8-30-2011

Structural characterization of metal binding in metallo-b-lactamases using x-ray absorption spectroscopy

Robert Breece

Robert M Breece

Candidate

Chemistry and Chemical Biology

Department

This dissertation is approved, and it is acceptable in quality and form for publication:

Approved by the Dissertation Committee:

, Chairperson

STRUCTURAL CHARACTERIZATION OF METAL BINDING IN METALLO-B-LACTAMASES USING X-RAY ABSORPTION SPECTROSCOPY

BY

ROBERT M BREECE

B.S., CHEMISTRY, BUTLER UNIVERSITY, 2000
M.S., CHEMISTRY, MIAMI UNIVERSITY, 2004

DISSERTATION

Submitted in Partial Fulfillment of the
Requirements for the Degree of

DOCTOR OF PHILOSOPHY
CHEMISTRY

The University of New Mexico
Albuquerque, New Mexico

AUGUST, 2011

STRUCTURAL CHARACTERIZATION OF METAL BINDING IN METALLO-B-LACTAMASES USING X-RAY ABSORPTION SPECTROSCOPY

BY

ROBERT M BREECE

ABSTRACT OF DISSERTATION

Submitted in Partial Fulfillment of the
Requirements for the Degree of

DOCTOR OF PHILOSOPHY
CHEMISTRY

The University of New Mexico
Albuquerque, New Mexico

AUGUST, 2011

STRUCTURAL CHARACTERIZATION OF METAL BINDING IN METALLO-β-LACTAMASES USING X-RAY ABSORPTION SPECTROSCOPY

By

Robert M Breece

B.S., CHEMISTRY, BUTLER UNIVERSITY, 2000
M.S., CHEMISTRY, MIAMI UNIVERSITY, 2004
Ph.D., CHEMISTRY, UNIVERSITY OF NEW MEXICO, 2011

ABSTRACT

In an effort to probe the structure and mechanism of metallo-β-lactamases, the metal-binding behaviors of several enzymes were studied using EXAFS (Extended X-ray Absorption Fine Structure). Three members of the metallo-β-lactamase subclass B1, BcII from *Bacillus cereus*, Bla2 from *Bacillus anthracis* and CcrA from *Bacillus fragilis*, were compared to examine metal-binding behavior within a subclass. Each system exhibits different metal-binding behavior including cooperative binding (BcII), sequential binding (CcrA), and differential binding between zinc(II) and cobalt(II) forms (Bla2). The metal-binding behavior of subclass B3 of L1 from *Stenotrophomonas maltophilia* was explored with RFQ (rapid-freeze quenched) EXAFS and site selective metal substitution. RFQ EXAFS show the metal coordination at 10 ms in the reaction in the native enzyme including a zinc-zinc distance (3.72Å) greater than is present in either the resting or product-bound states. Metal substitution incorporates cobalt(II) into the Zn_2(DHH) of the enzyme and showed the metal-binding at each metal site.

List of Figures

List of Tables

Chapter I

Metallo-β-Lactamase Family

Introduction

The metallo-β-lactamase family is a class of enzymes with a unique αβ/βα sandwich fold. Among the members of this family are the three subclasses of metallo-β-lactamases, glyoxalase 2, and the quorum sensing lactonases. This family of enzymes has a metal binding site at the interface between the two β-sheet domains which binds most divalent cations, but preferentially binds one or two equivalents of zinc in the case of metallo-β-lactamases and lactonases, one iron and one zinc in the case of glyoxalase 2, and two irons in the case of rubredoxin:oxygen oxidoreductase. The substrates of these enzymes vary dramatically, but each catalyzes the hydrolysis at a carbonyl.

Metallo-β-Lactamases

Through the widespread use, abuse, and misuse of β-lactam antibiotics selective pressures on the bacterial population has led to the appearance of resistant strains. [1-4] These resistant strains emerge within a few years of the drugs introduction and grow more prevalent as the drug's use becomes widespread. Despite the ongoing progress of antibiotic design, resistance to β-lactam antibiotic is a serious clinical problem,

particularly in immunosuppressed patients and in hospital acquired infections. The most common mechanism of resistance is the production of β-lactamases.These antibiotics mimic the natural substrate of transpeptidase, which is the pentapeptide chain attached to the peptidoglycan layer. The peptidoglycan layer is found within the cell wall of both gram positive and gram negative bacteria. It is composed of a sugar polymer backbone with peptide linking sugar chains together. Transpeptidase is the enzyme responsible for these cross-links. In the presence of β-lactam antibiotics, transpeptidase is inactivated by covalent modification of the site. The lack of cross-links in the peptidoglycan layer causes the cells to lyse due to internal osmotic pressure. [5]

Bacteria have produced four classes of β-lactamases to combat β-lactam antibiotics. Three of these classes, A,C, and D, use serines as the nucleophile that cleaves the β-lactam bond. The serine β-lactamases have a clinically viable inhibitor and display narrow substrate specificity. The last class, B, uses a zinc-bound hydroxide as the nucleophile. This class has wide substrate specificity with activity towards the three varieties of β-lactam antibiotics. The B class is further subdivides into three subclasses (B1, B2, and B3) based on amino acid sequence homology and substrate preference. [2, 6] Clinically viable inhibitors of serine β-lactamases, such as clavulanic acid, sulbactam, and tazobactam, are used in combination with β-lactam antibiotics to combat resistant bacterial strains. However, metallo-β-lactamases are unaffected by these inhibitors. To date, no clinically viable inhibitors have been produced against metallo-β-lactamases. [6] Without a viable inhibitor and the wide substrate specificity, metallo-β-lactamases are an important target in combating bacterial antibiotic resistance.

The first subclass, B1, is the largest family and contains the best studied metallo-β-lactamases. Members of this group include CcrA[7, 8] from *Bacillus fragilis* and BcII [9-11]from *Bacillus cereus*. The preferred substrate for this class is penicillins, though they display activity with all three types of β-lactam antibiotics. With a single equivalent of zinc (II) they show 70% activity. A second equivalent restores full activity. The two biding sites for the zinc are known as Zn_1 and Zn_2. The Zn_1 (3H) site is composed of three histidine residues, similar to the active site found in carbonic anhydrase and many zinc hydrolases. The Zn_2 (DCH) site is composed of one histidine, one cysteine, and one aspartate residues in addition to a terminal water. The two zinc sites are bridged by a hydroxide ion. This bridging hydroxide is believed to be the nucleophile that hydrolyzes the lactam bond.

The second subclass, B2, requires only a single equivalent of zinc to achieve full activity. Additional equivalents inhibit the enzyme's activity. Prominent members of this class are ImiS [12] from *Aeromonas veronii* and CphA [13] from *Aeromonas hydrophillia.* Subclass B2 utilizes carbapenems as its preferred substrate. The active equivalent of zinc occupies the Zn_2 site of the typical metallo-β-lactamase active site with one histidine, one cysteine, and one aspartate coordinating the metal ion. The second metal binding site is disrupted by a mutation in the Zn_1 site, where one of the metal binding histidines is replaced by a nonbinding asparagine. The second equivalent of zinc coordinates between a methionine located in a nearby loop and one histidine ligand. [14]

The third subclass, B3, contains the enzymes L1 [15, 16] from *Stenotrophomonas maltophilia* and Gob-18 [17] from *Elizabethkingia meningoseptica*. Subclass B3 prefers cephalosporins as its preferred substrate, though it retains activity towards most varieties

of β-lactam antibiotics. In most cases, one equivalent of zinc provides 70% activity and the second equivalent restores full activity. The active site is similar to subclass B1 with the cysteine of site Zn_2 (DHH) altered to a histidine. Previous studies suggest the active site is populated sequentially with the Zn_1 (3H) site becoming populated in advance of the Zn_2 (DHH) site. Gob-18 is classified as a B3 enzyme based on sequence homology and substrate specificity, however Gob-18 only requires one equivalent of metal for full activity. It contains a similar point mutation to the B2 subclass, where a Zn_1 (3H) site histidine is altered into a glutamine. Unlike the B2 subclass, this enzyme is not inhibited by additional equivalents of metal ions.

Metallo-β-Lactamase Superfamily

The αβ/βα fold appears in more than just the metallo-β-lactamase enzymes. This folding motif is more prevalent in prokaryotes than in eukaryotes. Members of this super family include: glyoxalase 2 (GLX2) [18], a detoxification enzyme that is found in bacterial, plant, and animal cells; zinc-dependent phosphodiesterase [19] (ZiPD) from *Eschericia coli,* a tRNase Z homolog; rubredoxin:oxygen oxidoreductase [20] (ROO) from *Desulfovibrio gigas,* a dioxygen reduction enzyme*;* acyl-homoserine-lactone lactonase [21-23] (AHLlac) from *Bacillus thuringensis*, which hydrolyzes extracellular lactones used for quorum sensing; methylparation hydrolase [24] (MPH) from *Pseudomonas* sp., which degrades the organophospate pesticide methyl parathion; phosphorylcholine esterase [25] (Pce) from *Streptococcus pneumoniae*, which hydrolyzes the phosphorylcholine residues from teichoic and lipoteichoic acids; and alkylsulfatase

[26] (SDSA1) from *Pseudomonas aeruginosa,* which degrades and metabolizes sodium dodecylsulfate. The metal binding site in these enzymes is similar to a B3 metallo-β-lactamase, but includes a carboxylate residue that bridges the two metals. These enzymes use two equivalents of metal for their activities, but the identity of those metals vary from enzyme to enzyme. AHL lactonase uses zinc exclusively. Glyoxalase 2 uses a combination of iron and zinc, as well as manganese in plants. The ROO site uses two irons and includes an carboxylate in the place of a histidine in the Zn_1 (3H) site. These enzymes are responsible for a wide variety of reactions, but many of them are produced in response to substances that are toxic to the host cells.

Metal Binding

The metal binding behavior of metallo-β-lactamases of the three subclasses have been studied, but the mode of metal binding is still disputed. It has been discussed that the only biologically relevant form is the monozinc form. All subclasses of metallo-β-lactamases are active with a single equivalent of metal. Studies have shown that the first equivalent of metal goes to the Zn_1 (3H) site of B1 [27, 28] and B3[29] enzymes and to the Zn_2 (DCH) side of the B2 [13, 14] subclass. With all three subclasses performing similar chemistry and retaining activity with a single equivalent of metal, this form is capable of accounting for *in vivo* activity. Other studies have suggested that the di-zinc form is the biologically relevant form, but that upon release of product that one metal is removed from the active site. [30]

The metal-binding behavior of metallo-β-lactamases could follow three schemes, which are dependent on the binding constants for the two sites. If the binding constants are more than an order of magnitude different, the binding process would follow a sequential process with metals binding to the tighter binding site before populating the second looser site. Greater disparities between the binding constants would result in one site dominating the initial site bound. As the binding constants of the site become equivalent, both sites would be populated simultaneously resulting in a random arrangement of metals. In the random arrangement the four population states of the enzymes (empty, Zn_1 bound, Zn_2 bound, and fully loaded) could be present at the same time. A third possibility is cooperative binding. In this scheme, the addition of the first equivalent of metal increases the binding affinity of the second site. The second site becomes preferentially populated instead of the first site of another protein molecule. This produces a population that is either fully loaded or apoenzyme, with low quantities of the mono-substituted form.

The metal binding behavior has been studied for a member of each of the three subclasses. Only x-ray absorption spectroscopy and x-ray diffraction can study the metal site of the native enzyme, so metal substitution was used to supplement native enzyme studies. The substitution of cobalt for the zinc is commonly used to produce enzymes with more favorable spectroscopic properties. The substitution exhibits similar activities to the native form and will generally adopt the same coordination number and geometry. Four techniques provide information specific to the metal binding to the active site. The first applies to the native, zinc-containing enzyme, but all three can apply to cobalt-substituted enzyme. The primary means of studying the metal-binding behavior of the

native enzyme is through x-ray absorption spectroscopy, which will provide information about coordination number, bond length, and the identity of the attached ligands. This technique allows for direct comparison between the zinc and cobalt-substituted forms. The other two techniques are only applicable to the cobalt-substituted form of the enzyme. UV-visible spectroscopy can suggest the coordination number and the presence or absence of a ligand-to-metal charge transfer band is indicative of cobalt-sulfur bonds. Paramagnetic ^{1}H NMR may also be used to look at the metal binding site. The protons of metal-bound residues have their chemical shifts altered by the presence of the unpaired electrons on the cobalt. The β protons on cysteine residues and the protons on the histidine rings have different chemical shifts and the histidine protons are solvent exchangeable. The fourth technique that can be useful in identifying the metal binding site in cobalt-substituted enzymes is EPR spectroscopy, which is sensitive to the geometry about a paramagnetic metal. Large changes in the active site will result in different spectral features; accordingly it is possible to tell if a single species or multiple species populate the active site. In this way it is possible to distinguish between the sequential and random/cooperative models of metal binding. With this technique, modeling the spectra will suggest coordination number for a given species. Included in the model is a measure of the rhombicity of the site. This value increases to a maximum of 1/3 the zero field splitting. At the maximum, the suggest coordination number is five and at the minimum the coordination number favored is six. The four techniques are complementary and the information that is discovered builds a structural model for the active site.

Subclass B1 is the most widely studied subclass with two representative members (BcII and CcrA) that have been studied spectroscopically. As previously mentioned, these two enzymes have a binuclear active site that requires 2 equivalents of zincs (II) for full activity. The first site contains three histidines and a hydroxide bridging the metals. The second site contains one histidine, one aspartic acid, one cysteine, a terminal water, and the bridging water. The two sites are very different from each other and provide three criteria for distinguishing the sites. The presence of the cysteine ligand is identifiable in all three of the listed techniques, through the Zn-S bond by x-ray absorption spectroscopy, LMCT band in the UV-visible spectroscopy, and the β-protons by NMR. The number of histidines can be monitored through EXAFS and paramagnetic ^{1}H NMR. More subtle is the coordination number which is four in the Zn_1 (3H) site and five in the Zn_2 (DCH) site, which the intensity of the l->d spectral bands and the intensity of EXAFS oscillations can suggest.

For CcrA, studies have been conducted on the zinc and cobalt forms of both the mono- or di-substituted enzymes. With a single equivalent of zinc added, the EXAFS analysis shows a coordination number of four nitrogens or oxygens with three of those identified as histidines. [31] EXAFS of dizinc CcrA is best fit by 4 nitrogen or oxygens ligands, half a sulfur ligand, half of a carboxylate carbon, two histidines, and a Zn-Zn distance of 3.42 Å. These fits correspond to a sequential binding model, where the first equivalent of zinc occupies the Zn_1 site and the second equivalent forming the bridged species seen in the crystal structure. The EXAFS of the mono- and di-cobalt-substituted enzymes are similar to each other, but distinct from the Zn enzymes. They both fit to five nitrogen/oxygen and two and a half histidines. There is no improvement of the fit upon

addition of a sulfur ligand. Likewise, the cobalt-cobalt distance is not apparent, which suggests that there is no bridging hydroxide/water between the metals. The higher coordination number, five compared to four and four and a half, likely reflects the adoption of additional solvent molecules. However, other spectroscopic techniques suggest that the first equivalent of cobalt occupies the Zn_1 site. [28] In the UV-visible spectra the LMCT band does not appear until there is more than one equivalent of cobalt. Additionally, the paramagnetic ^1H NMR shows no evidence of the β protons until the second site begins to be filled. The additional information suggests that the cobalt-substituted form of the enzyme similarly displays sequential binding, but the sites are not identical to the Zn enzymes. The EPR of the CcrA shows that the one equivalent and two equivalent species are distinct suggesting that the site builds sequentially. The dicobalt species is composed of two separate species one of which displays the same features as the monocobalt CcrA. The suggest coordination number is five or six which is consistent with the EXAFS observation of added solvent ligands. The addition of an extra solvent molecule and the lack of a bridge suggests that the two forms do the same reaction from different starting points.

Another member of the subclass B1 (BcII) shows a different trend from CcrA. Preliminary studies with UV-visible and NMR spectroscopy suggest that from small additions of cobalt to apo BcII results in some cobalt-sulfur bond formation. [32] In the UV-visible spectra, the LMCT band appears as the initial equivalents of metal are added, which continues to grow up to two equivalents. NMR spectra remain unchanged from the lowest quantities of cobalt through the second equivalent. The EPR of cobalt-substituted BcII shows that at substoichiometric equivalents of metal, multiple species of cobalt can

be found. There is also evidence that this species will form a bridged species because of a deviation of spin density attributed to spin-coupled di-cobalt sites. Later in this work, EXAFS analysis will explore the metal binding behavior of BcII with cobalt as well as with the native zinc.

The representative member of subclass B2 that has been extensively probed is ImiS. There is currently no crystal for this enzyme, but another member of this subclass CphA has been crystallized. [13] This crystal structure shows that the single equivalent of zinc occupies the Zn_2 (DCH) site. Spectroscopic studies have been consistent with this picture. Native ImiS was characterized by EXAFS and has three nitrogen/oxygens, one sulfur, with one histidine. [14] All three techniques have been used to look at cobalt-substituted ImiS. EXAFS analysis is best fit by 5 nitrogen/oxygen with one histidine. [27] The addition of a sulfur shell does not significantly improve the fit residual, but the presence of the sulfur can be seen by the presence of β protons in the NMR and by the presence of the cobalt-sulfur LMCT band. [33] The inhibitory second equivalent of metal has also been studied by EXAFS. The second equivalent of zinc binds to a site similar to the first. The average of the two sites is three nitrogen/oxygen and one sulfur with one histidine. The enzyme contains no additional cysteine residues in the active site, but a methionine is present in a mobile loop near the site. With metal bound, the loop's mobility is hindered and the enzyme is inhibited. The mutation of the methionine to a nonbinding ligand removes inhibition of additional equivalents of zinc.

The member of subclass B3 that has been best characterized is L1. This enzyme has been studied with the four techniques detailed previously. In most ways, it is similar to the subclass B1 enzyme CcrA, though it lacks the diagnostic sulfur ligand. The first

equivalent of metal occupies the Zn_1 (3H) site with the second equivalent completing the binuclear site. [29] The cobalt form of the enzyme displays a tendency to higher coordination number than the corresponding zinc form, which suggests that each site gains a solvent molecule. [27] This would place the coordination at five and six for the Zn_1 and Zn_2 sites respectively. The location of the first metal site was inconclusive via the EXAFS fits, but the number of histidine peaks in the NMR spectrum established that binding is sequential with the metal occupying the Zn_1 (3H) site. The metallo-β-lactamase Gob-18, is placed within subclass B3 based on its substrate specificity and sequence homology, but its metal binding behavior is dramatically different from L1. As mentioned earlier, Gob-18 is a mononuclear enzyme that requires only one zinc for full activity. [17] An active site residue has been modified from a histidine in the Zn_1 site (3H) into a glutamine, which disrupts that binding site. This enzyme binds the zinc at the Zn_2 site (DHH), in a similar manner to the B2 enzymes.

Mechanism

Metallo-β-lactamases are useful to the bacteria because they deactivate β-lactam antibiotics. The reaction they catalyze is the hydrolysis of the lactam bond, breaking open the four-membered ring. The ring opening reaction eliminates the inhibition of transpeptidase and allows for the creation of the bacterial cell wall. The four-membered ring is stable at physiologically relevant pH, but the presence of metal activates a water molecule for the nucleophilic attack.

The evidence on the mechanism of the metallo-β-lactamases is only modest. Structures of resting and product-bound complexes have been studied through crystallographic, [13, 16, 34-36] spectroscopic, [8, 12, 14, 29, 32, 33, 37-50] and computational [51-62] techniques. This provides two steps in the overall mechanism. The intervening steps have been studied in two cases. The hydrolysis of nitrocefin produces a spectroscopically observable substrate, which has been studied using stopped-flow kinetics. [40] The second example is a moxalactam intermediate-bound studied with crystallography. [36] Additionally, computational studies have been conducted in specific lactamase-substrate pairings. These studies provide additional detail into the mechanism, but they may only be important to the individual reactions depicted.

The first stage of the mechanism is the substrate binding to the active site. In di-metal active sites, computational and product-bound studies suggest that the β-lactam carbonyl is brought within close proximity to the Zn_1 (DCH) site while the carboxylate on the second ring binds to the Zn_2 site. The additional ligand bound to Zn_2 puts the zinc in the less favored five or six coordinate state. The release of the bridging water would provide for a strong nucleophile in close proximity to the carbonyl of the lactam ring. The attack of the nucleophile on the electropositive carbon is the next step in the proposed mechanism. This would cause the amide bond to break homolytically, leaving a lone pair on the lactam nitrogen. This brings the formal charge of the nitrogen to negative one. The charged nitrogen may be stabilized in multiple ways. It can form a bond to the nearby divalent zinc, it may simply be stabilized by the proximity to the positively charged zinc, or it can extract a proton from the active site water or nearby residues. In any of these three cases, the reaction product requires the extraction of a proton within the reaction

mechanism. After the ring opening reaction, the substrate is attached to the active site by two or three bonds and these connections must be be replaced by solvent and the original active site must be regenerated.

A spectroscopically observable intermediate of the reaction can be probed using the specialized β-lactam antibiotic nitrocefin. This cephalosporin contains a dinitrostyrene sidechain. This sidechain extends the conjugation of the six-membered ring on the cephalosporin core and can form several resonance structures after ring opening. When this cephalosporin is reacted with a metallo-β-lactamase, the β-lactam ring is cleaved and a stable intermediate is formed. [40] This intermediate can be studied using rapid-scanning and stopped-flow UV-visible spectroscopy. The substrate has an absorbance maximum at 390 nm and the product displays an absorbance at 485 nm. Unlike other antibiotics however, the hydrolysis of nitrocefin leads to a third absorption at 665 nm. The third absorption corresponds to an intermediate species, which is formed rapidly (5 ms) and is more slowly converted to the product (25 ms).

An intermediate of the pairing of L1 with the β-lactam moxalactam was studied by crystallography by Spencer, *et. al*. [36] This structure shows a ring opened moxalactam bound to the dizinc active site of L1. In this case, the carboxylic acid that originated from the amide carbonyl is bound to Zn_2 (3H) and both the amide-originated nitrogen and the secondary ring carboxylic acid is bound to Zn_1 (DCH). The distances of these interactions measured from the crystal structure are 2.4 Å, which are longer than the bonds to the enzyme residues and the bridging water (2.0Å – 2.1Å). Computational studies of this same reaction decrease these bonding distances to approximately those of the enzyme residues. [60] The crystal structure is also missing a portion of the

moxalactam, R' has been altered from 1-methyl tetrazole, connected to the antibiotic through a thioether linkage, to a simple methyl group.

Each of the two mono-substituted metallo-β-lactamase have shown activity as well, and are suggested to follow similar mechanisms. In the case of B2 metallo-β-lactamases, the Zn_2 (3H) site is missing. This site's role in the L1 mechanism is providing the nucleophilic hydroxide, which attacks the lactam carbonyl. This function could be replaced by an activated solvent molecule. In the case of metallo-β-lactamases missing the Zn_2 (DCH) site, the function of this site appears to be the binding of the carboxylic acid of the second ring, which fixes the substrate into the proper orientation. Secondary interactions in the active site may serve to orient the substrate. These cases lower the overall activity of the site. In summary, the di-zinc mechanisms are viewed with some consensus, while the mono-zinc mechanism remain controversial.

Site Plasticity

A trend that is appearing within the metallo-β-lactamase family is the versatility of the site. The system can display reactivity in all three of the metal containing forms. CcrA and L1 display 70% activity with the Zn_1 site solely populated. Gob-18 and ImiS display full activity with the Zn_2 site populated. BcII, L1, and CcrA display their full activities with both sites filled with zinc. Attempts have also been made using site directed mutagenesis to convert one subclass into another, but have usually resulted in the desired metal binding behavior with a loss of activity. In the case of the conversion of BcII into variants that bind only one metal, the second site was removed by mutation of

binding ligands of the second site. [63] These two enzymes were named 3H-BcII and DCH-BcII. In both cases, the rate constants of the reaction were several orders of magnitude lower than wild type. Another case, the attempt to convert Gob-18 into a 'standard' member of subclass B3, was even less successful. An active site glutamine was mutated into a histidine, which should have restored the Zn_1 (3H) site. However, the site was unable to bind the second equivalent of metal suggesting that the changes to this enzyme alters secondary interactions that affects the orientation of the metal binding residues. The activity of the Q116H mutant of Gob-18 was present for all classes of β-lactam antibiotics. The activity towards penicillin antibiotics was 80% of the native enzyme, but the activity towards the other two classes was only 25%.

A more successful case was the conversion of BcII into the other two types of dizinc sites. [64] A BcII-HD mutant was created by the conversion of the active site arginine into a histidine and the cysteine ligand into an aspartate. These two mutations mimic the active site of glyoxalase 2. The other mutant was BcII-HS, which mutated the arginine into a histidine and the cysteine ligand into a serine, which turns the B1 active site into a B3 mimic. The BcII-HD bound two equivalents of zinc, but the activity towards all β-lactam antibiotics was reduced by two or more orders of magnitude. The BcII-HS mutant bound two equivalents of zinc and displayed a preference towards cephalosporins, but was still lower in activity compared to native BcII.

Metallo-β-lactamses are able to react with their chosen substrate under a wider variety of conditions. It functions as a zinc hydrolase from a wide variety of starting points. The site is functional can be active with metal populating either the Zn_1 or the Zn_2 sites and many of the individual members are active over a broad spectrum of β-

lactam antibiotics. Also, the mutation of point residues in the active site can interconvert subclasses to some extent.

Summary

The zinc-containing metallo-β-lactamase enzymes are an important family of enzymes to understand. Their presence among bacteria is continuing to move into more and more virulent strains and unlike the serine lactamases, they remain without a clinically viable inhibitor. With the wide ranging effectiveness of the metallo-β-lactamases, the need to understand their active site structure and mechanism in greater depth becomes more important. This work will explore in greater depth the metal binding behavior and reactivity of metallo-β-lactamase enzymes.

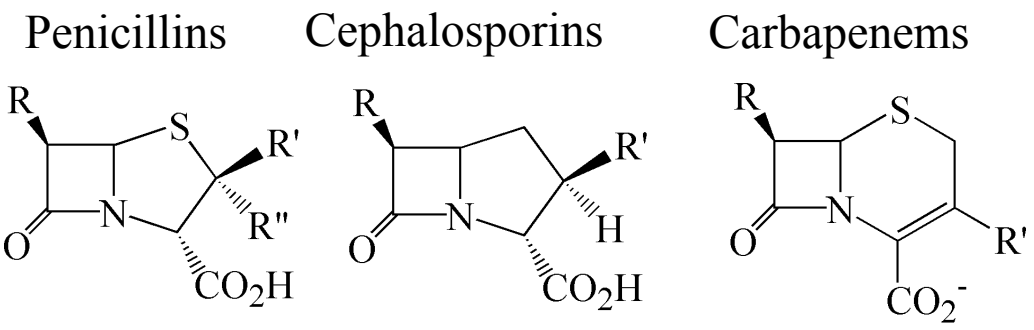

Figure 1-1: Three Classes of β-lactam Antibiotics

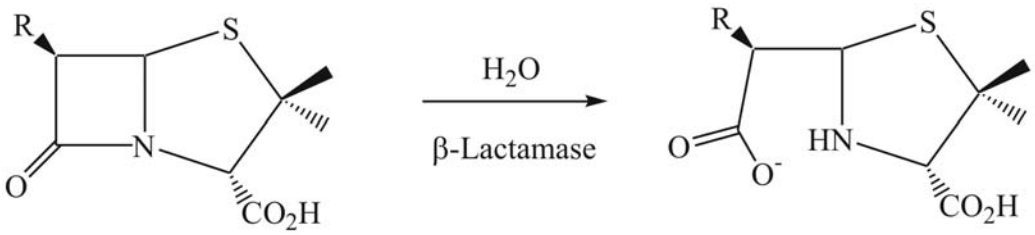

Figure 1-2: Reaction of β-lactamases

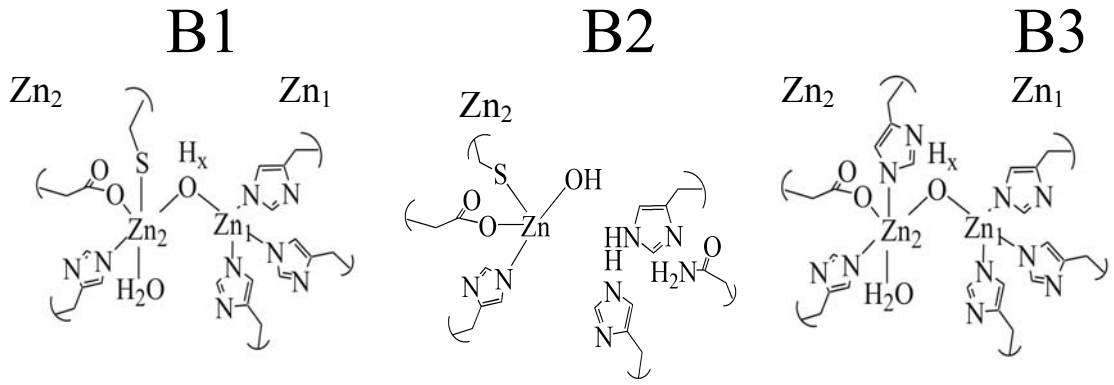

Figure 1-3: Three Subclasses of Metallo-β-lactamases

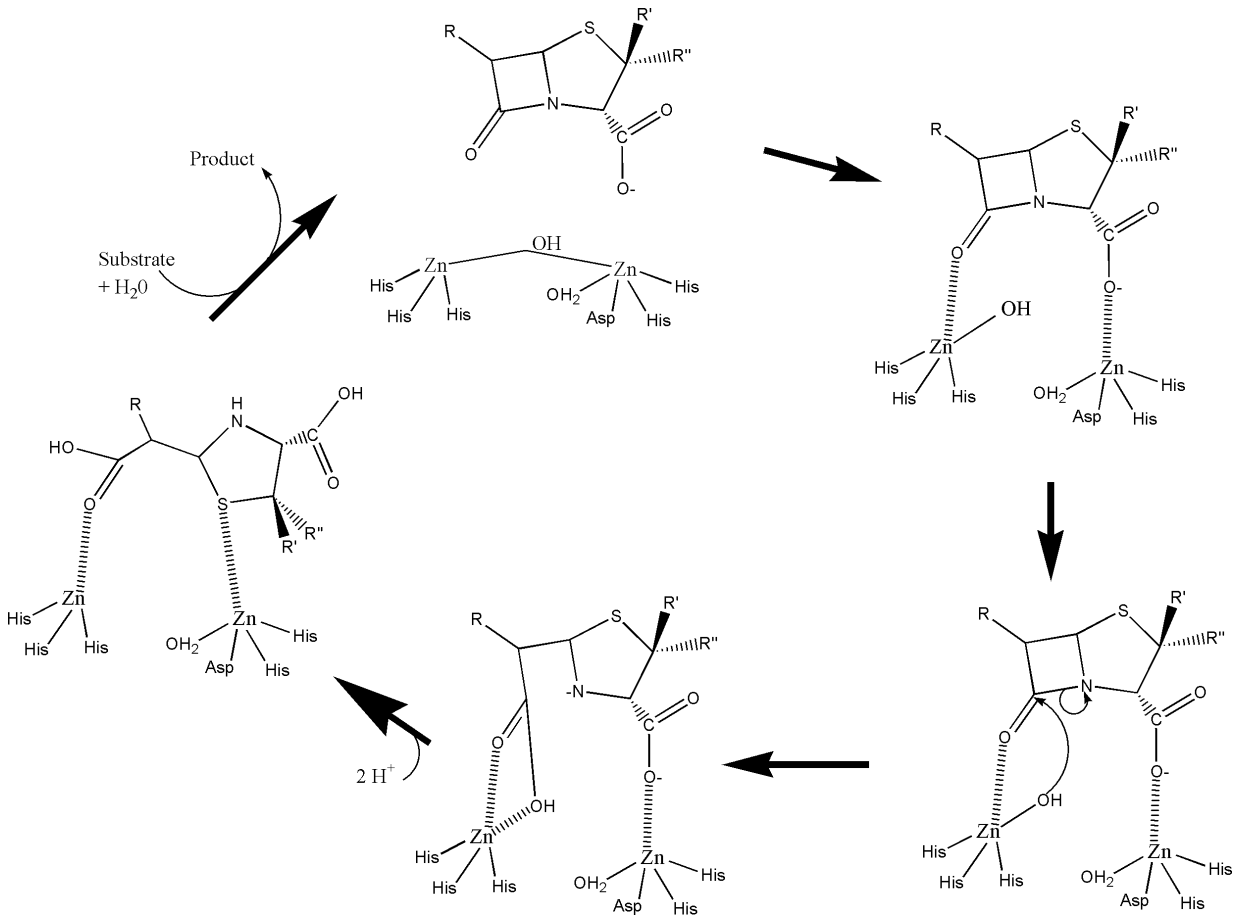

Figure 1-4: Proposed Reaction Mechanism for L1

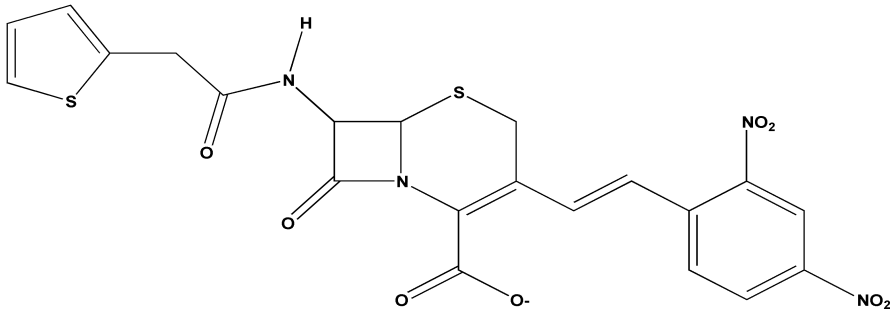

Figure 1-5: Structure of Nitrocefin

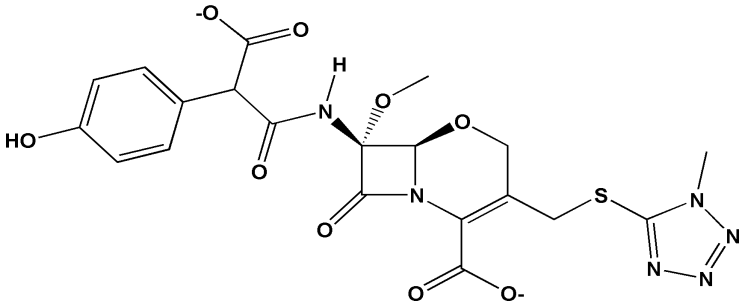

Figure 1-6: Structure of Moxalactam (Latamoxef)

References

1. Levy, S.B., *The Antibiotic Paradox: How the Misuse of Antibiotics Destroys Their Curative Powers*. Second ed. 2002: Perseus Publishing. 353.
2. Bush, K., *Metallo-β-Lactamases: A Class Apart.* Clinical Infectious Diseases, 1998. **27**(Suppl 1): p. S48-S53.
3. Levy, S.B., *The Challenge of Antibiotic Resistance.* Scientific American, 1998. **3**: p. 47-53.
4. Neu, H.C., *The Crisis in Antiobiotic Resistance.* Science, 1992. **257**: p. 1064-1073.
5. Prescott, L.M., J.P. Harley, and D.A. Klein, *Microbiology*. Sixth ed. 2005, New York: McGraw-Hill.
6. Crowder, M.W., J. Spencer, and A.J. Vila, *Metallo-b-lactamases: Novel Weaponry for Antibiotic Resistance in Bacteria.* Accounts of Chemical Research, 2006. **39**: p. 721-728.
7. Crowder, M.W., et al., *Characterization of the Metal-Binding Sites of the β-Lactamase from Bacteroides fragilis.* Biochemistry, 1996. **35**(37): p. 12126-12132.
8. Wang, Z., W. Fast, and S.J. Benkovic, *Direct Observation of an Enzyme-Bound Intermediate in the Catalytic Cycle of the Metallo-β-Lactmase from Bacteroides fragilis.* American Chemical Society, Journal of, 1998. **120**(41): p. 10788-10789.
9. Davies, R.B. and E.P. Abraham, *Metal Cofactor Requirements of β-Lactamase II.* Biochemical Journal, 1974. **143**: p. 129-135.

10. Davies, R.B., E.P. Abraham, and J. Melling, *Separation, Purification and Properties of β-Lactamse I and β-Lactamse II from Bacillus cereus 569/H/9.* Biochemical Journal, 1974. **143**: p. 115-127.

11. Ambler, R.P., et al., *The Amino Acid Sequence of the Zinc-Requiring β-Lactamase II from the Bacterium Bacillus cereus 569.* FEBS Letters, 1985. **189**(2): p. 207-211.

12. Walsh, T.R., et al., *Enzyme Kinetics and Biochemical Analysis of ImiS, the Metallo-β-Lactamase from Aeromonas sobria 163a.* Antimicrobial Chemotherapy, Journal of, 1996. **37**: p. 423-431.

13. Garau, G., et al., *A Metallo-β-Lactamase Enzyme in Action: Crystal Structures of the Monozinc Carbapenemase CphA and its Complex with Biapenem.* Molecular Biology, Journal of, 2005. **345**(4): p. 785-795.

14. Costello, A.L., et al., *An EXAFS study of the Zn(II) Binding Sites in Aeromonas veronii bv. sobria.* 2006(Manuscript in preparation).

15. Crowder, M.W., et al., *Overexpression, Purification, and Characterization of the Cloned Metallo-β-Lactamase L1 from Stenotrophomonas maltophilia.* Antimicrobial Agents and Chemotherapy, 1998. **42**(4): p. 921-926.

16. Ullah, J.H., et al., *The Crystal Structure of the L1 Metallo-β-Lactamase from Stenotrophomonas maltophilia at 1.7 Å Resolution.* Molecular Biology, Journal of, 1998. **284**(1): p. 125-136.

17. Barrio, J.M., et al., *The metallo-β-lactamase GOB is a mono-Zn (II) enzyme with a novel active site.* Journal of Biological Chemistry, 2007. **282**(25): p. 18286-18293.

18. Crowder, M.W., et al., *Glyoxalase II from A. thaliana requires Zn(II) for Catalytic Activity.* FEBS Letters, 1997. **418**: p. 351-354.

19. Kostelecky, B., et al., *The Crystal Structure of Zinc Phosphodiesterase from Escherichia coli Provides Insight into Function and Coopertivity of tRNase Z-Family Proteins.* Journal of Bacteriology, 2006. **188**(4): p. 1607-1614.

20. Frazao, C., et al., *Structure of a Dioxygen Reduction Enzyme from Desulfovibrio gigas.* Nature Structural Biology, 2000. **7**(11): p. 1041-1045.

21. Thomas, P.W., et al., *The Quorum-quenching Lactonase from Bacillus thuringiensis is a Metalloprotein.* Biochemistry, 2005. **44**(20): p. 7559-7569.

22. Momb, J., et al., *The Quorum-Quenching Metallo-γ-lactonase from Bacillus thuringiensis Exhibits a Leaving Group Thio Effect.* Biochemistry, 2006. **45**: p. 13385-13393.

23. Momb, J., et al., *Mechanisms of the Quorum-Quenching Lactonase (AiiA) from Bacillus thuringiensis. 2. Substrate Modeling and Active Site Mutations.* Biochemistry, 2008. **47**: p. 7715-7725.

24. Dong, Y.J., et al., *Crystal Structure of Methyl Parathion Hydrolase from Pseudomonas sp. WBC-3.* Journal of Molecular Biology, 2005. **353**: p. 655-663.

25. Lagartera, L., et al., *Pneumococcal phosohorylcholine esterase, Pce, Contains a Metal Binclear Center That is Essential for Substrate Binding and Catalysis.* Protein Science, 2005. **14**: p. 3013-3024.

26. Hagelueken, G., et al., *The Crystal Structure of SdsA1, an alkylsulfatase from Pseudomonas aeruginosa, Defines a Third Class of Sulfatases.* Proceedings of the

National Academy of Science of the United States of America, 2006. **103**(20): p. 7631-7636.

27. Costello, A.L., unpublished results.

28. Periyannan, G., et al., *Sequential Binding of Co(II) to Metallo-β-Lactamase CcrA.* Biochemistry, 2006. **45**(4): p. 1313-1320.

29. Costello, A.L., et al., *Site Selective Binding of Zn(II) to Metallo-b-Lactamase L1 from Stenotrophomonas maltophilia.* Biological Inorganic Chemistry, Journal of, 2006. **11**(3): p. 351-358.

30. Badarau, A. and M.I. Page, *Loss of Enzyme Activity During Turnover of the Bacillus cereus β-lactamase Catalyzed Hydrolysis of β-lactams due to loss of zinc ion.* Journal of Biological Inorganic Chemistry, 2008. **13**: p. 919-928.

31. Hawk, M.J., et al., *Differential Binding of Co(II) and Zn(II) to Metallo-β-lactamase Bla2 from Bacillus anthracis.* Journal of the American Chemical Society, 2009. **131**(30): p. 10753-10762.

32. Llarrull, L.I., et al., *Evidence for a Dinuclear Active Site in the Metallo-β-lactamase BcII with SubStoichiometric Co(II).* Journal of Biological Chemistry, 2007. **282**(42): p. 30586-30595.

33. Crawford, P.A., et al., *Spectroscopic Studies on Cobalt(II)-Substituted Metallo-β-lactamase ImiS from Aeromonas veronii bv. sobria.* Biochemistry, 2005. **44**(13): p. 5168-5176.

34. Fabiane, S.M., et al., *Crystal Structure of the Zinc-Dependent β-Lactamase from Bacillus cereus at 1.9 Angsrom Resolution: Binuclear Active Site with Features of a Mononuclear Enzyme.* Biochemistry, 1998. **37**(36): p. 12404-12411.

35. Concha, N.O., et al., *Crystal Structure of the IMP-1 Metallo-β-Lactamase from Pseudomonas aeruginosa and Its Complex with a Mercaptocarboxylate Inhibitor: Binding Determinants of a Potent, Broad-Spectrum Inhibitor.* Biochemistry, 2000. **39**(15): p. 4288-4298.

36. Spencer, J., et al., *Antibiotic Recognition by Binuclear Metallo-β-Lactamases Revealed by X-ray Crystallography.* American Chemical Society, Journal of, 2005. **127**(41): p. 14439-14444.

37. Crawford, P.A., et al., *Over-expression, purification, and characterization of metallo-β-lactamase ImiS from Aeromonas veronii bv. sobria.* Protein Expression and Purification, 2004. **36**(2): p. 272-279.

38. Llarrull, L.I., M.F. Tioni, and A.J. Vila, *Metal Content and Localization During Turnover in B. Cereus Metallo-β-lactamase.* Journal of the American Chemical Society, 2008. **130**: p. 15842-15851.

39. Scrofani, S.D.B., et al., *NMR Characterization of the Metallo-β-Lactamase from Bacteroides fragilis and Its Interaciton with a Tight-Binding Inhibitor: Role of an Active-Site Loop.* Biochemistry, 1999. **38**(44): p. 14507-14514.

40. Wang, Z., W. Fast, and S.J. Benkovic, *On the Mechanism of the Metallo-β-Lactamase from Bacteroides fragilis.* Biochemistry, 1999. **38**(31): p. 10013-10023.

41. Wang, Z., et al., *Metallo-b-Lactamases: Structure and Mechanism.* Current Opion. Chem. Biol., 1999. **3**: p. 614-622.

42. Fast, W., Z. Wang, and S.J. Benkovic, *Familial Mutations and Zinc Stoichiometry Determine the Rate-Limiting Step of Nitrocefin Hydrolysis by Metallo-β-Lactamase from Bacteroides fragilis.* Biochemistry, 2001. **40**(6): p. 1640-1650.

43. Yanchak, M.P., R.A. Taylor, and M.W. Crowder, *Mutational Analysis of Metallo-β-Lactamase CcrA from Bacteroides fragilis.* Biochemistry, 2000. **39**(37): p. 11330-1139.

44. Simm, A.M., et al., *Characterization of Monomeric L1 Metallo-β-Lactamase and the Role of the N-Terminal Extension in Negative Cooperativity and Antibiotic Hydrolysis.* Biological Chemistry, Journal of, 2002. **277**(27): p. 24744-24751.

45. McManus-Munoz, S. and M.W. Crowder, *Kinetic Mechanism of Metallo-β-Lactamse L1 from Stenotrophomonas maltophilia.* Biochemistry, 1999. **38**(5): p. 1547-1553.

46. Periyannan, G., et al., *In vivo Folding of Recombinant Metallo-β–Lactamase L1 Requires the Presence of Zn(II).* Protein Science, 2004. **13**(8): p. 2236-2243.

47. Yang, Y., et al., *Kinetic Properties and Metal Content of the Metallo-β-Lactamse CcrA Harboring Selective Amino Acid Substitutions.* Biological Chemistry, Journal of, 1999. **274**(22): p. 15706-15711.

48. Valladares, M.H., et al., *Zn(II) Dependence of the Aeromonas hydrophila AE036 Metallo-β-Lactamase Activity and Stability.* Biochemistry, 1997. **36**(38): p. 11534-11541.

49. Valladares, M.H., et al., *Kinetic and Spectroscopic Characterization of Native and Metal-Substituted β-Lactamase from Aeromonas Hydrophila AE036.* FEBS Letters, 2000. **467**: p. 221-225.

50. Felici, A. and G. Amicosante, *Kinetic Analysis of Extension of Substrate Specificity with Xanthomonas maltophilia, Aeromonas hydrophila, and Bacillus cereus Metallo-β-Lactamses.* Antimicrobial Agents and Chemotherapy, 1995. **39**(1): p. 192-199.

51. Dal Peraro, M., et al., *Water-Assisted Reaction Mechanism of Monozinc β-Lactamases.* American Chemical Society, Journal of, 2004. **126**(39): p. 12661-12668.

52. Diaz, N., D. Suarez, and K.M. Merz, *Molecular Dynamics Simulations of the Mononuclear Zinc-β-Lactamase from Bacillus cereus Complexes with Benzylpenicillin and a Quantum Chemical Study of the Reaction Mechanism.* American Chemical Society, Journal of, 2001. **123**: p. 9867-9879.

53. Diaz, N., D. Suarez, and K.M. Merz, *Zinc Metallo-β-Lactamase from Bacteroides fragilis: A Quantum Chemical Study on Model Systems of the Active Site.* American Chemical Society, Journal of, 2000. **122**: p. 4197-4208.

54. Prosperi-Meys, C., et al., *Substrate Binding and Catalytic Mechanism of Class B β-Lactamases: A Molecular Modeling Study.* Cell Mol. Life Sci., 2001. **58**: p. 2136-2143.

55. Salsbury, F.R., M.F. Crowley, and C.L. Brooks, *Modeling of the Metallo-β-Lactamase from B. fragilis: Structural and Dynamic Effects of Inhibitor Binding.* Proteins: Struct., Funct., Genet., 2001. **44**: p. 448-459.

56. Suarez, D., E.N. Brothers, and J. Merz, K.M., *Insights into the Structure and Dynamics of the Dinulcear Zinc β-Lactamase Site from Bacteroides fragilis.* Biochemistry, 2002. **41**(21): p. 6615-6630.

57. Suarez, D., N. Diaz, and K.M. Merz, *Molecular Dynamics Simulations of the Dinuclear Zinc-β-Lactamase from Bacteroides fragilis Complexed with Imipenem.* Computational Chemistry, Journal of, 2002. **23**: p. 1587-1600.

58. Suarez, D. and K.M. Merz, *Molecular Dynamics Simulations of the Mononuclear Zinc-β-Lactamase from Bacillus cereus.* American Chemical Society, Journal of, 2001. **123**: p. 3759-3770.

59. Xu, D. and H. Guo, *Antibiotic Binding to Dizinc β-Lactamase L1 from Stenotrophomonas maltophilia SCC-DFTB/CHARMM and DFT Studies.* Journal of Physical Chemistry A, 2007. **111**: p. 5630-5636.

60. Xu, D., H. Guo, and Q. Cui, *Antibiotic Deactivation by a Dizinc b-Lactamase: Mechanistic Insights from QM/MM and DFT Studies.* American Chemical Society, Journal of, 2007. **129**: p. 10814-10822.

61. Xu, D., D. Xie, and H. Guo, *Catalytic Mechanism of Class B2 Metallo-β-lactamase.* Journal of Biological Chemistry, 2006. **281**(13): p. 8740-8746.

62. Xu, D., et al., *Antibitoic Binding to Monozinc CphA b-Lactamase from Aeromonas hydrophila: Quantum Mechanical/Molecular Mechanical and Density Functional Theory Studies.* Medicinal Chemistry, Journal of, 2005. **48**(21): p. 6679-6689.

63. Abriata, L.A., et al., *Engineered Mononuclear Variants in Bacillus cereus Metallo-β-lactamase BcII Are Inactive.* Biochemistry, 2008. **47**: p. 8590-8599.

64. Gonzalex, J.M., et al., *The Zn2 Position iin Metallo-β-lactamases is Critical for Activity: A Study on the Chimeric Metal Sites on a Concerved Protein Scaffold.* Molecular Biology, Journal of, 2007. **373**: p. 1141-1156.

Chapter II

X-Ray Absorption Spectroscopy

Introduction

X-ray absorption was first observed since the 1920's [1, 2] with the discovery of the photoelectic effect, but it wasn't until the 1970's with the development of synchrotron sources and the development of EXAFS theory [3-8] that the full potential of x-ray absorption spectroscopy (XAS) was demonstrated. The high intensity radiation with a wide spectral distribution allowed for the study of dilute samples. Of particular interest are non-crystalline metal containing biological samples, which are only available at low concentrations.

X-ray absorption spectroscopy measures the effect of core electrons being emitted after the absorption of incoming light of the appropriate wavelength. X-ray absorption has a threshold energy below which there is only modest loss of light intensity and above which light is absorbed. This threshold is equivalent to the ionization potential. The spectrum is divided into three distinct regions: the pre-edge, XANES, and EXAFS regions. In the pre-edge region, the incoming radiation is less than the necessary energy to disturb the core electrons and results in only background absorption and scattering of the light. The XANES (X-ray Absorption Near Edge Structure) region consists of transitions of core electrons to unoccupied bound states and low-lying continuum states. Most notable is a rise in the absorption coefficient, which is termed the absorption edge.

The energy of the edge is specific to each element and to the atomic shell from which the electron is ejected. The edge energy is modulated by the absorbing atom's environment and the atom's oxidation state. The region of lower energy near the edge corresponds to core electron excitation to valence levels, and its intensity provides details about the local symmetry of the absorbing element. The EXAFS (Extended X-ray Absorption Fine Structure) region extends above 50 to 1000 electron volts from the edge. At these energies, the core electron is ejected into the continuum where it is scattered off of nearby atoms, which creates an oscillatory modulation of the absorption coefficient. [9, 10] The following sections detail the theory of EXAFS and the general methods of data analysis.

EXAFS

The basic concepts behind the EXAFS phenomenon have been described previously. [9-11] In the EXAFS region, the incoming radiation exceeds the energy required to excite core electrons into the continuum as a photoelectron. Energy exceeding the ionization potential is converted to photoelectron kinetic energy. The photoelectron can be treated as a spherical wave with an equal probability of propagating in any direction, with kinetic energy ($E-E_0$) and a wavelength defined by the de Broglie relation ($\lambda=h/p$). As the photoelectron wave propagates through space, it interacts with surrounding matter and interferes with the outgoing wave. (Figure 2-2) This backscattering phenomenaon creates an interference pattern with maxima and minima that correspond to regions of constructive and destructive interference.

The resulting sinusoidal oscillations are termed EXAFS (Extended X-ray Absorption Fine Structure). This region of the spectrum provides information on the

local environment surrounding the absorbing atom. The EXAFS is a sum of sine waves, each corresponding to a nearby atom scattering the photoelectron wave. Each of the three defining characteristics of the sine waves correspond to a property of the absorber-scatterer pair. The frequency of the sine waves is a measure of the absorber-scatterer (as) distance. The amplitude of the sine waves correspond to the number and identity of the scattering atoms. Atoms at a similar distance contribute additively to the obserced sine wave amplitude. Similarly, heavier scatterers lead to larger amplitude. The phase of the sine wave is influenced by the photoelectron passing through the electric potential of the absorbing and scattering atoms. Each atom type has a different electron density and the phase shift is an indication of the absorber-scatterer pair.

The empirical expression for the EXAFS modulation is shown in Equation 2-1, where the EXAFS quantity, χ, is defined.

$$\chi(k) \equiv \frac{\mu - \mu_0}{\mu_0} \qquad \text{Eq 2.1}$$

In principle, Equation 2-1 isolates and normalizes the total absorption coefficient, μ, from the absorption coefficient of a monoatomic (free atom) absorber, μ_0. There are difficulties with direct measurement of μ_0, which require additional steps to isolate the EXAFS. The first step is background removal below the edge, which requires the subtraction of a polynomial or half-Gaussian to eliminate the background scattering and absorption from lighter elements. The second step is to eliminate contribution of μ_0 above the edge, which is approximated by fitting a high order piecewise polynomial (spline) to the EXAFS region. The third and final step is normalization to a calculated function that

approximates m_0. The normalization involves calculation of μ_0 and corrects for variations in pathlength or concentration among samples.

For ease of comparison of spectra from different absorbing atoms and to easily extract distance information it is convenient to convert the EXAFS data from energy (eV) to the photoelectron momentum vector ($Å^{-1}$)

$$k = \frac{2\pi}{\lambda} = \frac{p}{h} = \frac{2\pi m_e v}{h} = [\frac{8\pi^2 m_e}{h^2}(E - E_0)]^{1/2} = [0.2625(E - E_0)]^{1/2} \qquad \text{Eq. 2-2}$$

In Equation 2-2, λ, p, and m_e are the wavelength, momentum, and the mass of the photoelectron, respectively. The ionization potential, E_0, can be experimentally measured via photoelectron spectroscopy, but in practice it is treated as a variable by converting the data to k-space using a fixed E_0, then refining the number during the fitting process. The refined E_0 is reported as a shift in the ionization potential (ΔE_0). The energies were converted to k-space using the following values: E_0= 9680 eV (Zn) and E_0= 7725 eV (Co). Determination of the energy shifts is described later in this section.

The isolated EXAFS data is then fit to the theoretical expression for χ (Eq. 2-3) using a nonlinear least squares algorithm.

$$\chi(k) = \sum_s \frac{N_s A_{as}(k) S_c}{kR_{as}^2} \exp(-2R_{as}/\lambda) \exp(-2k^2 \sigma_{as}^2) \sin[2kR_{as} + \phi_{as}(k)] \qquad \text{Eq. 2-3}$$

Equation 2-3 is based on single scattering theory. Multiple scattering effects will be discussed later in this section. In equation 2-3, N_s is the number of scatterers (s) in a given shell of atoms, $A_{as}(k)$ is the backscattering amplitude of the absorber-scatterer (as) pair, σ_{as}^2 is the mean square deviation of the absorber-scatterer bond length (R_{as}), $\varphi_{as}(k)$ is the phase shift, and λ is the photoelectron mean free path, S_c is the scale factor, which is constant for any absorber-scatterer pair. The sum is taken over all shells of scatterers

that contribute to the EXAFS. EXAFS oscillation intensity is directly proportional to the number of scatterers and the back scattering amplitude. The intensity is diminished by a factor of inverse k, so data are usually presented as a $k^3\chi$ (k). The intensity is also diminished by the distance between the absorber-scatterer pair, which limits the amount of structural information to distances approximately 4.0-4.5 Å or less. The scale factor corrects for errors in the theoretically derived amplitude function and is experimentally determined by fitting data of known structure.

The next two terms in the EXAFS equation are exponential damping terms. The first term accounts for the inelastic losses from the photoelectron excited state lifetime, which has contributions from the hole in the core electronic structure resulting from the excitation and the photoelectron itself. The second term, known as the Debye-Waller factor, is associated with deviations of the bond length of the absorber-scatterer pair. The Debye-Waller factor is composed of two elements: static and dynamic disorder of the bond. The dynamic component is due to vibrational motions. This motion is temperature dependent and can be minimized by running the experiments at low temperature. The static disorder is due to structural variations within the sample.

The remaining term in the EXAFS equation provides the sinusoidal oscillation. This term contains two components: One provides the frequency, and one the phase shift. The frequency is directly correlated to the absorber-scatterer bond distance with low frequency corresponding to short bond distances and high frequencies corresponding to longer ones. With a Fourier transformation of the EXAFS, the frequencies are converted to distances appearing as a radial distribution function shifted by the phase shift (ca. ~0.4

Å) which is due to the photoelectrons passing through the electron clouds of the aborbing and scattering atoms.

In an effort to eliminate high frequency noise and isolate single shells of atoms, a Fourier filter is applied backtransforming the data into k-space. The backtransformed data can then be fit to Equation 2-3 to obtain the contribution from individual shells. EXAFS data presented here is fit as specified in the figure legends (backtransformed from ca. ~1 to 2 Å for coordinated atoms and 0.1 to 4.0 Å for full characterization). Fits are conducted using the least-squares engine of IFEFFIT (IFEFFIT is open source software available from http://cars9.uchicago.edu/ifeffit) that is distributed with Sixpack (Six pack is available from http://ssrl.slac.stanford.edu/~swebb/sixpack.htm). Data was fit to the unfiltered data to verify results.

Accurate curve fits require correct amplitude and phase functions for the backscattered photoelectrons. All amplitude and phase functions were obtained using the *ab initio* routines of FEFF 8.10. [12] The scale factor (S_c) and the shift in energy (ΔE_0) for each absorber-scatterer pair were calibrated using experimental EXAFS data of structurally known compounds. Specifically, N_s and R_{as} were fixed to values derived from crystal structures and S_0, ΔE_0, and σ_{as}^2 were varied. Models used to calibrate the following studies were zinc tetrakismethylimadazole, $ZN(MeIm)_4$,[13] zinc tetramesitylthiolate, $Zn(SMes)_4$, cobalt bis-trispyrazolylborate, $Co(Tp)_2$, and cobalt tetramesitylthiolate, $Co(SMes)_4$, for Zn-N, Zn-S, Co-N, and Co-S absorber-scatterer pairs respectively. Optimal values for the scale factors and ΔE_0 were: Zn-N $S_c = 0.78$, $\Delta E_0 = -21$, Zn-S $S_c = 0.91$, $\Delta E_0 = -21$, Co-N $S_c = 0.74$, $\Delta E_0 = -11$, and Co-S $S_c = 0.85$, $\Delta E_0 = -11$ when E_0 in equation 2-2 was set to the values mentioned earlier. These optimized values

were used with samples of unknown structure by keeping S_c and ΔE_0 constant and varying R_{as} and σ_{as}^2.

In summary, EXAFS can provide information about the distance, coordination number, identity and relative disorder of atoms surrounding the absorber, but the accuracies and precision of each of these values vary. The most accurate of these values are the distances between the absorber-scatterers with accuracies of ±0.01 Å and precision of ± 0.005 Å. The identity of the neighboring scatterer can only be determined to the nearest row of the periodic table, which easily distinguishes nitrogen and sulfur but is unable to distinguish nitrogen from oxygen. This is a direct result of the dependence of the phase and amplitude on the sizes of the relative scattering atoms. The resolution of separating two identical shells of atoms from each other is dependent on the k-range of the data as shown in Eq. 2-4,

$$\Delta R = \frac{\pi}{2\Delta k} \qquad \text{Eq. 2-4}$$

where ΔR and Δk are the resolution and k- ranges of the data. [14] The coordination number has an accuracy of ± 25% which corresponds to ± 1 atoms.

The variables within the EXAFS equation are highly correlated. The amplitude is dependent on the coordination number, scatterer identity and disorder of the absorber-scatterer pair. A large Debye-Waller factor may indicate the coordination number is too high or the shell is composed of two separate shells of atoms. The scale factor also contributes to amplitude, and a low S_c will over estimate the coordination number. The phase term is dependent on the absorber-scatterer distance and the scatterer identity, which complicates the identification of scattering atoms. With these correlations, care must be exercised to produce an accurate fit.

The number of independent data points, N_{idp} in a data set is defined by Eq. 2.5. [15]

$$N_{idp} = \frac{2\Delta k \Delta R}{\pi} + 2 \qquad \text{Eq. 2-5}$$

This equation is a measure of the total information content present in the data and represents the maximum number of parameters that can be determined by a fit to the spectrum. For the first shell of scatterers in a typical EXAFS spectrum, N_{idp} can vary from 9 to 12 depending on the width of the peak, DR, and the quality of the data, Δk. Five variable parameters are available in Eq.2-3 (N_s, R_{as}, σ_{as}^2, S_c, ΔE_0) for a single shell of atoms. The typical value of ~10 idp ($\Delta k \sim 11$, $\Delta R \sim 1.2$) allows for a single shell of atoms to be over-determined. Increasing the number of scattering shells to two, the maximum number of variables would equal the independent data points. Adding a third shell, would increase the number of variables beyond the information content of the data, under-determining the fit. For fits provided in this document, the number of variables per shell of scatterers was limited to R_{as}, σ_{as}^2. In all cases, the number of variable parameters never exceeded the number of independent data points.

The quality of fit is determined in IFEFFIT by a R-factor, defined by Eq. 2-6,

$$R = \frac{\sum_{i=1}^{N} \left\{ \left[\mathrm{Re}(\chi_{i\,calc}) \right]^2 + \left[\mathrm{Im}(\chi_{i\,calc}) \right]^2 \right\}}{\sum_{i=1}^{N} \left\{ \left[\mathrm{Re}(\chi_{i\,obs}) \right]^2 + \left[\mathrm{Im}(\chi_{i\,obs}) \right]^2 \right\}} \qquad \text{Eq. 2-6}$$

where Re and Im represent the real and imaginary components of the EXAFS data. [16] The equation is the sum-of-squares measure of the fractional misfit of the data. This

'goodness of fit' is not dependent on N_{idp}, the number of variables, or the measurement uncertainty. It is only dependent on how well the fit matches the data.

Experimental Techniques

The basic experimental setup employed in collecting EXAFS data has the same components as a fluorescence experiment. There is a light source, a monochromator, the sample, and a detector. The light source is the highly collimated, 'white' x-ray radiation available at the National Synchrotron Light Source. The light is made uniform with a series of slits. The energy is selected as the beam passes through a double-crystal monochromator which keeps the outgoing beam parallel to the incident beam. The intensity of the radiation is measured with a series of ionization chambers I_0, I_1, and I_2. Energy calibration is achieved by passing a portion of the beam through a metal foil of the appropriate element. Spectra may be collected either as a transmission ($\mu_T = \ln (I_0/I_1)$ or a fluorescence experiment ($\mu_F = \ln (I_F/I_0)$.

The energy range requirement for biological samples (2.5 – 25 keV) can be obtained with conventional x-ray tubes, a rotating anode, or synchrotron radiation, but the photon flux at a synchrotron radiation sources make it ideal for metalloprotein studies. All data reported here were recorded at Beamline X3B at the National Synchrotron Light Source at Brookhaven National Lab.

Energy selection in this particular setup is accomplished using Bragg reflection from single crystals (Eq. 2-7).

$$n\lambda = n\left(\frac{hc}{E}\right) = 2d \sin\theta \qquad \text{Eq. 2-7}$$

In Equation 2-7, n is the order of reflection, l is the wavelength, E is the energy of the diffracted ray, θ is the angle between the Bragg planes, and d is the spacing between the crystal lattice planes. Si(111) crystals are used (d= 3.14 Å) at X3B in a double crystal arrangement, allowing the reflected beam to exit parallel to the incident beam. Tuning the energy is accomplished by rotating the crystals relative to the incident beam.

For flat crystal monochromators, the energy resolution is given by Eq. 2-8,

$$\Delta E = E(\Delta\theta)\cot\theta \qquad \text{Eq. 2-8}$$

where θ is the Bragg angle at energy E and Δθ is the spread in x-rays passing through the monochromators. [11, 17] For synchrotron radiation, Δθ is the vertical collimation of the entering x-ray beam. With this relationship, the vertical aperture is inversely proportional to the energy resolution. Thus, it is highly desirable to operate with as small of a vertical aperture as possible to maintain adequate photon flux. Additionally, moving to a smaller d-spacing (*i.e.*, Si(220), 1.92Å) will increase energy resolution.

The monochromator selected energy is not the only reflected energy. Higher order harmonics (n>1) are also reflected. Harmonic rejection can be accomplished by either detuning or use of an inline mirror. The first method involves placing the crystals slightly nonparallel with respect to one another. This method will reduce the harmonic intensities to negligible levels while reducing the primary energy by ~50% of the original intensity. The second method requires the use of a nickel coated mirror which reflects the primary energy. However, this method cannot be used with all elements due to the nickel coating. In particular, cobalt and nickel spectra are distorted in the region where the mirror absorbs. [18, 19]

As noted earlier, X-ray absorption data may be collected either as transmission or fluorescence spectra. With high concentration samples (solids or solutions containing greater than 10 mM of the absorbing element), the transmission setup is optimal. The absorption coefficient, μ, can be measure by Beer's law, Eq. 2-9,

$$A = A_0 \exp(-\mu x) \qquad \text{Eq. 2-9}$$

where x is sample thickness, A_0 is the intensity of incident x-rays, and A is the intensity of transmitted x-rays. The intensities of the x-rays are collected as a function of energy (ln A/A_0 vs. E). The x-ray intensities are measured using gas ionization detectors, which consist of x-ray transparent windows and two charged plates filled with an inert, ionizable gas. X-rays pass through the chamber, ionize the gas, and generate a current which is proportional to the x-ray intensity. The current is amplified and measured using a VDC.

Dilute materials (~ 1 mM) were analyzed by fluorescence. At energies above the K-edge, the ionized atoms relax by emitting a fluorescent x-ray photon. This fluorescence is created when the hole left by the photoelectron is occupied by an electron from the n = 2 level emitting fluorescence (Kα fluorescence). The energy of this fluorescence is lower than that of the absorption edge and can be isolated with a photon-counting detector. The fluorescence is directly proportional to the absorption events, thus the plot directly mimics the absorption spectrum. This detection method allows for monitoring dilute systems because only the Kα fluorescence from the atom of interest is observed at the detector. All metalloprotein data was collected using a 13-channel solid-state germanium fluorescence detector.

The protein samples include a glassing agent (i.e., ~20% glycerol) in the aqueous buffers. Inclusion of the glassing agent prevents the formation of ice crystals. Ice crystals diffract x-rays dominating fluorescence, which results in unreliable data. Samples were contained in lexan cells with a mylar tape window and maintained at low (~ 20K) temperature on a cold finger. Each detector channel each examined, before being averaged. Those that contained artifacts were excluded from the average. All of the proteins presented here represent the average the average of 8-16 scans, typically incorporating 9-11 channels per scan.

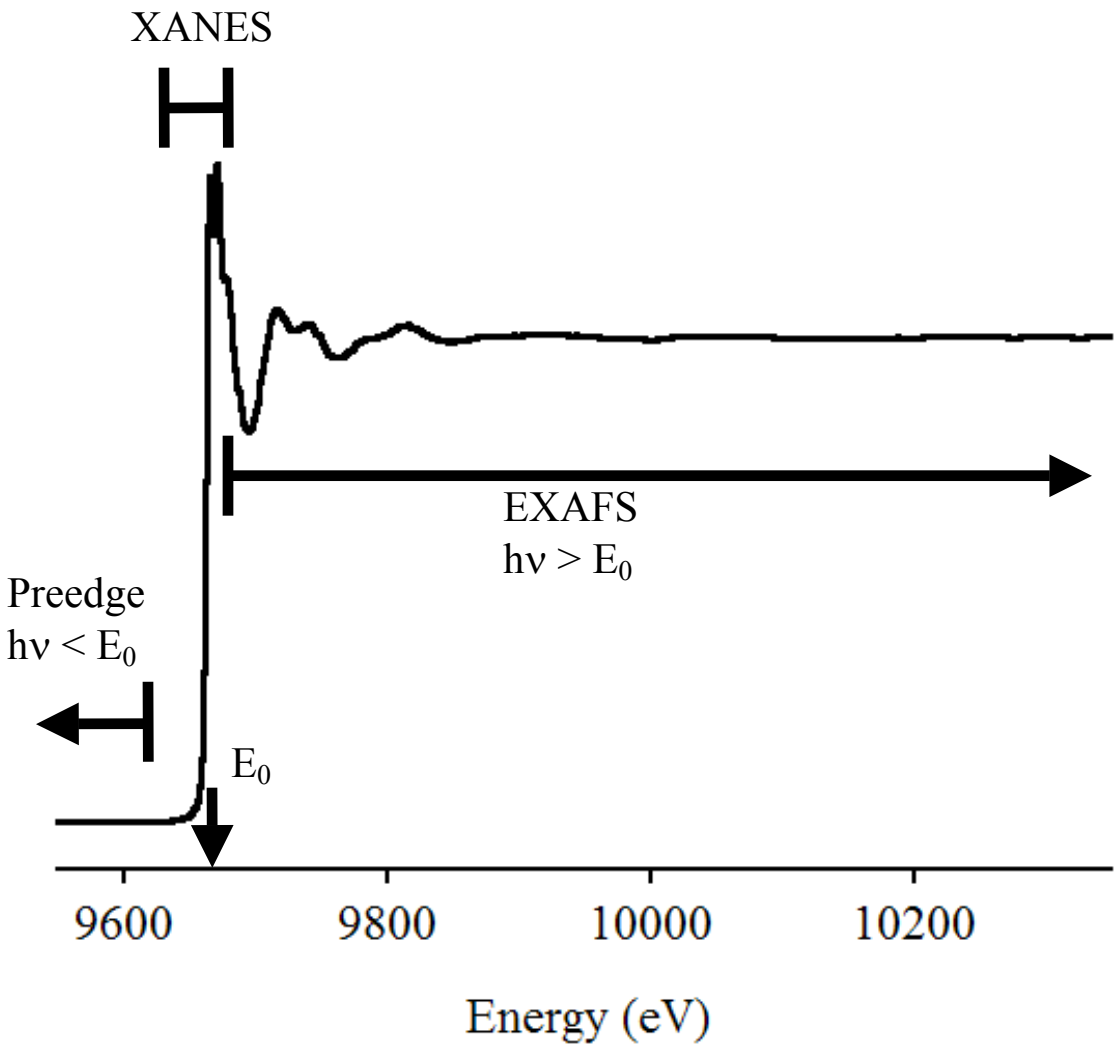

Figure 2-1: X-Ray Absorption Spectrum

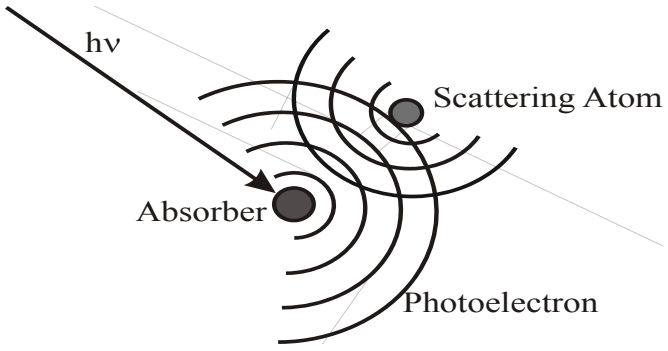

Figure 2-2: Physical Depiction of Absorption and Scattering

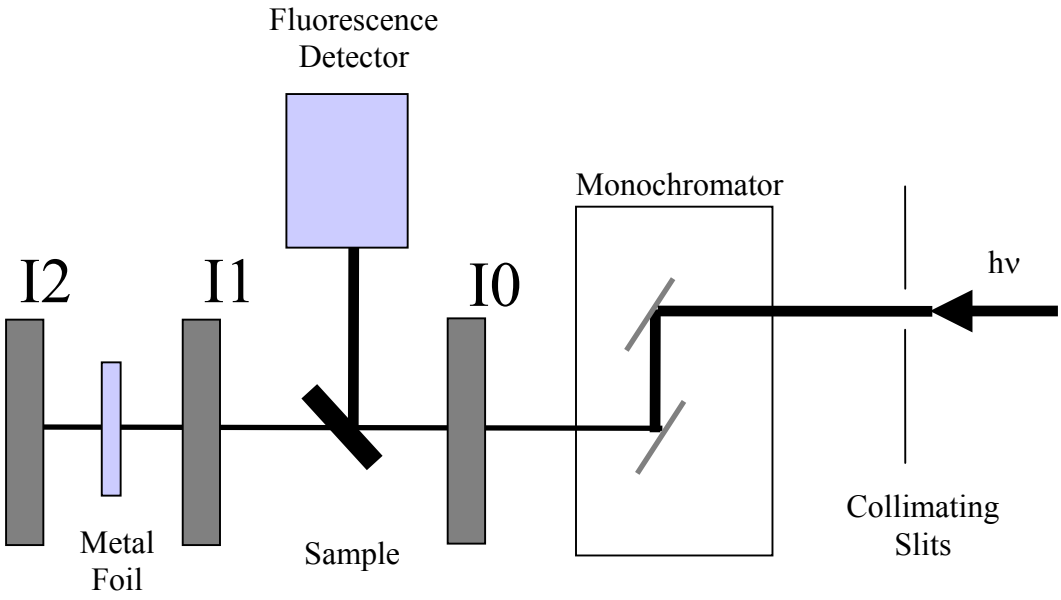

Figure 2-3: Schematic of EXAFS Beamline

1. Kossel, W., *Zum Bau der Röntgenspektren.* Z. Phys., 1920. **1**: p. 119-134.

2. Siegbahn, M., *The Spectroscopy of X-Rays*. 1925, London and New York: Oxford University Press.

3. Sayers, D.E., F.W. Lytle, and E.A. Stern, Adv. X-Ray Analysis, 1970. **13**: p. 248.

4. Sayers, D.E., F.W. Lytle, and E.A. Stern, Physical Review Letters, 1971. **27**: p. 1204.

5. Sayers, D.E., F.W. Lytle, and E.A. Stern, Non-Crystalline Solids, Journal of, 1972. **8-10**: p. 401.

6. Sayers, D.E., F.W. Lytle, and E.A. Stern, *Amorphous and Liquid Semiconductors*, ed. J.a.B. Stuke, W. 1974, London: Taylor & Francis.

7. Stern, E.A., Physical Review B: Solid State, 1974. **10**: p. 3027.

8. Stern, E.A., D.E. Sayers, and F.W. Lytle, Physical Review B: Solid State, 1975. **11**: p. 4836.

9. Stern, E.A., *X-Ray Absorption: Principles, Applications, Techniques of EXAFS, SEXAFS and XANES.* Chemical Analysis, ed. D.C. Koningsberger and R. Prins. Vol. 92. 1988, New York: John Wiley & Sons. 3.

10. Scott, R.A., *Physical Methods of Bioinorganic Chemistry: Spectroscopy and Magnetism*, ed. L. Que, Jr. 2000, Susalito, California: University Science Books. 465-503.

11. Scott, R.A., *Measurement of Metal-Ligand Distances by EXAFS.* Methods in Enzymology, 1985. **117**: p. 414-459.

12. Ankudinov, A.L. and J.J. Rehr, *Theory of Solid State Contributions to the X-Ray Elastic Scattering Amplitude.* Physical Review B, 2000. **62**(4): p. 2437-2445.

13. McClure, C.P., et al., *EXAFS Studies of the Zinc Sites of UDP-(3-O-acyl)-N-acetylglucosamine deacetylase (LpxC).* Inorganic Biochemistry, Journal of, 2003. **94**(1-2): p. 78-85.

14. Clark-Baldwin, K., et al., *The Limitations of X-Ray Absorption Spectroscopy for Determining the Structure of Zinc Sites in Proteins. When Is a Tetrathiolate Not a Tetrathiolate?* American Chemical Society, Journal of, 1998. **120**(33): p. 8401-8409.

15. Stern, E.A., *Number of Relevant Independent Points in X-Ray-Absorption Fine-Structure Spectra.* Physical Review B, 1993. **48**(13): p. 9825-9827.

16. Newville, M., *Feffit Manual: Using FEFF to model XAFS data*. 1998. p. 1-46.

17. Knapp, G.S., H. Chen, and T.E. Klippert, *Development of a laboratory EXAFS facility.* Review of Scientific Instruments, 1978. **49**(12): p. 1658-1666.

18. Brown, J., G.E., et al., *X-ray Absorption Spectroscopy and its Applications in Mineralogy and Geochemistry*. Revies in Mineralogy, ed. F.C. Hawthorne. Vol. 18. 1988, Washington, D.C.: Mineralogical Society of America.

19. Heald, S.M., *EXAFS with Synchrotron Radiation*. Chemical Analysis, ed. D.C. Koningsberger and R. Prins. 1988, New York: Wiley & Sons.

Chapter III

Spectroscopic and Mechanistic Studies on Metallo-β-lactamase Bla2 from *Bacillus anthracis*

The following work was published in Megan J. Hawk, Robert M. Breece, Christine E. Hajdin, Katherine M. Bender, Zhenxin Hu, Alison L. Costello, Brian Bennett, David L. Tierney, and Michael W. Crowder. Journal of the American Chemical Society, 2009. **131**(30): p. 10753-10762.

The author's contribution to the following discussion was collection, analysis, and interpretation of the EXAFS on Bla2. Megan Hawk contributed the protein preparation, NMR spectroscopy, kinetics, and optical spectroscopy. Brian Bennett contributed the EPR spectroscopy collection and interpretation.

Introduction

Anthrax is a disease that affects cattle and other herbivores and is caused by the spore-forming bacterium *Bacillus anthracis*. [1] Anthrax infections in humans lead to dark pustules on the skin, and are most commonly caused by contact with infected animals. However, anthrax infections can also be caused by ingestion or inhalation of *B. anthracis* spores. The potential for airborne transmission has led to the development of anthrax as a potential biological warfare agent, [2] and *B. anthracis* has been labeled as a

category A bioterrorism agent by the Centers of Disease Control and Prevention (CDC). [3]

Two significant anthrax outbreaks are on record due to non-environmental sources. The accidental release of military-grade anthrax in Sverdlovsk, USSR in 1979 caused at least 62 deaths. [4] In October, 2001, the Washington, D. C. Processing and Distribution Center of the U.S. Postal Service, and several congressional offices, were contaminated with a highly-processed form of anthrax from the Ames strain. More than 2,000 workers were exposed, leading to 22 infections and 11 deaths. [3] Currently, the CDC recommends a 60 day antimicrobial regimen of ciprofloxacin, doxycycline, or amoxicillin for anthrax infections. [2] Cephalosporins, trimethoprim, and sulfamethoxazole are not prescribed, due to the suspected resistance to these drugs. Recently, the Sterne strain of *B. anthracis* has been reported to produce both a class A (Bla1) and a class B (Bla2) β-lactamase. [5]

Currently, over 50% of the antibiotics prescribed by physicians are β-lactam-containing compounds, such as penicillins, cephalosporins, and carbapenems. [6] However, an increasing number of bacterial pathogens show resistance to β-lactam antibiotics, threatening their efficacy into the future. The most common pathway for resistance is the bacterial production of β-lactamases, which hydrolyze the four-membered ring in β-lactam antibiotics, rendering them ineffective. [7, 8] To date, over 400 β-lactamases have been described, and these enzymes have been classified into four subgroups (A-D). [8] While exhibiting different kinetic and inhibition properties, all group A, C, and D β-lactamases utilize an active site serine to perform nucleophilic attack on the substrate. The serine β-lactamases (SβLs) are the most clinically-

significant, and there are some clinical inhibitors that are active towards a majority of the enzymes in these groups. [8]

In contrast, the group B β-lactamases, often referred to as metallo-β-lactamases or MβLs, require 1-2 Zn(II) ions for catalytic activity.[9, 10] Approximately 40 MβLs have been reported, leading to their further classification into 3 subgroups. [11] The B1 enzymes require 1-2 Zn(II) ions for full activity, and prefer penicillins as substrates. They bind one Zn(II) in the Zn_1 (or 3H) site, which is made up of His116, His118, His196, and a solvent-derived ligand that bridges the two metal ions, and one Zn(II) in the Zn_2 (or DCH) site, made up of His263, Asp120, Cys221, the bridging solvent, and a terminally-bound water. Subclass B1 is represented by BcII from *Bacillus cereus*, CcrA from *Bacteroides fragilis*, and IMP-1 from *Pseudomonas aeruginosa*. The B2 enzymes, represented by CphA from *Aeromonas hydrophila* and imiS from *Aeromonas sobria*, require only one Zn(II) for full activity, prefer carbapenems as substrates and bind the catalytic Zn(II) in the Zn_2 site. The B3 enzymes generally require two Zn(II) ions for full activity, prefer cephalosporins as substrates, bind one Zn(II) in the canonical Zn_1 site and one Zn(II) in a modified Zn_2 site where Cys221 is replaced by His121, and are represented by L1 from *Stenotrophomonas maltophilia* and FEZ-1 from *Legionella gormanii*. Recently, a new member of the B3 subclass has been reported, and unlike its brethren, GOB from *Elizabethkingia meningioseptica* is a mono-Zn enzyme that binds metal at the Zn_2 site. [12]

Although the Sterne strain of *B. anthracis* has not caused the kind of human infection that the Ames and Sverdlovsk strains have, transfer of the Bla2 gene to a more pathogenic *Bacillus* is expected to be facile. Bla2 shares 89% sequence identity and 92%

sequence homology with BcII, [5, 13] and it would seem that all structural, mechanistic, and computational studies already reported for BcII would be applicable to Bla2. In spite of having very similar amino acid sequences, steady-state kinetic constants reported for Bla2 and BcII are different, [5, 14] and several active site amino acids (IIe39, Thr182 and Gly151) in BcII are not conserved in Bla2. In addition, there is conflicting data on BcII, [15-18] and it is not clear which set of data, if either, applies to Bla2.

We report here detailed studies to characterize recombinant Bla2 from *B. anthracis*. The metal content of the enzyme was ascertained with ICP-AES, and the steady-state kinetic constants of various analogs of the enzyme, with a range of substrates, were determined. To probe the structure of Bla2, the mono- and di-Co(II) analogs were prepared and characterized by UV-Vis, ^{1}H NMR, EPR, and EXAFS spectroscopies. These studies are complemented by EXAFS of the mono- and di-Zn(II) enzymes. Together the data demonstrate that metal binding by Bla2 follows distinct pathways, dependent on the identity of the metal ion (Co(II) or Zn(II)), and that the reactivity of the Zn- and Co-containing enzymes are quite different.

Experimental Procedures

Materials. The pET24bOmpA-Bla2 over-expression plasmid was generously supplied by Professor Timothy Palzkill of the Baylor School of Medicine, [5] and *E. coli* strain BL21(DE3) was purchased from Novagen, Madison, WI. A Minitan II concentrator system was purchased from Fisher Scientific, Pittsburgh, PA, with 1000 NMWL plates from Millipore, Bedford, MA. All chromatographic steps were conducted with a fast protein liquid chromatography (FPLC) system purchased from Amersham Pharmacia

Biotech. Nitrocefin and cefaclor were purchased from Becton Dickinson and Sigma, respectively. Meropenem and imipenem were donated by Zeneca Pharmaceticals, Wilmington, DE and Merck and Co., Rahway, NJ, respectively.

Over-Expression, Purification, and Biochemical Characterization. The pET24b-OmpA-Bla2 plasmid was transformed into *E. coli* BL21(DE3) cells via electroporation. Colonies from the transformation were used to inoculate 10 ml of LB medium containing 25 μg/ml kanamycin, and the culture was shaken overnight at 37 C. The overnight culture was used to inoculate 4x1L of LB medium containing 25 μg/ml kanamycin at 37 C, which were shaken at 37 C until reaching an optical density at 600 nm of 0.75-0.85. Protein production was induced with 1 mM isopropyl-β-*D*-thiogalactopyranoside (IPTG), and the cultures were allowed to shake overnight at 25 C.

The resulting cells were centrifuged (10 min at 7500 xg), and the supernatant was collected. The protein solution was kept on ice and concentrated with a Minitan II system equipped with 1000 NMWL plates until the volume reached *ca.* 50 ml. The concentrated protein mixture was centrifuged (30 min at 14500 xg), and the supernatant was dialyzed versus 2L of 50 mM Hepes, pH 6.5, overnight at 4 C. The supernatant was centrifuged (30 min at 14,500 xg) to remove insoluble matter and loaded onto an SP-Sepharose column (25 ml bed volume), which was pre-equilibrated with 50 mM Hepes, pH 6.5. Bound proteins were eluted with a 0-1 M NaCl gradient in 50 mM Hepes, pH 6.5, at 2 ml/min. Fractions (6 ml) containing Bla2, as determined by SDS-PAGE, were pooled and concentrated with an Amicon ultrafiltration cell equipped with a YM-10 membrane. SDS-PAGE gels were used to ascertain protein purity. The molecular mass of recombinant Bla2 in 50 mM Hepes, pH 6.5, was determined by MALDI-TOF mass

spectrometry. Amino acid analyses of Bla2 were conducted by the Protein Separation and Analysis Laboratory at Purdue University, West Lafayette, IN.

Metal Analyses. The metal content of Bla2 was determined using a Varian Liberty 150 inductively coupled plasma spectrometer with atomic emission detection (ICP-AES). Bla2 samples were diluted to 10 μM or 20 μM in 50 mM Hepes, pH 6.5. Calibration curves of five standards (Zn(II), Cu(II), Ni(II), Mn(II), Co(II), and Fe) were used to quantify the metal ion concentrations in Bla2 samples, as previously reported. [19]

Steady-State Kinetics. Steady-state kinetic studies were conducted at 25 C in 50 mM Hepes, pH 6.5, on a Hewlett-Packard model 5480A diode array spectrophotometer. The molar absorptivities of the substrates used were $\Delta\varepsilon_{485nm}$ = 17,400 $M^{-1}cm^{-1}$ for nitrocefin, $\Delta\varepsilon_{280nm}$ = -6,410 $M^{-1}cm^{-1}$ for cefaclor, $\Delta\varepsilon_{305nm}$ = 7,600 $M^{-1}cm^{-1}$ for meropenem, and $\Delta\varepsilon_{300nm}$ = -9000 $M^{-1}cm^{-1}$ for imipenem. Substrate concentrations ranged from 10 to 200 μM, and the enzyme concentration was held fixed at ca. 10 nM. Steady-state kinetic constants were determined as described previously. [19]

Preparation of apo-Bla2. Bla2 (1-2 ml of 1 mM as-isolated enzyme) was dialyzed versus 4x2L (12 hours each) of 15 mM Hepes, pH 6.5, containing 10 mM EDTA at 4 C. EDTA was removed by dialysis versus 2x2L of Chelex-treated, 15 mM Hepes, pH 6.5, containing 150 mM NaCl, followed by 2x2L of Chelexed 15 mM Hepes, pH 6.5, containing 100 mM NaCl, for 6 h each, at 4 C. After the last dialysis step, the protein solution was centrifuged (30 min at 14,500 xg) to remove precipitated protein and then concentrated by ultrafiltration to 1-2 ml. The resulting solution was passed through a Sephadex G-25 column, using Chelex-treated 15 mM Hepes, pH 6.5, containing 100 mM

NaCl, as eluent. Fractions were collected, and samples containing Bla2 were pooled and concentrated, prior to the determination of metal content by ICP-AES.

UV-Vis Spectrophotometry. Apo-Bla2 (ca. 1 mM) in Chelexed 15 mM Hepes, pH 6.5, containing 100 mM NaCl was titrated with $CoCl_2$ (Strem Chemicals, 99.999 %). Samples of Bla2 with 1 or 2 eq of added Co(II) were incubated on ice for 5 min. before being centrifuged (10 minutes at 14,500 x g) to remove precipitated protein. Difference spectra were obtained by subtracting the spectrum of apo-Bla2 from those of the Co(II)-added samples.

Stopped-Flow UV-Vis Studies. Diode array UV-Vis spectra were collected (200 – 700 nm) at 4 C on an Applied Photophysics SX18-MVR stopped-flow spectrophotometer. The buffer used in these experiments was 50 mM Hepes, pH 6.5, and the substrates were nitrocefin, cefaclor, and imipenem. Substrate concentrations ranged from 10 to 50 μM, and the concentration of 1Zn-Bla2 was held constant at 20 μM. All experiments were conducted in triplicate, and the data presented here represent the average of these multiple data sets. Stopped-flow absorbance data were converted to concentrations as previously described, [20] and the data were corrected for the instrument dead time of 2 ms. The resulting progress curves were fitted to single exponentials, and the resultant values of k_{obs} were plotted against substrate concentration. When using nitrocefin as substrate, these plots were hyperbolic and fitted to $k_{obs} = K_1[S]k_2 / (K_1[S] + k_{-2})$, as previously described. [21] When using cefaclor and imipenem as substrates, these plots were linear and fitted to $k_{obs} = k_1[S] + k_{-1}$. The progress curves were simulated using KINSIM, as previously described. [22, 23] Dynafit was used to

verify the simulations, [24] and ProK was used to obtain errors for the rate constants, as previously described. [22]

EPR spectroscopy. EPR spectra were recorded using a Bruker EleXsys E600 EPR spectrometer equipped with an Oxford Instruments ITC4 temperature controller and an ESR-900 helium flow cryostat. A Bruker ER-4116DM cavity was used, with a resonant frequency of 9.63 GHz (in perpendicular mode) and 10 G (1 mT) field modulation at 100 kHz was employed. Other recording conditions are given in the legend to Figure 4. Computer simulations of EPR spectra were carried out using the matrix diagonalization program Xsophe [25] (Bruker Biospin GmbH) assuming a spin Hamiltonian $\mathbf{H} = \beta \mathbf{g.B.S} + \mathbf{S.D.S}$, where $S = {}^3/_2$ and $D > 0$ corresponds to an $M_S = |\pm {}^1/_2\rangle$ ground state Kramers' doublet, as previously described. [22, 26, 27]

NMR Spectroscopy. ^{1}H NMR spectra were collected at 298 K on a Bruker Avance 500 spectrometer operating at a proton frequency of 500.13 MHz. Samples of Bla2 in either 10 % or 90 % H_2O were 1 mM in Chelex-treated, 15 mM Hepes, pH. 6.5, containing 100 mM NaCl. All samples were incubated for 30 min on ice after D_2O addition and centrifuged, before being placed in the NMR tube. Spectra were collected using a presaturation pulse sequence (zgpr) for water suppression, a recycle time of 41 ms, and a sweep width of 400 or 800 ppm. Prior to Fourier transformation, the FID was apodized with an exponential function that resulted in an additional line broadening of 80 Hz.

X-Ray Absorption Spectroscopy. Samples of Bla2 (~ 1 mM, including 20% (v/v) glycerol added as a glassing agent) were loaded in Lucite cuvettes with 6 μm polypropylene windows and frozen rapidly in liquid nitrogen. X-ray absorption spectra

were measured at the National Synchrotron Light Source (NSLS), beamline X3B, with a Si(111) double crystal monochromator; harmonic rejection was accomplished using a Ni focusing mirror. Fluorescence excitation spectra for all samples were measured with a 13-element solid-state Ge detector array. Samples were held at ~ 15 K in a Displex cryostat during XAS measurements. X-ray energies were calibrated by reference to the absorption spectrum of the appropriate metal foil, measured concurrently with the protein spectra. All of the data shown represent the average of ~ 12 total scans, from two independently prepared samples each. Data collection and reduction were performed according to published procedures [28] with E_0 set to 9680 eV for Zn and 7735 eV for Co. The Fourier-filtered EXAFS were fit to Equation 1 using the nonlinear least-squares engine of IFEFFIT that is distributed with SixPack. [29, 30]

$$\chi(k) = \sum \frac{N_{as} A_s(k) S_c}{kR_{as}^{\ 2}} \exp(-2k^2 \sigma_{as}^{\ 2}) \exp(-2R_{as}/\lambda) \sin[2kR_{as} + \phi_{as}(k)] \qquad (1)$$

In Eq. 1, N_{as} is the number of scatterers within a given radius (R_{as}, ± σ_{as}), $A_s(k)$ is the backscattering amplitude of the absorber-scatterer (*as*) pair, S_c is a scale factor, $\phi_{as}(k)$ is the phase shift experienced by the photoelectron, λ is the photoelectron mean free-path, and the sum is taken over all shells of scattering atoms included in the fit. Theoretical amplitude and phase functions, $A_s(k)exp(-2R_{as}/\lambda)$ and $\phi_{as}(k)$, were calculated using FEFF v. 8.00. [31] The scale factor (S_c) and ΔE_0 for Zn-N (S_c = 0.78, ΔE_0 = -21 eV), Zn-S (0.85, -21 eV), Co-N (0.74, -26 eV) and Co-S (0.85, -26 eV) scattering were determined previously and held fixed throughout this analysis. [28, 32] Fits to the current data were obtained for all reasonable integer or half-integer coordination numbers, refining only R_{as} and σ_{as}^2 for a given shell. Multiple scattering contributions from

histidine ligands were approximated according to published procedures, fixing the number of imidazole ligands per metal ion at half-integral values while varying R_{as} and σ_{as}^2 for each of the four combined ms pathways (see Table 4). [28, 32] Metal-metal (Co-Co and Zn-Zn) scattering was modeled by fitting calculated amplitude and phase functions to the experimental EXAFS of $Co_2(salpn)_2$ and $Zn_2(sapln)_2$.

Results

Biochemical Characterization

Overexpression and Purification of Bla2. Previously, Palzkill and co-workers designed a pET24-based over-expression plasmid that produces an OmpA-Bla2 fusion protein. [5] The fusion protein is ultimately exported to the outer membrane, where cleavage of the fusion protein deposits recombinant Bla2 directly into the growth medium. Using our procedure, 17-23 mg of > 95 % pure Bla2 can be obtained from 1 liter of LB medium (Figure 1). Amino acid analyses indicate an extinction coefficient (ε_{280}) of 25,400 $M^{-1}cm^{-1}$, and the MALDI-TOF MS exhibits an m/z of 24,249 amu (25,360 predicted, based on the amino acid sequence). [13] Metal analysis demonstrates the as-isolated enzyme contains 1.0 $\pm$ 0.2 equivalents of Zn and < 0.1 equivalent of Co, Cu, Ni, Mn, or Fe. Incubation of the as-isolated enzyme with a 4-fold excess of Zn(II), followed by Chelex treatment to remove unbound and loosely bound metal ions, resulted in an enzyme that tightly bound 1.4 $\pm$ 0.1 eq of Zn. In general, the presence of excess Zn

in the medium destabilized the dilute enzyme, often resulting in irreversible precipitation; similar effects were not observed at higher (> 0.5 mM) concentrations.

Steady-State Kinetics of Bla2. Previous kinetic studies by Palzkill, *et al* were conducted in 50 mM Hepes, pH 7.5, containing 50 μM Zn(II) and 20 μg bovine serum albumin (BSA). [5] In initial attempts to measure steady-state kinetics under these conditions, we found the enzyme to be unstable. Inclusion of BSA did not stabilize the enzyme in our hands. However, Bla2's predicted pI of 7.6 led us to speculate that lowering the pH from 7.5 would stabilize the protein. Reproducible steady-state kinetic data was obtained at pH 6.5 in 50 mM Hepes. It is important to bear in mind that the steady-state kinetic buffers contain ~ 100 nM Zn(II), [33] even if the buffers are Chelex-treated, while the assayed enzyme concentration is 1-10 nM. Given this, it is difficult to state with certainty the exact metal content of the Zn-Bla2 analogs in Table 2. Within theses limits, as-isolated Bla2, which most closely resembles the mono-zinc enzyme, hydrolyzed nitrocefin, imipenem, cefaclor, and meropenem with k_{cat} values ranging from 24 to 92 s^{-1} and K_m values ranging from 25 to 110 μM (Table 1).

Apo-Bla2 was prepared by dialysis against EDTA, followed by exhaustive dialysis to remove residual EDTA (see Materials and Methods). Apo-Bla2 prepared in this way contained no detectable Zn, Co, Mn, or Fe, as indicated by ICP-AES. Direct addition of 1 or 2 eq of Zn(II) to the apoenzyme gave the 1Zn- and ZnZn-analogs of Bla2 that were used for metal-dependent steady state kinetic studies (Table 2). 1Zn-Bla2 exhibited a k_{cat} of 32 s^{-1} and a K_m of 28 μM at pH 6.5 using nitrocefin as the substrate. The k_{cat} of this enzyme was ca. 30 % less than that of as-isolated Bla2 (Table 1). Addition of a second eq of Zn(II) (ZnZn-Bla2) resulted in an increase in both k_{cat} and K_m, while

further additions of Zn(II) led to a steady drop in k_{cat}, consistent with the instability of the dilute enzyme in the presence of excess Zn(II) noted above. The analogous mono- and di-Co(II) enzymes (1Co-Bla2 and CoCo-Bla2, respectively) gave steady-state values for both k_{cat} and K_m that were similar to the corresponding Zn enzymes (Table 2).

Stopped-Flow UV-Vis Kinetic Studies. Stopped-flow kinetic studies were conducted on 1Zn-Bla2 with three substrates (nitrocefin, cefaclor, and imipenem). Similar studies were not performed on ZnZn-Bla2, due to its instability in dilute solution. In the reaction of 1Zn-Bla2 (20 μM) with nitrocefin (10 – 50 μM), only two distinct features are observed: one at 390 nm that decreases with time, corresponding to loss of substrate, and one at 485 nm that increases with time, corresponding to product formation (Figure 2). No transitory absorbance was observed at 665 nm, corresponding to a stable intermediate previously observed in reactions of nitrocefin with CcrA [34] and L1, [20] but not with BcII. [35] Progress curves at 390 and 485 nm using 25 and 50 μM nitrocefin were fitted to single exponentials to obtain k_{obs}. A plot of k_{obs} vs. substrate concentration was hyperbolic, suggesting a rapid-equilibrium, two-step binding mechanism (Scheme 1). [21] The progress curves were simulated using KINSIM, the mechanism in Scheme 1, and the rate constants in Table 3 (Figure 2). The King-Altman method [36] was used to determine theoretical expressions for k_{cat} and K_m, based on the mechanism in Scheme 1, and the resulting steady-state kinetic constants (k_{cat} = 7.4 s^{-1} and K_m = 62 μM) were similar to those determined in steady-state kinetic studies (Table 1).

Stopped-flow kinetic studies were also performed on 1Zn-Bla2 with imipenem and cefaclor. In these reactions, only the substrates could be observed. Unlike for nitrocefin, plots of k_{obs} vs. imipenem or cefaclor concentration is linear, suggesting one-

step binding mechanisms for both substrates (Scheme 2). [36] The resulting progress curves were simulated using KINSIM, the mechanism in Scheme 2, and the rate constants in Table 3. The King-Altman-determined theoretical expressions for k_{cat} and K_m give theoretical values for imipenem (k_{cat} = 35 s^{-1} and K_m = 194 μM) and cefaclor (k_{cat} = 15 s^{-1} and K_m = 150 μM) that are similar to those determined by steady-state kinetic studies (Table 1).

Metal Binding

Optical Spectroscopy. We first examined Co(II) binding by optical titration of apo-Bla2. The UV-visible difference spectra (*Co-bound – apo-Bla2*, Figure 3) show the Cys-S to Co(II) charge transfer transition at 320 nm (ε_{320} = 608 M^{-1} cm^{-1}) that is indicative of metal binding at the Zn_2 site, even at 0.5 eq of Co(II). Also apparent at 0.5 eq of Co(II) are the ligand field transitions (500 – 650 nm, ε_{550} = 218 M^{-1} cm^{-1}) normally associated with metal binding at the Zn_1 site (Figure 3). Each of these features increases linearly in absorbance as a function of added Co(II) (Figure 3, inset), suggesting that Co(II) distributes between the Zn_1 and Zn_2 sites with minimal difference in affinity. We were unable to obtain the optical spectrum of Bla2 containing 3 eq of Co(II) because the protein quickly precipitated, similar to prior observations from Co(II) titrations of CcrA. [37]

EPR Spectroscopy. EPR spectra from 1Co-Bla2 and CoCo-Bla2 were recorded under non-saturating, saturating, and rapid-passage conditions and are shown in Figure 4. The spectra from 1Co-Bla2 (Fig. 4A) and CoCo(II)-Bla2 (Fig. 4B) recorded under non-saturating conditions exhibited no resolvable rhombicity or ^{59}Co hyperfine structure, and

were characteristic of 5- or 6-coordinate Co(II) with at least one water ligand. Spectra recorded at high power and low temperature (Fig. 4D) did not reveal any $M_S = |\pm\ ^3/_2\rangle$ signals that would indicate tetrahedral Co(II). Slight differences were observed between the non-saturated spectra of 1Co-Bla2 and CoCo-Bla2. The difference spectrum (Figure 4C) revealed the presence of a second Co(II) species in CoCo-Bla2, indicating at least some preference for one site over the other, though this could not be quantified.

The rapid passage spectra of 1Co-Bla2 and CoCo-Bla2 (Fig. 4E) were indistinguishable in form and differed only in intensity, by a factor of 2. This indicates that the species that is responsible for this spectrum is the same in both 1Co-Bla2 and CoCo-Bla2, and that twice as much of it is present in CoCo-Bla2 than in 1Co-Bla2. These data are consistent with either a cooperative binding mechanism or a random mechanism with similar affinities for the sites, but are completely inconsistent with a sequential mechanism. Comparison of the normal, non-saturated spectrum of 1Co-Bla2 and the (*CoCo-Bla2* - *1Co-Bla2*) difference spectrum (Fig. 4C) shows that the spectrum of 1Co-Bla2 is sharper in the $g_\perp$ region, around 2000 G (200 mT). The derivative of the rapid passage spectrum (of either 1Co-Bla2 or CoCo-Bla2) is, in turn, sharper still than that of 1Co-Bla2; the former more likely represents a single chemical species and provides some direct evidence that the signal from 1Co-Bla2 contains more than one species.

Taken overall, then, the EPR data indicate that the signal from 1Co-Bla2 is likely due to two components, one of which can be isolated by recording the spectrum under rapid passage conditions for that signal, and another that is similar in line shape but could not be deconvoluted. Approximately 85% of the signal from CoCo-Bla2 consists of

Co(II) in the same environments, with the same distribution among those environments, as in 1Co-Bla2. These data indicate a binding mechanism that is largely either random or cooperative. A minor fraction of the Co(II) spin density in CoCo-Bla2, 15%, appears either to (i) indicate Co(II) that resides in a third, distinct environment or (ii) represent a slight difference in the distribution of Co(II) between two binding sites, or else (iii) is indicative of a broadening mechanism due to weak spin-coupling between Co(II) ions that is more pronounced in CoCo-Bla2 than in 1Co-Bla2. While the latter possibility would suggest random binding to sites with similar affinities, rather than cooperative binding, there was no additional evidence from parallel mode EPR (B0|B1, not shown) for weak magnetic coupling between the two Co(II) ions in CoCo-Bla2.

NMR Spectroscopy. The ^{1}H NMR spectrum of CoCo-Bla2 in 10 % D_2O shows five downfield shifted resonances between 35 and 85 ppm (Figure 5). The spectrum is nearly identical in appearance to that previously reported for di-Co BcII, [15] where each peak was assigned to a single proton, despite significant differences in linewidth and intensity. The ^{1}H NMR spectrum of Bla2 containing one eq of Co(II) is identical to that of CoCo-Bla2, although of lower signal-to-noise (Figure S8). In 90 % D_2O, four of the resonances of CoCo-Bla2 (78, 65, 49, and 44 ppm) disappear. With analogy to the crystal structure of BcII, we assign these four resonances to the NH protons of His116, His118 and His196 from the Zn_1 site and His263 of the Zn_2 site. The resonance at 42 ppm is not solvent-exchangeable and can be assigned to the meta proton of His118, which binds metal through the δN in BcII. This is consistent with the multiple Co(II) binding sites identified by EPR, and the observation of both the S→Co(II) CT band and the d→d bands,

both with one eq of Co(II), indicating that the first eq of Co(II) distributes between the two metal binding sites.

The NMR spectra of Bla2 are very similar to those previously reported for BcII, [15] with the notable exception of a resonance assignable to the β-CH_2 protons of a Co(II)-coordinated cysteine (spectra were recorded to 400 ppm). One possibility is that our procedure to prepare the ^{1}H NMR samples resulted in oxidation of Cys221 to the sulfoxide. Similar oxidation has been suggested for CcrA, [32] and an oxidized Cys221 has been observed in crystal structures of BcII [38] and VIM-2. [39]

Co K-Edge XAS. Comparing the EXAFS of 1Co-Bla2 and CoCo-Bla2 (Figure 6) shows little quantifiable difference, consistent with the optical, NMR and EPR studies described above. The major difference is in the height of the main peak, reflective of either higher coordination number or lower overall disorder in the first shell on addition of the second eq of Co(II). The shape, particularly the width, of the main feature is largely unchanged, and curve-fitting results suggest the latter interpretation (lower disorder) better reflects the apparent difference. Best fits for 1Co- and CoCo-Bla2 are shown in Figure 6, and summarized in Table 4. Detailed fitting results, including fits to unfiltered EXAFS, are presented in Supporting Information, Figure S1 and Table S1 for 1Co-Bla2, and Figure S2 and Table S2 for CoCo-Bla2.

The distributed binding indicated above leads to the expectation that both 1Co- and CoCo-Bla2 would reflect an average of the Zn_1 and Zn_2 coordination spheres, with 4 N/O and 0.5 S comprising the first shell. In both cases, inclusion of a partial sulfur scatterer dramatically improves the quality of the first shell fits. For 1Co-Bla2, the average first shell bond length is reflective of 4- or 5-coordination (Fit S1-1). While the

fit residual decreases nearly 3-fold (63 %) when the fit includes a mixed first shell of nitrogen and oxygen (compare Fits S1-1 and S1-2), the difference in refined distances (0.15 Å) is at the resolution of the data (0.14 Å). An even greater improvement is seen on addition of a sulfur scatterer (70 %, compare Fits S1-1 and S1-3). The three shell fit, including resolved N, O and S shells, results in an overall 83 % improvement from the single scattering fit (Fit S1-1 vs. S1-4), and 43 % over the N/O + S fit (Fit S1-1 vs. S1-4), although the refined N and O distances are outside the resolution of the data. For this reason, multiple scattering fits were conducted using a first shell of 4 N/O + 0.5 S and indicate an average of 2 His ligands per Co ion (Fit S1-5). Inclusion of a Co-Co vector in this fit leads to only 8 % improvement in the fit residual, suggesting a bridged bimetallic cluster is not present (Fit S1-6).

Similar results are obtained for CoCo-Bla2 (Fig. 6, Bottom, and Figure S2 and Table S2). The average first shell bond length is unchanged from 1Co-Bla2 (compare Fits S2-1 and S1-1). A mixed first shell of N and O leads to a 49 % improvement in fit residual with N and O distances at the resolution of the data (Fits S2-1 and S2-2) and inclusion of a partial sulfur scatterer leads to a 70 % improvement in the fit residual. Multiple scattering fits, using 4 N/O + 0.5 S to model the first shell, again indicate an average of 2 His ligands per Co ion. The appearance of the outer shell scattering would suggest some rearrangement on addition of the second Co(II) ion, but this information is outside the scope of the current analysis. Inclusion of a Co-Co vector in this fit leads to a 20 % improvement in fit residual, while increasing the number of variable parameters to 14 from 12 (a 17 % increase). The refined Co-Co distance is shorter than the Zn-Zn separation in similar systems, including this one (below), while it is expected, if present

to be slightly longer due to the modestly larger size of the Co(II) ion. We take this as evidence that the aquo bridge is replaced by one solvent on each metal ion in fully loaded CoCo-Bla2, in accord with our previous studies of CcrA. [32]

Zn K-Edge XAS. In contrast to the distributed binding observed with Co, the binding of Zn by Bla2 appears to be sequential. The Fourier transformed EXAFS for 1Zn-Bla2 shows much higher outer shell intensity than its ZnZn counterpart, which shows much better resolution in its outer shell scattering (Figure 7, Top). Qualitatively, this is consistent with binding of the first equivalent of Zn(II) in the Zn_1 site, bearing three His ligands. Population of the Zn_2 site would then be expected to (*i*) broaden the first shell with addition of the sulfur ligand, (*ii*) lower the overall outer shell scattering, as the average number of His ligands is reduced from 3 to 2 and (*iii*) sharpen the outer shell features as the dinuclear site becomes better organized. This description is fully consistent with the Fourier transforms presented in Figure 6.

The qualitative description presented above is also supported by the curve fitting results (best fits are shown in Figure 7 and Table 4, detailed results are shown Figure S3 and Table S3 for 1Zn-Bla2, and Figure S4 and Table S4 for ZnZn-Bla2), which show the Zn in 1Zn-Bla2 is coordinated by 4 N/O donors, including 3 His ligands. Inclusion of a partial sulfur scatterer does not significantly improve the fit (< 30 %), while resulting in an unreasonably short Zn-S distance (2.23 Å, compare Fits S3-1 and S3-2). Similarly, a mixed first shell of N and O donors leads to a minimal improvement in the fit residual, only slightly larger than simply increasing the number of variable parameters (compare Fits S3-3 and S3-4 to Fit S3-1), with a separation in Zn-N and Zn-O distances that is less than the resolution of the data. Multiple scattering fits indicate an average of 3 His

ligands per Zn, and inclusion of a Zn-Zn vector in this fit results in only 18 % improvement in fit residual with a relatively short refined Zn-Zn distance of 3.36 Å. Together, we take this as evidence that there is no population of the Zn_2 site in 1Zn-Bla2, and that there is not sub-populations of di-Zn and apo-Bla2.

In contrast, the coordination sphere of the average Zn(II) in ZnZn-Bla2 clearly includes 0.5 S donors, as well as 4 N/O. The average first shell bond length (in N/O only fits) increases by 0.05 Å over 1Zn-Bla2 (compare Fits S4-1 and S3-1), suggesting an increase in average coordination number and/or the presence of a larger scatterer. A mixed first shell of resolved Zn-N and Zn-O leads to a 70 % decrease in the fit residual, though the distances are right at the resolution of the data (Fits S4-1 and S4-2). Inclusion of 0.5 S with 4 unresolved N/O donors leads to an 88 % improvement in the fit residual (compare Fits S4-3 and S4-1), and a three-component N + O + S fit results in an overall 93 % reduction in residual. For simplicity, multiple-scattering fits were restricted to a first shell of 4 N/O + 0.5 S donors. The fits are consistent with the average number of imidazoles being reduced from 3 to 2 on addition of the second eq of Zn(II). Inclusion of a Zn-Zn interaction leads to a 43 % improvement in the fit residual, while increasing the number of variable parameters from 12 to 14. The refined Zn-Zn distance of 3.44 Å is the same as that seen in other resting state dinuclear MβLs by both XAS [40] and diffraction, [41-43] but very different from the 3.6-3.7 Å EXAFS-derived separation reported earlier for BcII. [44]

The discrepancy in metal-binding mechanisms followed by Bla2 led us to examine Zn binding by the B1 MβL CcrA from *B. fragilis*. The metal site in CcrA is analogous to Bla2 and, in light of our previous work on Co binding by CcrA, [32] we

expect the same pattern as Zn binding by Bla2 with the first metal ion exclusively populating the Zn_1 site. As can be seen in Figure 8 (Top), the FTs for 1Zn-CcrA and 1Zn-Bla2 are remarkably similar. The similarity of the FTs is reflected in the curve fitting results for 1Zn-CcrA (Table S5 and Figure S5), which are nearly identical to 1Zn-Bla2, including only minimal improvements on (*i*) addition of a partial sulfur scatterer (compare Fits S5-2 and S5-1), (*ii*) using resolved N and O shells (Fits S5-3 and S5-1), or (*iii*) inclusion of a Zn-Zn vector in multiple scattering fits (Fits S5-4 and S5-5).

At first glance, the similarity of Zn-loaded CcrA and Bla2 dissolves on loading the second eq of Zn(II). The main peaks in the EXAFS FTs for ZnZn-CcrA and ZnZn-Bla2 are strikingly different (Figure 8, Center), although the CcrA FT returns nearly to baseline at a point similar to Bla2. The overall curve fitting results indicate that the apparent difference in their FTs is an artifact of subtle differences in structure. The average first shell bond length increases on addition of a second Zn(II) to CcrA, though not as much as for Bla2, and the best fit with only N/O scatterers indicates an average coordination number of 4 (Fit S6-1). Inclusion of a partial sulfur scatterer improves the fit residual by 48 % (compare Fits S6-2 and S6-1), and this is a well-defined minimum (compare Fits S6-2 and S6-3). Qualitatively, this leads to a much better match of the main peak's amplitude, with a small shoulder that contributes to the first outer shell peak (Figure S6A), typically ascribed to M-His and/or M-C_{CO2}- scattering. The same fit, replacing the Zn-S with a Zn-C scattering path gives only a 32 % improvement (Fit S6-5 vs. Fit S6-1), while inclusion of both leads to an overall 66 % decrease in fit residual (Fit S6-4). The refined Zn-S distance for ZnZn-CcrA is 0.06 Å longer than that obtained for ZnZn-Bla2. Comparison of the combined Zn-S/Zn-C scattering in *k*-space for these two

scenarios (see Figure S7) shows that as the Zn-S and Zn-C distances converge, a partial cancellation effect leads to the lack of an obvious Zn-S interaction in the ZnZn-CcrA FT. [45]

Multiple scattering fits for ZnZn-CcrA indicate an average of 2 His ligands per Zn, and inclusion of a Zn-C_{CO2-} scattering path (increasing the number of variables from 14-16), leads to a modest 17 % improvement in R_f (compare fits S6-6 and S6-7). In both cases, addition of a Zn-Zn vector leads to $\geq$50 % improvement in the fit residual (compare Fit S6-6 to Fit S6-8, and Fit S6-7 to Fit S6-9). The refined Zn-Zn distance is, again, fully consistent with those observed for other resting di-Zn MβLs by XAS [40] and diffraction. [41-43]

Stopped-Flow of 1Zn- and 1Co-Bla2. The distributed binding of Co(II) by Bla2, as demonstrated above, cannot distinguish between potential populations of mono-Co(II) Bla2 (loaded in either the Zn_1 or the Zn_2 site) and a mixture of apo- and fully-loaded di-Co(II) Bla2. As can be seen in Figure 9, while 1Zn-Bla2 does not stabilize an intermediate with nitrocefin, 1Co-Bla2 clearly does. The lack of accurate values of K_m and k_{cat} for 1Co-Bla2 preclude the simulation of these data. However, in recent work with the dinuclear B3 MβL L1, we showed that occupation of the Zn_1 site was sufficient for catalysis, but both metal ions were needed to stabilize the nitrocefin-derived intermediate, [46] as originally described by Wang, *et al*, with ZnZn-CcrA. [34] Thus, the data in Fig. 9 indicate that there is a significant population of CoCo-Bla2 present at 1 eq Co(II) per protein, at least under turnover conditions.

Discussion

Biochemical Characterization. Previously, Palzkill and co-workers reported the over-expression and purification of recombinant Bla2. [5] In this protocol, the *ompA* gene was fused to the gene for Bla2, and this construct was designed to export Bla2 into the culture growth medium, requiring only cation exchange and Sepharose S-200 chromatographies to obtain 0.4 mg of purified Bla2 per liter of growth culture. To improve the yield, we modified the published purification protocol, using a Minitan ultrafiltration system to concentrate the crude protein solution. A similar protocol was used to purify recombinant CcrA, which is also exported into the growth medium during over-expression. [37] We then purified Bla2 using a single SP-Sepharose chromatographic step, yielding 17-23 mg of purified Bla2 per liter of growth medium.

The Zn(II) content of as-isolated Bla2, prepared in this way, was 1.0 $\pm$ 0.2 eq per protein, substantially lower than that reported for as-isolated BcII (1.4 – 1.8 eq) [15, 47] and CcrA (1.5 – 2.0). [32, 37, 48, 49] Addition of excess Zn(II) to the as-isolated enzyme, followed by extensive dialysis against metal-free buffer results in an enzyme that binds 1.4 $\pm$ 0.1 eq of Zn(II). In similar studies, BcII has been reported to tightly bind 2.0 $\pm$ 0.1 equivalents of Zn(II). [50] Given the two enzymes share 89 % sequence identity and 92 % sequence homology, [5] it is not clear why the metal contents of BcII and Bla2 are so different. A possible source of this discrepancy may lie in quantification of the enzymes. As determined by amino acid analyses, the extinction coefficient of Bla2 at 280 nm is 25,400 $M^{-1}cm^{-1}$, while that of BcII is 30,500 $M^{-1}cm^{-1}$, [50] a difference of 17 %. Using the smaller extinction coefficient of Bla2, a metal stoichiometry of 2.0 Zn(II) tightly bound to BcII would be reduced to ~ 1.7 eq. Alternately, using the larger

extinction coefficient of BcII, the metal stoichiometry of as isolated Bla2 would be reduced to ~ 0.8 eq Zn(II) per protein. This is inconsistent with the steady state kinetics, which would have been expected to show an increase in k_{cat} on further addition of Zn(II). Again, given the similarity in their amino acid sequences, it is unclear why the two enzymes have extinction coefficients, and metal contents, that vary so greatly.

Steady-state kinetic studies on as-isolated Bla2 containing 1 equivalent of Zn(II), using several different substrates, show that the as-isolated enzyme is catalytically-active (Table 1). Previously, Palzkill, *et al*, reported that recombinant Bla2 (Zn(II) content unknown) exhibited a K_m of 75 $\pm$ 5 μM and a k_{cat} 313 $\pm$ 21 s^{-1}, when using nitrocefin as substrate. [5] In our hands, recombinant Bla2 containing 1 eq of Zn(II) exhibited a K_m of 25 $\pm$ 4 μM and a k_{cat} of 41 $\pm$ 3 s^{-1} with nitrocefin as substrate. These values compare favorably with previous steady-state kinetic data on BcII, which exhibits a K_m of 9 μM and a k_{cat} of 43 s^{-1} with nitrocefin. [47] The stark difference in steady-state kinetic behavior of the two recombinant Bla2 preparations may be due to differing metal content and/or different assay conditions. Our assays were conducted at 25 C, while the preceding studies were conducted at 30 C, [5] although this should result in only a 1.25-fold difference in k_{cat}.

Our initial efforts to use the identical conditions (50 mM Hepes, pH 7.5, 50 μM Zn(II) and 20 μg of bovine serum albumin (BSA)) gave irreproducible results, which we attribute to enzyme instability under these conditions. The predicted pI of Bla2 is 7.6; therefore at pH 7.5, the enzyme would be expected to be predominantly zwitterionic and insoluble. We therefore lowered the pH of our assay buffer to 6.5, and the kinetic assays were much more reproducible. At present we cannot rule out any differences in the

enzymes that may have been introduced in the modified purification protocol. Clearly, the enzymes are different, as Palzkill, *et al*, reported that their recombinant Bla2 does not hydrolyze imipenem, [5] while our recombinant Bla2 exhibits a K_m of 89 μM and a k_{cat} of 92 s^{-1} when using imipenem as substrate (Table 1). However, at present, the source of these differences is unclear.

Metal Binding. Steady-state kinetic studies revealed that Bla2 containing 1 equivalent of Co(II) is less than ½ as catalytically active as CoCo-Bla2 (Table 2), suggesting that (*i*) Co(II) binding to Bla2 is random and that both metal ions bind with similar K_D values or (*ii*) that Bla2 exhibits positive cooperative binding of Co(II). A distributed binding model is supported by optical studies, which show both the *d-d* bands (Zn_1) and the S_{cys}→Co(II) LMCT (Zn_2), even at a loading of only 0.5 eq of Co(II), whose intensity maximizes above 2 eq of Co(II) per protein (Fig. 3). The EPR spectra of 1Co- and CoCo-Bla2 are nearly superimposable, and suggest 5- or 6-coordination for both, with at least one solvent ligand (Fig. 4). The ^{1}H NMR spectra of 1Co- and CoCo-Bla2 are nearly identical, showing the same five paramagnetically-shifted resonances (Fig. S8). Four of these resonances are solvent exchangeable (Fig. 5), indicating a total of four coordinated histidines with only 1 eq of Co(II) added. The Co K-edge EXAFS are also consistent with a distributed binding model, with only an apparent decrease in disorder accompanying addition of the second eq of Co(II). In sum, the spectroscopic studies of Co(II)-binding by Bla2 overwhelmingly indicate distributed binding of Co(II) by Bla2, but cannot distinguish between random and cooperative mechanisms in the resting enzyme.

In contrast to Co(II), the binding of Zn(II) by Bla2 appears to be sequential. EXAFS of 1Zn-Bla2 show the first eq of Zn(II) clearly binds to the Zn_1 site. Addition of a 2nd eq of Zn(II) to form ZnZn-Bla2 leads to the observation of a Zn-S interaction, consistent with Cys221 coordination (and metal bound at the Zn_2 site), and a clear Zn-Zn interaction at ~ 3.4 Å. The EXAFS are consistent with the steady-state kinetics, which showed that ZnZn-Bla2 is *not* twice as active as 1Zn-Bla2, suggesting that the second Zn(II) ion does not greatly affect catalysis and that the first site of Zn(II) binding, Zn_1 in this case, is more important kinetically. [15, 44, 51] To our knowledge this is the first documented example of a naturally occurring Zn enzyme that follows distinct metal binding pathways, dependent on whether the metal is Zn(II) or Co(II), and strongly underscores the need to demonstrate transferability when studying Co(II)-substituted Zn(II) enzymes.

The stopped-flow kinetics studies are consistent with the difference in metal binding mechanisms, and they offer the only information regarding the two possibilities for Co(II)-binding (random or cooperative). 1Zn-Bla2 does not stabilize the nitrocefin-derived reaction intermediate. The lack of an intermediate suggests that the situation described for resting 1Zn-Bla2 by EXAFS, a homogeneous population of mono-Zn enzyme, with Zn(II) bound in the canonical Zn_1 site, is preserved during turnover. In contrast, the appearance of an intermediate is clear in 1Co-Bla2 catalyzed nitrocefin hydrolysis. Within the accuracy of ε_{665} for the intermediate, the limiting concentration of the Co-bound intermediate (ca. 12 μM) suggests that, under turnover conditions, 1Co-Bla2 may, in fact, contain nearly equal populations of apo- and CoCo-Bla2, though at the current level of the data we can only speculate.

Comparison with CcrA. The metal-binding properties of two other B1 MβLs have been studied in detail. A set of enzymological, optical, X-ray absorption and magnetic resonance studies of Co(II) binding, similar to those presented here, by the B1 MβL CcrA indicated sequential binding, with the first equivalent of Co(II) bound exclusively at the Zn_1 site. To reach that conclusion, the combined spectroscopic approach was essential. For example, the EPR spectra of 1Co-CcrA and CoCo-CcrA were distinct but not definitive, both signals suggestive of 5/6-coordination. The XAS also indicated 5/6-coordination, higher, on average, than the corresponding Zn (*vide infra*). Neither XAS nor EPR showed evidence of a covalent bridge between the Co ions.

The EPR studies presented here also suggest 5/6-coordination for both Co(II) ions in Bla2, with little or no evidence of a bridging interaction. However, the XAS-derived average first shell bond lengths for 1Co- and 1Zn-Bla2 differ by only 0.02 Å, while those of 1Co- [32] and 1Zn-CcrA differ by 0.12 Å. A similar trend is apparent comparing the di-Co and di-Zn enzymes. The average first shell bond lengths for CoCo- and ZnZn-Bla2 differ by only 0.01 Å, while those of CoCo- [32] and ZnZn-CcrA differ by 0.12 Å. These data clearly indicate that Co(II)-substitution better preserves the coordination number of the native Zn(II) in Bla2 than it does in CcrA, which clearly indicates an increase in coordination number for both metal ions.

For Co(II)-substituted CcrA, the S→Co charge transfer band was difficult to assess, at any metal/protein ratio, and the XAS showed no statistically significant Co-S scattering. Ultimately, it was observation of the β-CH_2 protons of Cys221 by NMR (at 208 ppm), only in CoCo-CcrA, that offered a clear indication that the Zn_2 site is not populated until the Zn_1 site is filled. Unlike CcrA, the S→Co LMCT band was easily

detected for Bla2, at all metal/protein ratios, and the Co-S scattering was prominent at both 1 and 2 eq of Co(II). In this case we failed to detect the β-CH_2 resonance by NMR. We also note that the EXAFS-derived Zn-S distance is 0.06 Å longer in CcrA than in Bla2, which may indicate that Cys221 is a weaker donor in CcrA. This unexpected correlation is the subject of continuing investigation.

Comparison with BcII. The B1 MβL BcII is the most extensively studied of all MβLs. The initial crystal structure of BcII showed a mononuclear enzyme, with Zn(II) binding in the consensus Zn_1 site. [52] Subsequent structures showed that BcII contains a dinuclear Zn(II) binding site. [15, 53] The conflicting crystallographic data suggested the Zn(II) binding affinities at the Zn_1 (3H) and Zn_2 (DCH) sites in BcII might be different. Subsequently, di-Co(II) and mixed-metal (ZnCo) derivatives were reported and characterized spectroscopically, establishing a clear hierarchy of metal affinities at pH 6.0 that was less pronounced at physiological pH. [54] Both sites have been shown to be important for efficient β-lactam hydrolysis. [18, 55] More recent studies have shown that BcII shows a very modest preference for binding Co(II) at the Zn_1 site, but evidence of a di-Co(II) population is apparent at very low (~ 0.6 eq) Co(II) stoichiometries. [15] The present studies on Bla2 are not inconsistent with this model, though they offer no direct evidence as to the speciation of resting 1Co-Bla2.

Freeze quench spectroscopic studies of di-Co(II) BcII show a direct interaction of the substrate with both metal ions during catalysis, and indicate the presence of a covalent bridge in the resting enzyme, based on the observation of a parallel mode EPR signal. [56] The presence of the bridge appears, at present, unique to di-Co BcII, as in both CcrA and Bla2, we see no concrete evidence for Co-Co interactions in the Co K-

edge XAS or significant magnetic coupling in their EPR. [32] NMR studies of BcII also show that the β-CH_2 resonance shifts slightly downfield with increasing Co(II) loading, consistent with a small amount of magnetic coupling between the two metal ions. [15] While the β-CH_2 resonance was not observed for Bla2, no effects of Co(II) stoichiometry are apparent in the NMR spectra.

Significantly less data is available with respect to Zn(II) binding. The distributed binding of Co(II) by BcII is consistent with an earlier EXAFS study of Zn(II)-binding by the same enzyme. [44] Using optical competition and fluorescence spectroscopy, de Seny, *et al* showed that BcII exhibits negative cooperative Zn(II) binding and indicated that there are not high and low affinity Zn(II) binding sites. [44] They further contended that the first equivalent of Zn(II) distributes between the two sites and hinted that the binding of substrate may lead to Zn(II) preferentially binding the Zn_2 site in the active enzyme, [44] consistent with recent studies on BcII using substoichiometric Co(II). [57] In contrast, both CcrA and Bla2 have been shown here to bind Zn(II) sequentially. To the greater issue of Co(II)-substitution, it appears at present that the substitution is completely faithful in BcII; it reproduces the order of addition in CcrA, but not coordination number, without the formation of a bridged cluster; and it fails for Bla2 where distinct metal-dependent mechanisms are observed.

It has been recently shown that the more active mono-Co(II) form of BcII binds metal at the Zn_2 site. [57] The present studies on Bla2 are not inconsistent with this picture, although the rapid kinetics of 1Co-Bla2 with nitrocefin (Fig. 9) appear more consistent with a cooperative binding model for Co(II), at least in the presence of substrate. Page and coworkers have argued, using pH-dependent kinetics of Co(II)-

substituted BcII, that Co(II)-binding is cooperative in the presence of substrate, and that the dinuclear Co(II)-containing analog is the only catalytically-active form of the enzyme. [16, 58] The present studies on 1Co-Bla2, particularly the rapid kinetics in Fig. 9, lend some support for this model. More recent work suggests that a similar mechanism is operative in Zn(II)-BcII. [59] In contrast, Vila, [57] de Seny, [44] and Wommer [60] report that both the mono- and dinuclear Zn(II)-containing analogs of BcII are catalytically-active. Clearly, mono-Zn(II) Bla2 is active, and it shows no evidence of cooperativity. The related B1 MβL CcrA has been shown to be active as a both a mono-Zn(II) [61] and a mono-Co(II) enzyme, [37] and the B3 lactamases L1 [40] and GOB [12] have also been shown to be active as mono-Zn enzymes.

Analysis of the kinetic data demonstrates that 1Zn-Bla2 utilizes a rapid-equilibrium mechanism to hydrolyze nitrocefin, and the rate constants suggest that β-lactam C-N bond cleavage is rate-limiting. Vila and coworkers proposed the same rate-limiting step for BcII. [35] Previous studies on L1 and CcrA have shown that these enzymes utilize a similar rapid-equilibrium mechanism to hydrolyze nitrocefin, and a different mechanism to hydrolyze other substrates. [21, 62] Stopped-flow studies of 1Zn-Bla2 show that it behaves similarly, utilizing a distinct one-step mechanism in the hydrolysis of imipenem and cefaclor, without evidence of intermediate formation. Further conclusions cannot be reached without the availability of similar studies on ZnZn-Bla2.

Summary

Taken together, our data demonstrate that 1Zn-Bla2 is catalytically-active and EXAFS data on this analog demonstrate that Zn(II) binds in the consensus Zn_1 site. The

EXAFS data also show that Zn(II) binding is sequential, as in CcrA [32] and L1. [40] In contrast, all of the spectroscopic and kinetic data on Co(II)-containing Bla2 strongly indicate that Co(II) binding is either random or positive cooperative. A summary scheme showing how Zn(II) and Co(II) bind to Bla2 is shown in Figure 10. Further studies are required to address why Zn(II) and Co(II) behave differently in Bla2, and X-ray crystal structures of both analogs may yield information about the different metal binding properties. In particular, a crystal structure of Bla2 may shed light on why this enzyme appears to have different biochemical properties than BcII, in spite of the near identity of the two enzymes' primary structures. We believe this is the first documented example of a Zn enzyme binds Co(II) and Zn(II) via distinct mechanisms, underscoring the importance of validating transferability when extrapolating results on Co(II)-substituted proteins to the native Zn(II)-containing forms.

References

1. Mock, R.; Fouet, A., *Annu. Rev. Microbiol.* **2001,** 55, 647-671.
2. Inglesby, T. V.; Henderson, D. A.; Bartlett, J. G.; Ascher, M. S.; Eitzen, E.; Friedlander, A. M.; Hauer, J.; McDade, J.; Osterholm, M. T.; O'Toole, T.*, et al.*, *JAMA* **1999,** 281, 1735-1745.
3. Jernigan, J. A.; Stephens, D. S.; Ashford, D. A.; Omenaca, C.; Topiel, M. S.; Galbraith, M.; Tapper, M.; Fisk, T. L.; Zaki, S.; Popovic, T.*, et al.*, *Emerging Infect. Dis.* **2001,** 7, 933-944.
4. Meselson, M.; Guillemin, J.; Hugh-Jones, M.; Langmuir, A.; Popova, I.; Shelokov, A.; Yampolskaya, O., *Science* **1994,** 266, 1202-1208.
5. Materon, I. C.; Queenan, A. M.; Koehler, T. M.; Bush, K.; Palzkill, T., *Antimicro. Agents Chemo.* **2003,** 47, 2040-2042.
6. Neu, H. C., *Science* **1992,** 257, 1064-1073.
7. Rice, L. B.; Bonomo, R. A., *Drug Resist. Updates* **2000,** 3, 178-189.
8. Perez, F.; Endimiani, A.; Hujer, K. M.; Bonomo, R. A., *Current Opinion in Pharmacology* **2007,** 7, 459-469.
9. Walsh, C. T.; Wright, G. D., *Chem. Rev.* **2005,** 105, 391-393.
10. Crowder, M. W.; Spencer, J.; Vila, A. J., *Accounts of Chemical Research* **2006,** 39, 721-728.
11. Heinz, U.; Adolph, H. W., *CMLS, Cell. Mol. Life Sci.* **2004,** 61, 2827-2839.
12. Moran-Barrio, J.; Gonzalez, J. M.; Lisa, M. N.; Costello, A. L.; Peraro, M. D.; Carloni, P.; Bennett, B.; Tierney, D. L.; Limansky, A. S.; Viale, A. M.*, et al.*, *J. Biol. Chem.* **2007,** 282, 18286-18293.

13. Chen, Y.; Tenover, F. C.; Koehler, T. M., *Antimicro. Agents Chemo.* **2004,** 48, 4873-4877.

14. Felici, A.; Amicosante, G.; Oratore, A.; Strom, R.; Ledent, P.; Joris, B.; Fanuel, L.; Frere, J. M., *Biochemical Journal* **1993,** 291, 151-155.

15. Llarrull, L. I.; Tioni, M. F.; Kowalski, J.; Bennett, B.; Vila, A. J., *J. Biol. Chem.* **2007,** 282, 30586-30595.

16. Badarau, A.; Damblon, C.; Page, M. I., *Biochem. J.* **2007,** 401, 197-203.

17. Badarau, A.; Page, M. I., *Biochemistry* **2006,** 45, 10654-10666.

18. Gonzalez, J. M.; Medrano Martin, F. J.; Costello, A. L.; Tierney, D. L.; Vila, A. J., *J. Mol. Biol.* **2007,** 373, 1141-1156.

19. Crowder, M. W.; Walsh, T. R.; Banovic, L.; Pettit, M.; Spencer, J., *Antimicrobial Agents and Chemotherapy* **1998,** 42, 921-926.

20. McManus-Munoz, S.; Crowder, M. W., *Biochemistry* **1999,** 38, 1547-1553.

21. Spencer, J.; Clark, A. R.; Walsh, T. R., *J. Biol. Chem.* **2001,** 276, 33638-33644.

22. Sharma, N. P.; Hajdin, C.; Chandrasekar, S.; Bennett, B.; Yang, K. W.; Crowder, M. W., *Biochemistry* **2006,** 45, 10729-10738.

23. Matthews, M. L.; Periyannan, G.; Hajdin, C.; Sidgel, T. K.; Bennett, B.; Crowder, M. W., *Journal of the American Chemical Society* **2006,** 128, 13050-13051.

24. Kuzmic, P., *Analytical Biochemistry* **1996,** 237, 260-273.

25. Hanson, G. R.; Gates, K. E.; Noble, C. J.; Mitchell, A.; Benson, S.; Griffin, M.; Burrage, K., XSophe - Sophe - XeprViewA computer simulation software suite for the analysis of continuous wave EPR spectra. In *EPR of Free Radicals in Solids:*

Trends in Methods and Applications, Shiotani, M.; Lund, A., Eds. Kluwer Press: New York, 2003; pp 197-237.

26. Bennett, B.; Holz, R. C., *Biochemistry* **1997,** 36, 9837-9846.
27. Bennett, B., *Curr. Topics Biophys.* **2002,** 26, 49-57.
28. Thomas, P. W.; Stone, E. M.; Costello, A.; Tierney, D. L.; Fast, W., *Biochemistry* **2005,** 44, 7559-7569.
29. Sixpack is available free of charge from its author at http://www-ssrl.slac.stanford.edu/~swebb/sixpack.htm.
30. IFEFFIT is open source software available from http://cars9.uchicago.edu/ifeffit.
31. Ankudinov, A. L.; Ravel, B.; Rehr, J. J.; Conradson, S. D., *Physical Review B* **1998,** 58, 7565-7576.
32. Periyannan, G.; Costello, A. L.; Tierney, D. L.; Yang, K. W.; Bennett, B.; Crowder, M. W., *Biochemistry* **2006,** 45, 1313-1320.
33. Outten, C. E.; O'Halloran, T. V., *Science* **2001,** 292, 2488-2492.
34. Wang, Z.; Fast, W.; Benkovic, S. J., *Journal of the American Chemical Society* **1998,** 120, 10788.
35. Rasia, R. M.; Vila, A. J., *ARKIVOC* **2003,** 3, 507-516.
36. Segel, I. H., *Enzyme Kinetics*. John Wiley and Sons, Inc.: New York, 1993; p 955.
37. Wang, Z.; Benkovic, S. J., *Journal of Biological Chemistry* **1998,** 273, 22402-22408.
38. Fabiane, S. M.; Sohi, M. K.; Wan, T.; Payne, D. J.; Bateson, J. H.; Mitchell, T.; Sutton, B. J., *Biochemistry* **1998,** 37, 12404-12411.
39. Garcia-Saez, I.; Docquier, J.-D.; Rossolini, G. M.; Dideberg, O., *Journal of Molecular Biology* **2008,** 375, 604-611.

40. Costello, A.; Periyannan, G.; Yang, K. W.; Crowder, M. W.; Tierney, D. L., *J. Biol. Inorg. Chem.* **2006,** 11, 351-358.

41. Concha, N. O.; Rasmussen, B. A.; Bush, K.; Herzberg, O., *Structure* **1996,** 4, 823-836.

42. Ullah, J. H.; Walsh, T. R.; Taylor, I. A.; Emery, D. C.; Verma, C. S.; Gamblin, S. J.; Spencer, J., *J. Mol. Biol.* **1998,** 284, 125-136.

43. Concha, N. O.; Janson, C. A.; Rowling, P.; Pearson, S.; Cheever, C. A.; Clarke, B. P.; Lewis, C.; Galleni, M.; Frere, J. M.; Payne, D. J.*, et al.*, *Biochemistry* **2000,** 39, 4288-4298.

44. de Seny, D.; Heinz, U.; Wommer, S.; Kiefer, M.; Meyer-Klaucke, W.; Galleni, M.; Frere, J. M.; Bauer, R.; Adolph, H. W., *Journal of Biological Chemistry* **2001,** 276, 45065-45078.

45. A reexamination of the Co K-edge XAS of CoCo-CcrA, in light of the present discussion, gave results identical to those presented in Reference 32.

46. Hu, Z.; Periyannan, G.; Bennett, B.; Crowder, M. W., *J. Am. Chem. Soc.* **2008,** 130, 14207-14216.

47. de Seny, D.; Prosperi-Meys, C.; Bebrone, C.; Rossolini, G. M.; Page, M. I.; Noel, P.; Frere, J. M.; Galleni, M., *Biochemical Journal* **2002,** 363, 687-696.

48. Yang, Y.; Keeney, D.; Tang, X. J.; Canfield, N.; Rasmussen, B. A., *Journal of Biological Chemistry* **1999,** 274, 15706-15711.

49. Yanchak, M. P.; Taylor, R. A.; Crowder, M. W., *Biochemistry* **2000,** 39, 11330-11339.

50. Paul-Soto, R.; Zeppezauer, M.; Adolph, H. W.; Galleni, M.; Frere, J. M.; Carfi, A.; Dideberg, O.; Wouters, J.; Hemmingsen, L.; Bauer, R., *Biochemistry* **1999,** 38, 16500-16506.

51. Rasia, R. M.; Vila, A. J., *Biochemistry* **2002,** 41, 1853-1860.

52. Carfi, A.; Pares, S.; Duee, E.; Galleni, M.; Duez, C.; Frere, J. M.; Dideberg, O., *EMBO Journal* **1995,** 14, 4914-4921.

53. Carfi, A.; Duee, E.; Galleni, M.; Frere, J. M.; Dideberg, O., *Acta Crystallographica Section D* **1998,** D54, 313-323.

54. Orellano, E. G.; Girardini, J. E.; Cricco, J. A.; Ceccarelli, E. A.; Vila, A. J., *Biochemistry* **1998,** 37, 10173-10180.

55. Abriata, L. A.; Gonzalez, L. J.; Llarrull, L. I.; Tomatis, P. E.; Myers, W. K.; Costello, A. L.; Tierney, D. L.; Vila, A. J., *Biochemistry* **2008,** 47, 8590-8599.

56. Tioni, M. F.; Llarrull, L. I.; Poeylaut-Palena, A. A.; Marti, M. A.; Saggu, M.; Periyannan, G. R.; Mata, E. G.; Bennett, B.; Murgida, D. H.; Vila, A. J., *J. Am. Chem. Soc.* **2008,** 130, 15852-15863.

57. Llarrull, L. I.; Tioni, M. F.; Vila, A. J., *J. Am. Chem. Soc.* **2008,** 130, 15842-15851.

58. Badarau, A.; Page, M. I., *Biochemistry* **2006,** 45, 11012-11020.

59. Badarau, A.; Page, M. I., *J. Biol. Inorg. Chem.* **2008,** 13, 919-928.

60. Wommer, S.; Rival, S.; Heinz, U.; Galleni, M.; Frere, J. M.; Franceschini, N.; Amicosante, G.; Rasmussen, B.; Bauer, R.; Adolph, H. W., *Journal of Biological Chemistry* **2002,** 277, 24142-24147.

61. Paul-Soto, R.; Hernandez-Valladares, M.; Galleni, M.; Bauer, R.; Zeppezauer, M.; Frere, J. M.; Adolph, H. W., *FEBS Letters* **1998,** 438, 137-140.

62. McManus-Munoz, S.; Crowder, M. W., *Biochemistry* **1999,** 38, 1547-1553.

Table 1: Steady-state kinetic parameters[a] for nitrocefin, imipenem, cefaclor, and meropenem hydrolysis by Bla2 containing 1 equivalent of Zn(II).

	Substrate: Nitrocefin	**Substrate: Imipenem**	**Substrate: Cefaclor**	**Substrate: Meropenem**
K_m (μM)	25 ± 4	89 ± 35	67 ± 6	110 ± 42
k_{cat} (s^{-1})	41 ± 3	92 ± 21	24 ± 1	49 ± 11

[a]Kinetic assays were conducted at 25 °C in 50 mM Hepes, pH 6.5.

Table 2: Steady-state kinetic parameters for Bla2 containing 1 or 2 equivalents of Zn(II) or Co(II).

	1Co(II)-Bla2	**2Co(II)-Bla2**	**1Zn(II)-Bla2**	**2Zn(II)-Bla2**
K_m(μM)	18 ± 2	30 ± 9	28 ± 4	35 ± 4
k_{cat} (s^{-1})	19 ± 1	47 ± 5	32 ± 2	42 ± 2

All experiments were conducted at 25 °C in 50 mM Hepes, pH 6.5. The Bla2 analogs were prepared by adding the indicated equivalents of metal to apo-Bla2 before the assays were conducted.

Table 3: Kinetic constants used in KINSIM simulations, using the mechanism in Scheme 1.[a]

constant	value used in simulation for nitrocefin	value used in simulation for imipenem	value used in simulation for cefaclor
K_1	0.12 ± 0.01	0.13 ± 0.01	2.2 ± 0.1
k_2	10 ± 1	35 ± 1	15 ± 1
k_{-2}	4 ± 1	Set to 0	Set to 0
k_3	40 ± 1	-	-
k_{-3}	Set to 0	-	-

[a] ProK software (nonlinear Marquardt-Levenberg algorithm) was used to determine the error in the rate constants.

Table 4. Best fits to Co- and Zn-Bla2 and Zn-CcrA EXAFS. [a]

Fit	*Sample* & Model	M-N/O	M-S	M-His [b]	M-M
S1-5	*1Co-Bla2* 4 N/O (2 His) + 0.5 S	2.03 (6.9)	2.27 (1.8)	2.91 (4.6) 3.26 (11) 4.01 (5.8) 4.21 (13)	
S2-5	*CoCo-Bla2* 4 N/O (2 His) + 0.5 S	2.05 (3.6)	2.27 (3.5)	2.91 (3.6) 3.29 (18) 3.85 (10) 4.17 (17)	
S3-5	*1Zn-Bla2* 4 N/O (3 His)	2.03 (6.6)		2.91 (6.6) 3.16 (9.8) 4.11 (19) 4.42 (23)	
S4-6	*ZnZn-Bla2* 4 N/O (2 His) + 0.5 S + Zn-Zn	2.04 (6.3)	2.27 (2.6)	2.90 (7.1) 3.08 (5.8) 4.08 (18) 4.43 (25)	3.44 (15)
S5-4	*1Zn-CcrA* 4 N/O (3 His)	2.03 (6.9)		2.91 (6.6) 3.16 (9.8) 4.11 (19) 4.42 (23)	
S6-9	*ZnZn-CcrA* 4 N/O (2 His) + 0.5 S + Zn-Zn [c]	2.03 (5.9)	2.33 (4.5)	2.91 (6.8) 3.15 (3.5) 4.17 (22) 4.42 (18)	3.44 (11)

[a] Distances (Å) and disorder parameters (in parentheses, σ^2 (10^{-3} Å^2)) shown derive from integer or half-integer coordination number fits to filtered EXAFS data. For detailed fitting results, including ranges in both *k*- and R-space, fit residuals and fits to unfiltered data, see Figures S1-S6 and Tables S1-S6 in Supporting Information.

[b] Multiple scattering paths represent combined paths, as described previously (see Materials and Methods).

[c] This fit includes a Zn-C scattering path (0.5 C/Zn) at a distance of 2.49 Å (σ^2 = 1.4 x 10^{-3} Å^2).

Scheme 1

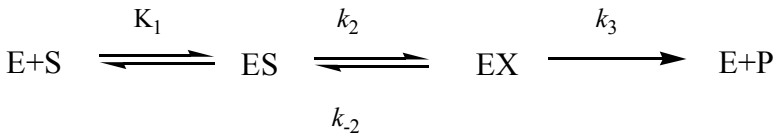

Scheme 2

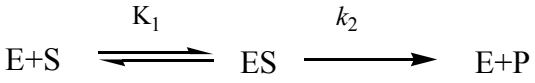

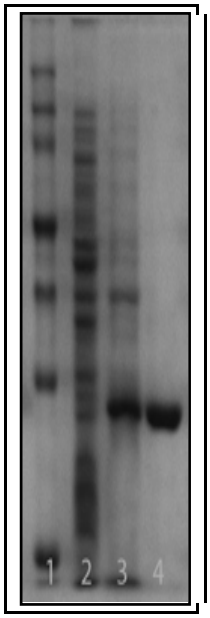

Figure 1. SDS-PAGE gel of purification of recombinant Bla2. Lane 1: molecular weight markers (from top to bottom: 150 kDa, 100 kDa, 75 kDa, 50 kDa, 35 kDa, 25 kDa, and 15 kDa); lane 2: boiled cell fraction of cells before induction with IPTG; lane 3: soluble fraction after French pressing and dialysis against 50 mM Hepes, pH 6.5; Lane 4: purified Bla2 after SP-Sepharose chromatography.

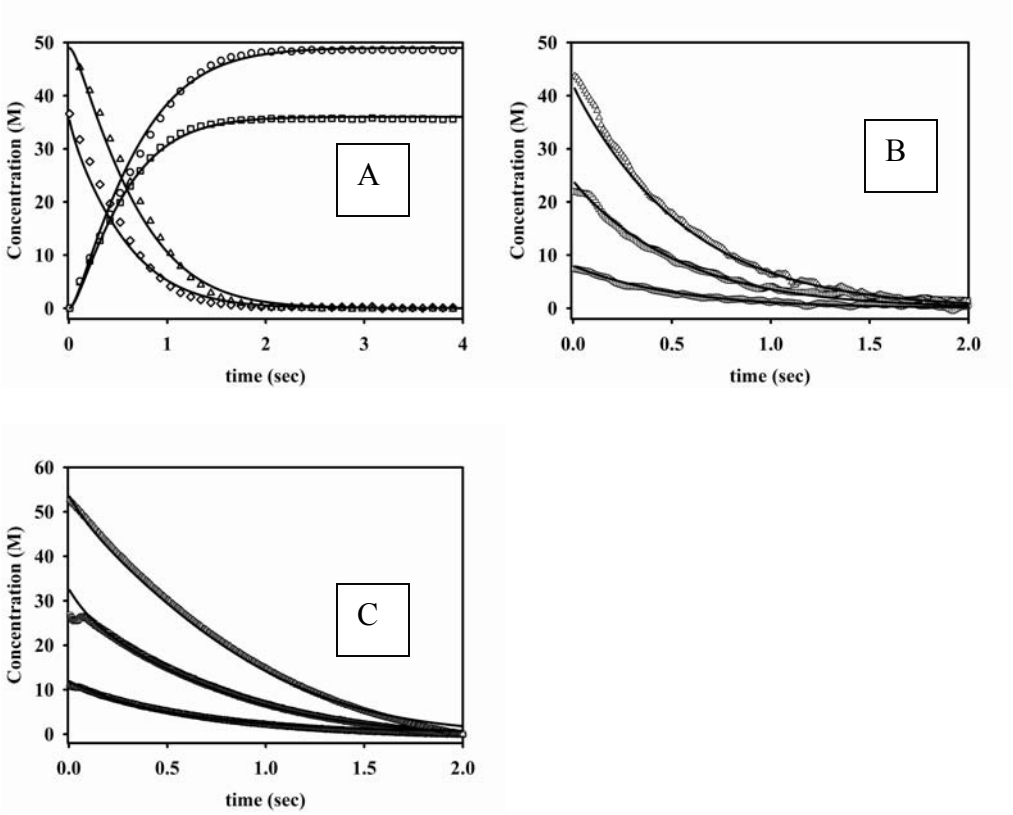

Figure 2. Progress curves for the reaction of 1Zn-Bla2 with nitrocefin (A), imipenem (B) and cefaclor (C). (A) The concentration of product increased over time using 25 (□) and 50 (○) μM nitrocefin, while substrate concentrations decreased over time using 25 (◊) and 50 (Δ) μM nitrocefin. The solid progress curves were generated by KINSIM, using the mechanism in Scheme 1 and the kinetic constants in Table 3. (B) Progress curves of the reaction of imipenem and Bla2 containing 1 eq. Zn(II) at 4 ^{o}C. The concentrations of substrate were (Δ) 50 μM, (□) 25 μM, and (○) 10 μM, and the concentration of Bla2 was 20 μM. The solid lines were generated by using KINSIM, the mechanism in Scheme 2, and the kinetic constants in Table 3. (C) Progress curves of the reaction of cefaclor and Bla2 containing 1 eq. Zn(II) at 4 ^{o}C. The concentrations of substrate were (Δ) 50 μM, (□) 25 μM, and (○) 10 μM, and the concentration of Bla2 was 20 μM. The solid lines were generated by using KINSIM, the mechanism in Scheme 2, and the kinetic constants in Table 3.

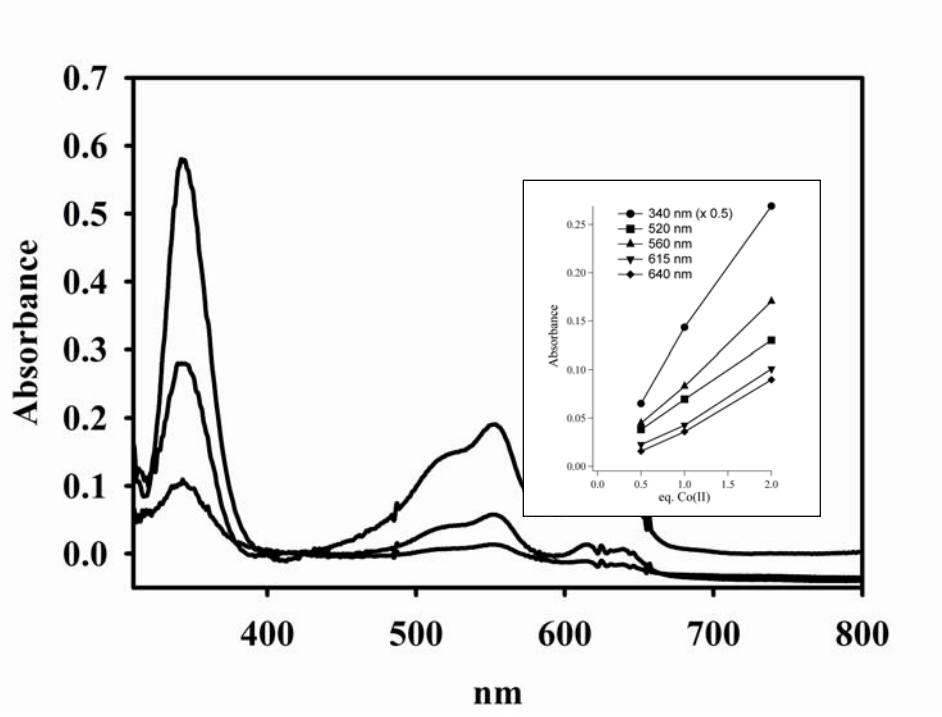

Figure 3. Optical titration of apo-Bla2 with Co(II). The concentration of apo-Bla2 was 1.2 mM apo-Bla2, and the buffer was 15 mM Hepes, pH 6.5, containing 100 mM NaCl. The enzyme was titrated with 0.5, 1.0, and 2.0 equivalents of Co(II) (bottom to top at 550 nm). Inset: Absorbance changes as the equivalents of Co(II) increase.

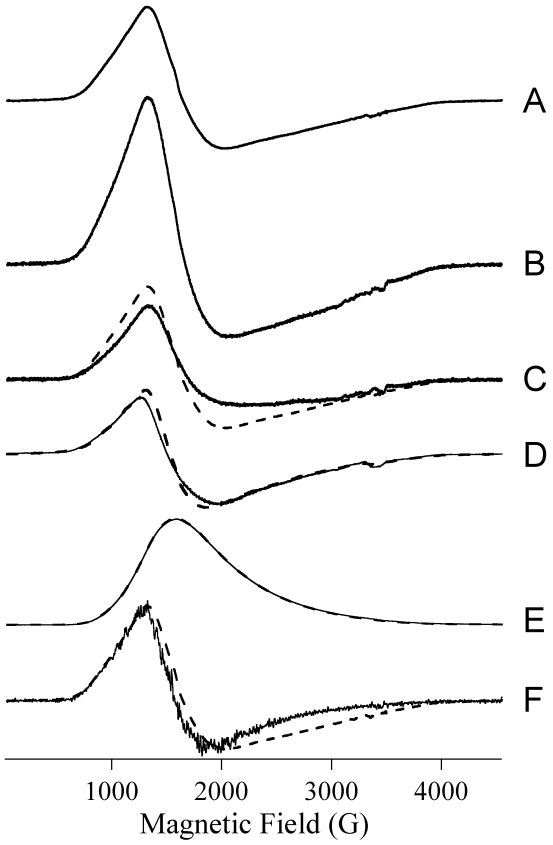

Figure 4. EPR spectra from Co(II)-containing Bla2. (A) 1Co-Bla2, 2 mW, 11 K; (B) CoCo-Bla2, 2 mW, 11 K; (C, solid line) = (B) – (A); (C, dashed line) 1Co-Bla2, 2 mW, 11 K; (D, solid line) CoCo-Bla2 × 0.5, 50 mW, 7 K; (D, dashed line) 1Co-Bla2, 50 mW, 7 K; (E, solid line) CoCo-Bla2 × 0.5, 100 mW, 7 K, rapid passage; (E, dashed line) 1Co-Bla2, 100 mW, 7 K, rapid passage; (F, solid line) derivative of rapid passage spectrum of CoCo-Bla2; (F, dashed line) 1Co-Bla2, 2 mW, 11 K. Rapid passage spectra were recorded using second-derivative quadrature phase-sensitive detection. The intensities of spectra shown in A – C are correct relative to each other. Intensities of pairs of spectra in D – F are arbitrary, but within each pair the intensities are correct when the multiplication factors given are taken into account.

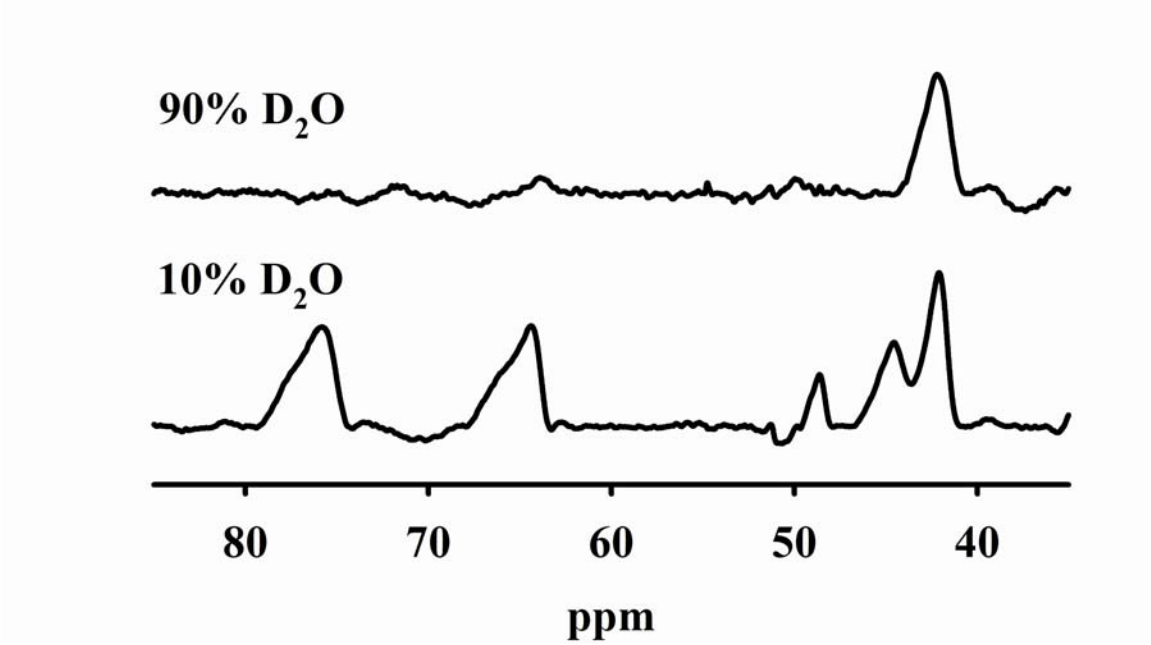

Figure 5. 500 MHz ^{1}H NMR spectra of CoCo-Bla2 in 10% D_2O and 90% D_2O.

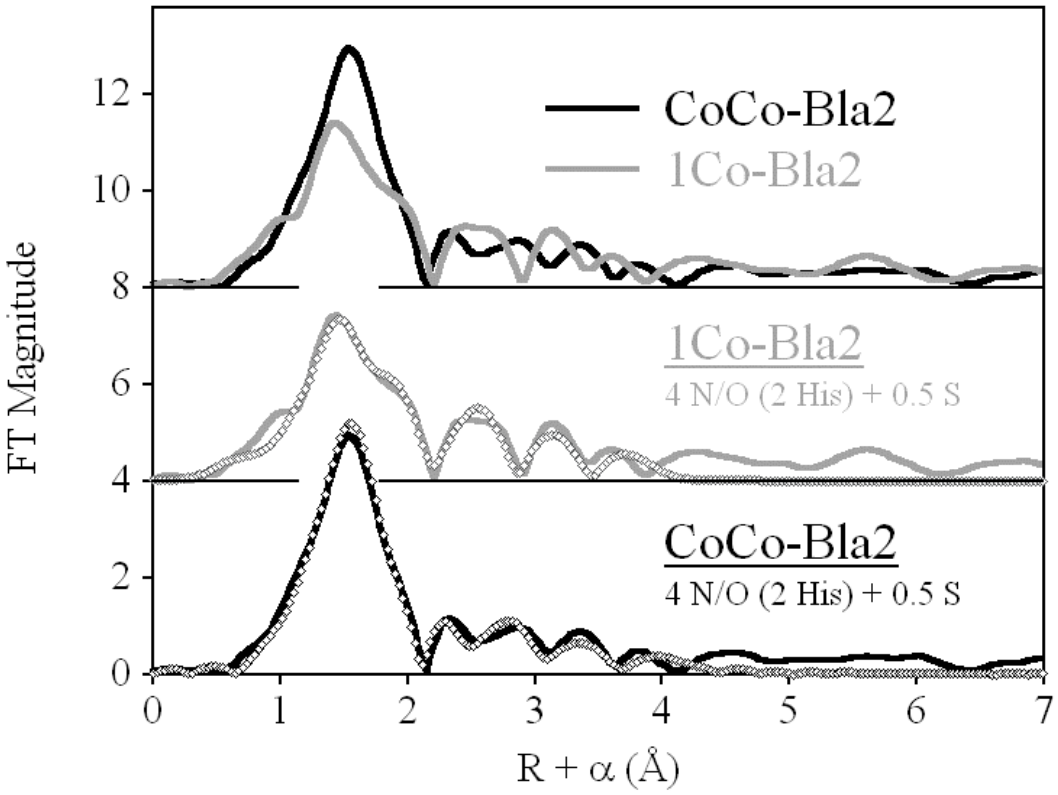

Figure 6. Fourier transformed EXAFS spectra of Co(II)-substituted Bla2. (Top) Direct comparison of 1Co- (gray line) and CoCo-Bla2 (black line). (Center) Best fit (open symbols) for 1Co-Bla2. (Bottom) Best fit (open symbols) for CoCo-Bla2. See Table 4 and Supporting Information for fit details.

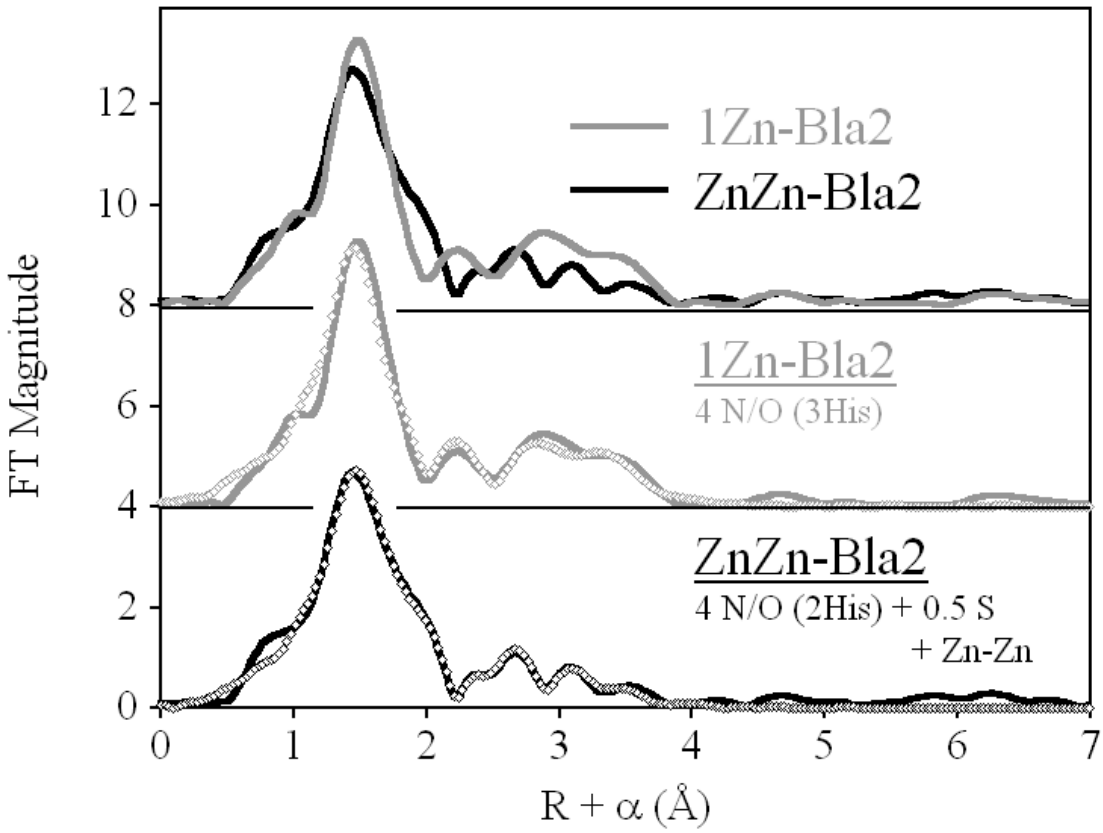

Figure 7. Fourier transformed EXAFS spectra of Zn(II)-Bla2. (Top) Direct comparison of 1Zn- (gray line) and ZnZn-Bla2 (black line). (Center) Best fit (open symbols) for 1Zn-Bla2. (Bottom) Best fit (open symbols) for ZnZn-Bla2. See Table 4 and Supporting Information for fit details.

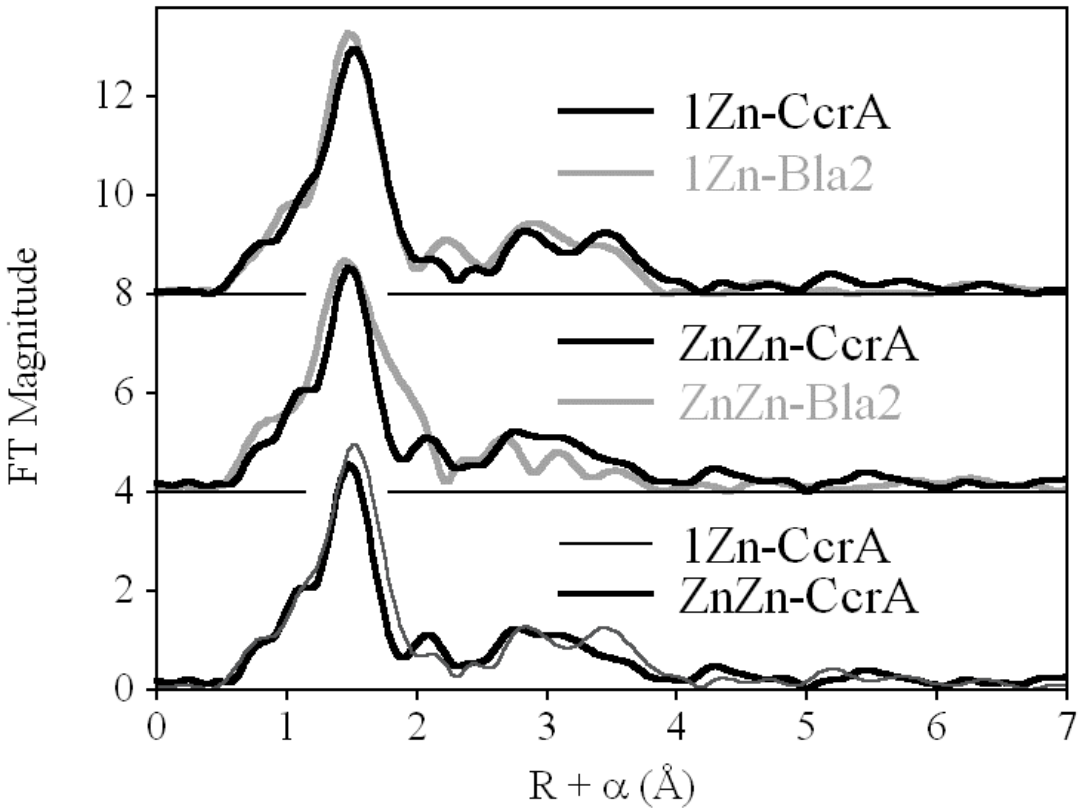

Figure 8. EXAFS Fourier transforms for Zn-CcrA. (Top) Direct comparison of 1Zn-CcrA (black line) and 1Zn-Bla2 (gray line). (Center) Direct comparison of ZnZn-CcrA (black line) and ZnZn-Bla2 (gray line). (Bottom) Direct comparison of 1Zn-CcrA (thin black line) and ZnZn-CcrA (thick black line).

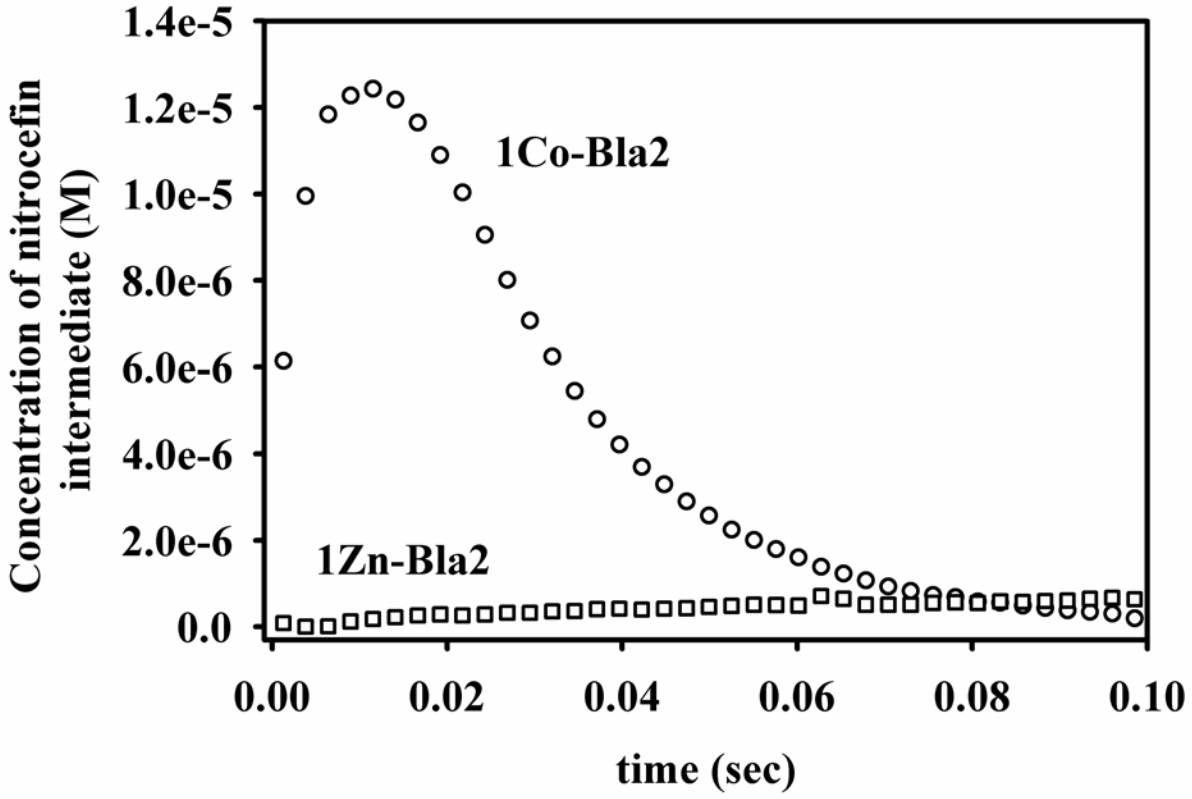

Figure 9: Stopped-flow kinetic traces for the hydrolysis of nitrocefin by 1Co- and 1Zn-Bla2, monitored at 665 nm.

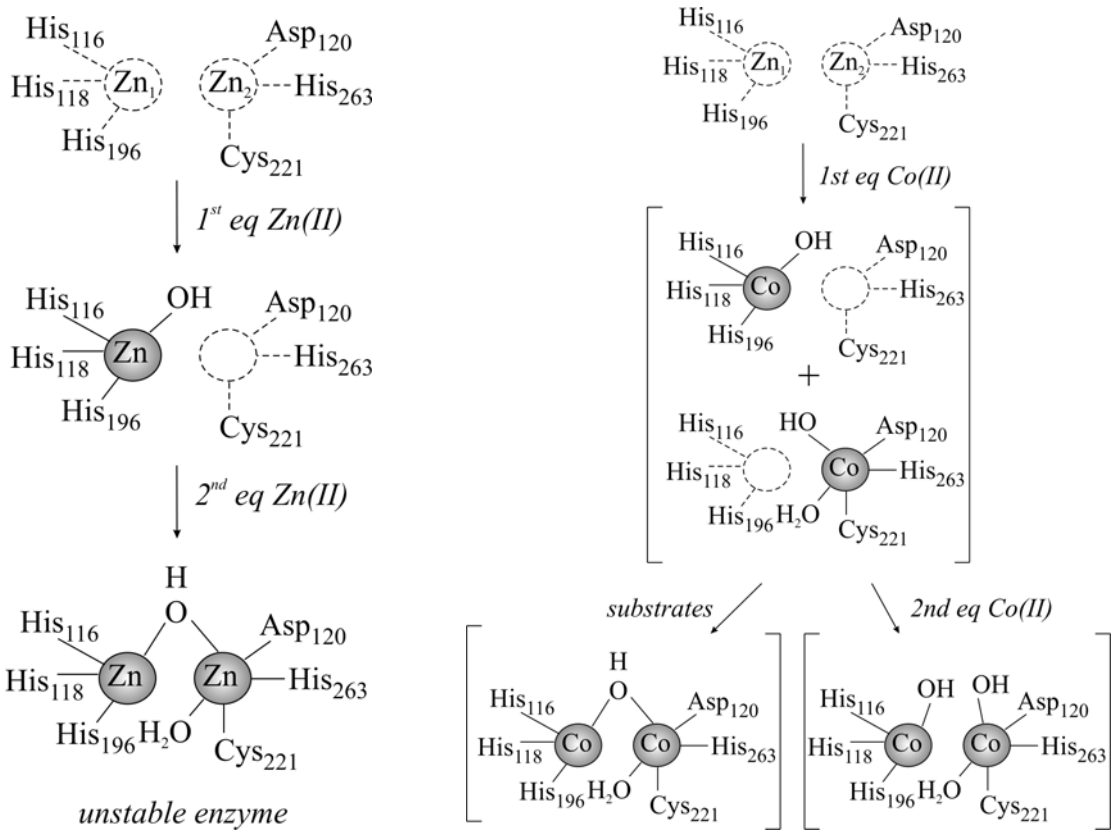

Figure 10: The proposed active site of Bla2 after the addition of 1 or 2 equivalents of Zn(II) (left) or Co(II) (right) to apo-Bla2.

XAS of Zn- and Co-containing Bla2

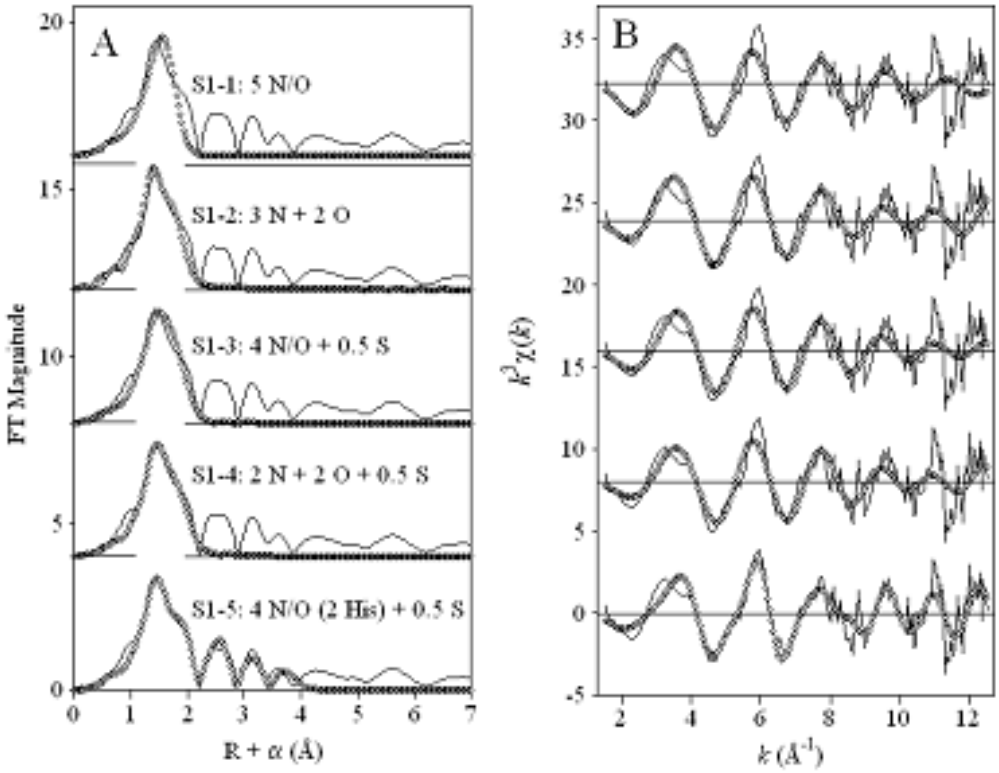

Figure S3. Fourier transforms (A) of k3-weighted EXAFS (B) for 1Co-Bla2 (solid lines),and corresponding curve fits (open symbols) from Table S1, numbers correspond to entries in the associated Table.

Table S1. Detailed EXAFS curve fitting results for 1Co-Bla2.[a]

Fit	Model	*Co–N/O*	*Co–S*	*Co–His*[b]	*Co–Co*	R_f[c]	R_u[c]
S1–1	5 N/O	2.04 (9.0)				183	428
S1–2	3 N + 2 O	[N] 2.10 (1.0) [O] 1.95 (6.0)				67	353
S1–3	4 N/O + 0.5 S	2.04 (9.0)	2.27 (1.8)			54	355
S1–4	2 N + 2 O + 0.5 S	[N] 2.04 (1.1) [O] 1.90 (5.8)	2.27 (3.8)			31	329
S1–5	4 N/O (2His) + 0.5 S[d]	2.03 (6.9)	2.27 (2.8)	2.91 (4.6), 3.26 (11) 4.01 (5.8), 4.21 (13)		117	188
S1–6	4 N/O (2His) + 0.5 S + Co–Co[d]	2.03 (6.9)	2.27 (3.7)	2.91 (8.6), 3.25 (20) 4.02 (10), 4.21 (14)	3.55 (6.0)	108	168

[a] Distances (Å) and disorder parameters (in parentheses, σ^2 (10^{-3} Å^2)) shown derive from integer or half-integer coordination number fits to filtered EXAFS data [k = 1.5–12.5 Å^{-1}; R = 0.7–2.3 Å (fits 1–4) or 0.2–4.2 Å (fits 5–6)].

[b] Multiple scattering paths represent combined paths, as described previously (see Materials and Methods).

[c] Goodness of fit (R_f for fits to filtered data; R_u for fits to unfiltered data) defined as

$$1000 * \frac{\sum_{i=1}^{N}\left[\mathrm{Re}(\chi_{i_{exp}}) - \mathrm{Re}(\chi_{i_{sim}})\right]^2 + \left[\mathrm{Im}(\chi_{i_{exp}}) - \mathrm{Im}(\chi_{i_{sim}})\right]^2}{\sum_{i=1}^{N}\left[\mathrm{Re}(\chi_{i_{exp}})\right]^2 + \left[\mathrm{Im}(\chi_{i_{exp}})\right]^2}$$

, where N is the number of data points.

[d] Inclusion of a Co–C scattering path (0.5 C/Co), along with the parameters of this fit, led to a refined Co–C distance of 2.42 Å (σ^2 = 0.1 x 10^{-3} Å^2), with a modest decrease in fit residual to R_f = 102.

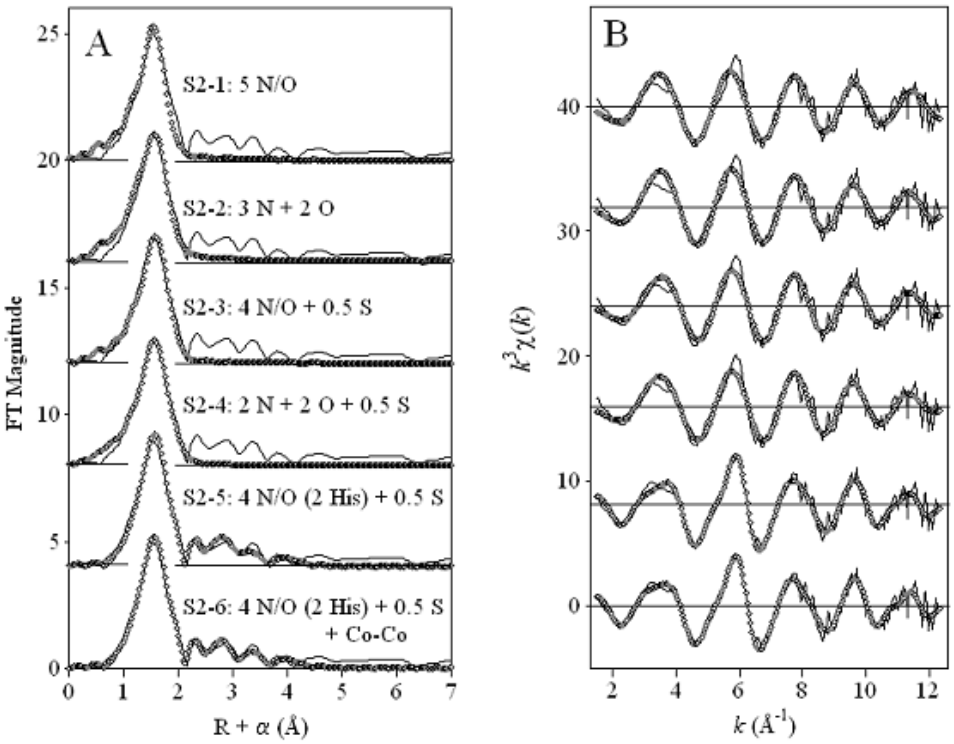

Figure S4. Fourier transforms (A) of k^3-weighted EXAFS (B) for CoCo-Bla2 (solid lines), and corresponding curve fits (open symbols) from Table S2.

Table S2. Detailed EXAFS curve fitting results for CoCo-Bla2.[a]

Fit	Model	*Co-N/O*	*Co-S*	*Co-His* [b]	*Co-Co*	R_f [c]	R_u [c]
S2-1	5 N/O	2.06 (4.2)				39	182
S2-2	3 N + 2 O	[N] 2.09 (1.5) [O] 1.96 (1.4)				20	168
S2-3	4 N/O + 0.5 S	2.05 (3.8)	2.27 (3.2)			12	160
S2-4	2 N + 2 O + 0.5 S	[N] 2.10 (6.0) [O] 1.99 (3.2)	2.27 (1.4)			11	155
S2-5	4 N/O (2His) + 0.5 S[d]	2.05 (3.6)	2.27 (3.5)	2.91 (3.6), 3.29 (18) 3.85 (10), 4.17 (17)		82	107
S2-6	4 N/O (2His) + 0.5 S + Co-Co	2.05 (3.3)	2.27 (3.4)	2.91 (3.7), 3.28 (21) 3.84 (11), 4.16 (19)	3.31 (13)	66	103

[a] Distances (Å) and disorder parameters (in parentheses, σ^2 (10^{-3} Å^2)) shown derive from integer or half-integer coordination number fits to filtered EXAFS data [k = 1.5-12.4 Å^{-1}; R = 0.7-2.3 Å (fits 1-4) or 0.2-4.2 Å (fits 5-6)].

[b] Multiple scattering paths represent combined paths, as described previously (see Materials and Methods).

[c] Goodness of fit (R_f for fits to filtered data; R_u for fits to unfiltered data) defined as

$$1000 * \frac{\sum_{i=1}^{N}\left\{\left[\mathrm{Re}(\chi_{i_{data}})-\mathrm{Re}(\chi_{i_{fit}})\right]^2+\left[\mathrm{Im}(\chi_{i_{data}})-\mathrm{Im}(\chi_{i_{fit}})\right]^2\right\}}{\sum_{i=1}^{N}\left\{\left[\mathrm{Re}(\chi_{i_{data}})\right]^2+\left[\mathrm{Im}(\chi_{i_{data}})\right]^2\right\}},$$ where N is the number of data points.

[d] Addition of a Co-C scattering path (0.5 C/Co) to the parameters of this fit led to a refined Co-C distance of 2.43 Å (σ^2 = 0.1 x 10^{-3} Å^2), with a minimal decrease in fit residual to R_f = 78.

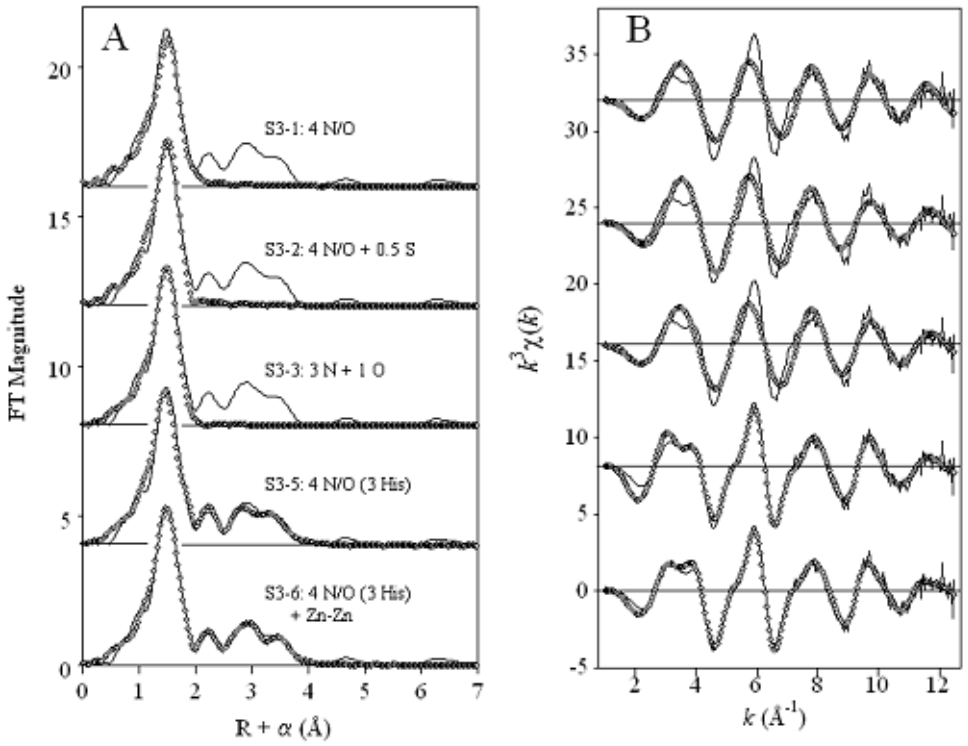

Figure S5. Fourier transforms (A) of k^3-weighted EXAFS (B) for 1Zn-Bla2 (solid lines), and corresponding curve fits (open symbols) from Table S3.

Table S3. Detailed EXAFS curve fitting results for 1Zn-Bla2.[a]

Fit	Model	Zn•N/O	Zn•S	Zn•His [b]	Zn•Zn	R_f [c]	R_u [c]
S3•1	4 N/O	2.02 (4.8)				56	200
S3•2	4 N/O + 0.5 S	2.01 (5.0)	2.23 (15)			40	191
S3•3	3 N + 1 O	[N] 2.06 (3.1) [O] 1.93 (1.1)				43	192
S3•4	2 N + 2 N	[N_1] 2.08 (0.5) [N_2] 1.96 (0.1)				46	192
S3•5	4 N/O (3 His)[d]	2.03 (6.6)		2.91 (6.6), 3.16 (9.8) 4.11 (19), 4.42 (23)		40	52
S3•6	4 N/O (3 His) + Zn•Zn	2.03 (6.6)		2.92 (8.6), 3.19 (32) 4.15 (14), 4.39 (20)	3.36 (10)	33	46

[a] Distances (Å) and disorder parameters (in parentheses, σ^2 (10^{-3} Å^2)) shown derive from integer or half-integer coordination number fits to filtered EXAFS data [k = 1.5-12.5 Å^{-1}; R = 0.7-2.2 Å (fits 1-4) or 0.2-4.2 Å (fits 5-6)].

[b] Multiple scattering paths represent combined paths, as described previously (see Materials and Methods).

[c] Goodness of fit (R_f for fits to filtered data; R_u for fits to unfiltered data) defined as

$$1000 * \frac{\sum_{i=1}^{N}\left[\mathrm{Re}(\chi_{f\_exp})_i - \mathrm{Re}(\chi_{f\_calc})_i\right]^2 + \left[\mathrm{Im}(\chi_{f\_exp})_i - \mathrm{Im}(\chi_{f\_calc})_i\right]^2}{\sum_{i=1}^{N}\left[\mathrm{Re}(\chi_{f\_exp})_i\right]^2 + \left[\mathrm{Im}(\chi_{f\_exp})_i\right]^2}$$

, where N is the number of data points.

[d] Inclusion of a Zn•C scattering path (0.5 C/Zn), along with the parameters of this fit, led to a refined Zn•C distance of 2.55 Å (σ^2 = 5.3 x 10^{-3} Å^2), with a modest decrease in fit residual to R_f = 36.

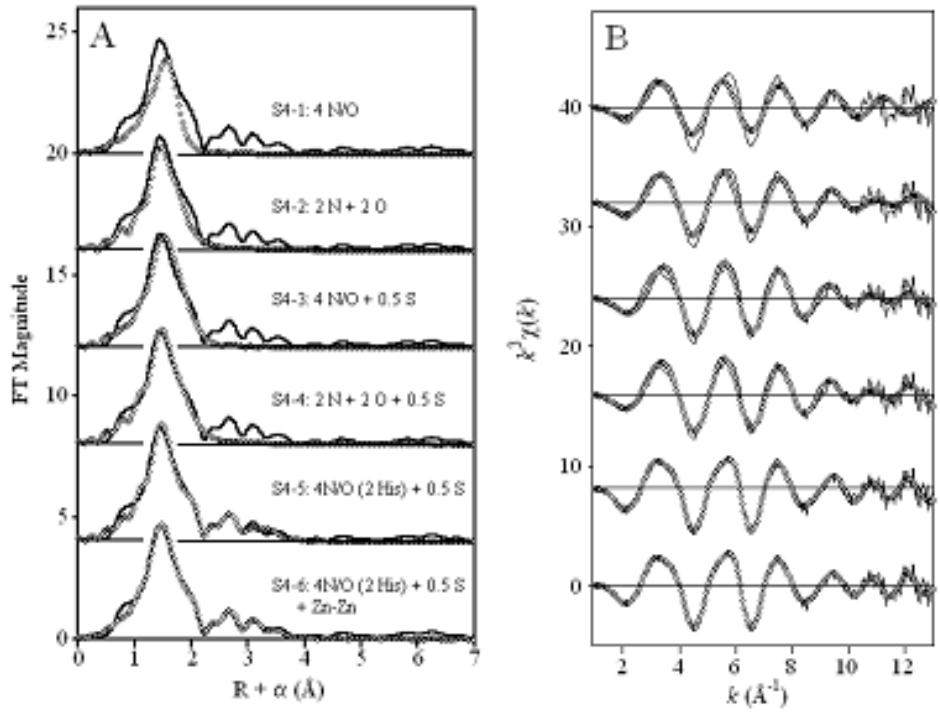

Figure S6. Fourier transforms (A) of k^3-weighted EXAFS (B) for ZnZn-Bla2 (solid lines), and corresponding curve fits (open symbols) from Table S4.

Table S4. Detailed EXAFS curve fitting results for ZnZn-Bla2.[a]

Fit	Model	*Zn•N/O*	*Zn•S*	*Zn•His* [b]	*Zn•Zn*	R_f [c]	R_u [c]
S4•1	4 N/O	2.07 (6.5)				186	230
S4•2	2 N + 2 O	[N] 2.13 (0.1) [O] 1.98 (1.7)				55	127
S4•3	4 N/O + 0.5 S	2.04 (6.4)	2.27 (14)			22	191
S4•4	2 N + 2 O + 0.5 S	[N] 2.14 (6.5) [O] 1.97 (2.9)	2.27 (2.6)			13	96
S4•5	4 N/O (2His) + 0.5 S [d]	2.04 (6.5)	2.27 (2.6)	2.90 (7.6), 3.10 (3.8) 4.09 (17), 4.43 (25)		21	56
S4•6	4 N/O (2His) + 0.5 S + Zn•Zn [e]	2.04 (6.3)	2.27 (2.6)	2.90 (7.1), 3.08 (5.8) 4.08 (18), 4.43 (25)	3.44 (15)	9	36

[a] Distances (Å) and disorder parameters (in parentheses, σ^2 (10^{-3} Å^2)) shown derive from integer or half•integer coordination number fits to filtered EXAFS data [k = 1•13 Å^{-1}; R = 0.7•2.3 Å (Fits 1•4) or 0.2•4.2 Å (Fits 5•6)].

[b] Multiple scattering paths represent combined paths, as described previously (see Materials and Methods).

[c] Goodness of fit (R_f for fits to filtered data; R_u for fits to unfiltered data) defined as

$$1000 * \frac{\sum_{i=1}^{N}\left\{\left[\mathrm{Re}(\chi_{i_{calc}})\right]^2 + \left[\mathrm{Im}(\chi_{i_{calc}})\right]^2\right\}}{\sum_{i=1}^{N}\left\{\left[\mathrm{Re}(\chi_{i_{data}})\right]^2 + \left[\mathrm{Im}(\chi_{i_{data}})\right]^2\right\}}$$

, where N is the number of data points.

[d] Addition of a Zn•C scattering path (0.5 C/Zn) to the parameters of this fit led to a refined Zn•C distance of 2.55 Å (σ^2 = 5.3 x 10^{-3} Å^2) and minimal improvement in fit residual to R_f = 20.

[e] Addition of a Zn•C scattering path (0.5 C/Zn) to the parameters of this fit led to a refined Zn•C distance of 2.51 Å (σ^2 = 1.3 x 10^{-3} Å^2) and minor improvement in fit residual to R_f = 8.

Zn K-edge XAS of the B1 MβL CcrA.

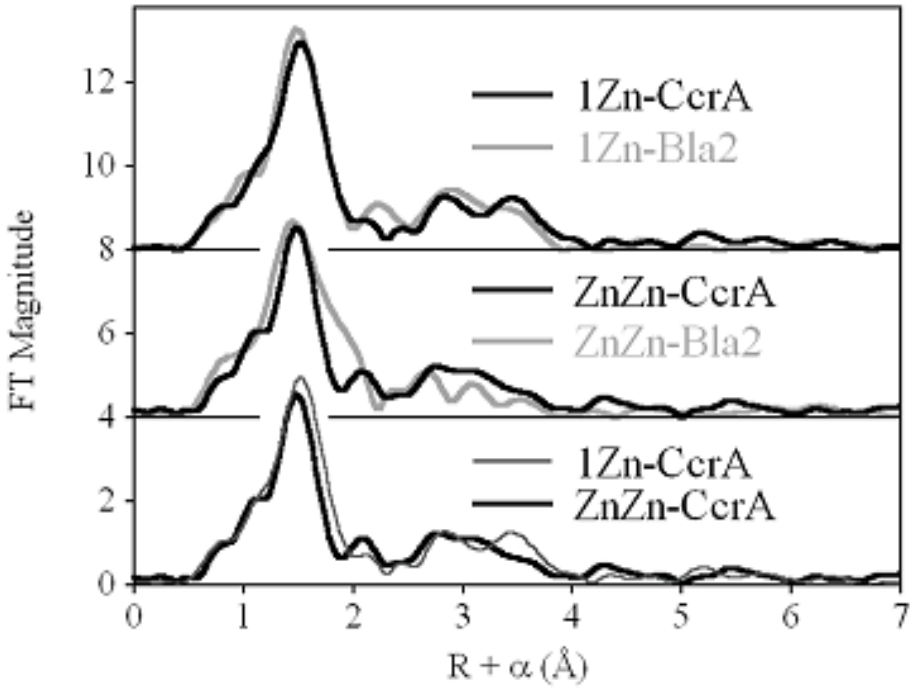

Figure S7. EXAFS Fourier transforms for Zn-CcrA. (Top) Direct comparison of 1Zn-CcrA (black line) and 1Zn-Bla2 (gray line). (Center) Direct comparison of ZnZn-CcrA (black line) and ZnZn-Bla2 (gray line). (Bottom) Direct comparison of 1Zn-CcrA (thin black line) and ZnZn-CcrA (thick black line).

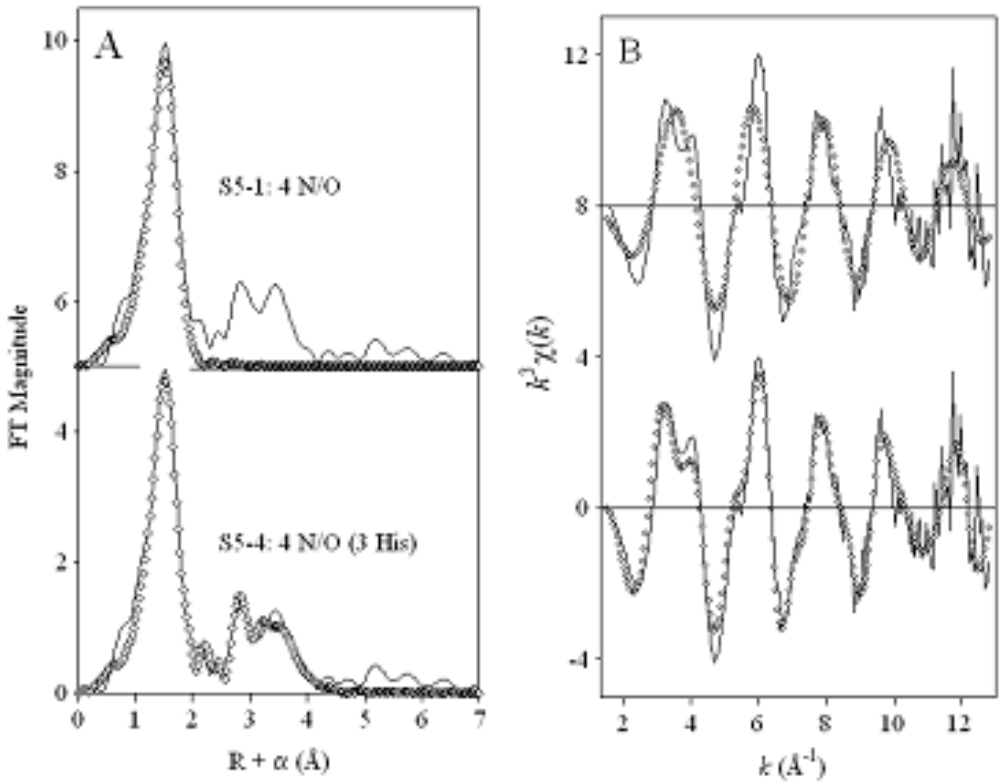

Figure S8. Fourier transforms (A) of k^3-weighted EXAFS (B) for 1Zn-CcrA (solid lines), and corresponding curve fits (open symbols) from Table S5.

Table S5. Detailed EXAFS curve fitting results for 1-Zn CcrA.[a]

Fit	Model	*Zn•N/O*	*Zn•S*	*Zn•His*[b]	*Zn•Zn*	R_f[c]	R_u[c]
S5•1	4 N/O	2.02 (4.6)				55	198
S5•2	4 N/O + 0.5 S	1.99 (6.0)	2.19 (7.2)			41	175
S5•3	3 N + 1 O	[N] 2.03 (2.3) [O] 1.89 (1.8)				42	176
S5•4	4 N/O (3 His)	2.03 (6.9)		2.91 (6.6), 3.16 (9.8) 4.11 (19), 4.42 (23)		26	88
S5•5	4 N/O (3 His) + Zn•Zn	2.03 (6.9)		2.91 (7.6), 3.16 (10) 4.12 (18), 4.41 (21)	3.32 (9.0)	24	88

[a] Distances (Å) and disorder parameters (in parentheses, σ^2 (10^{-3} Å^2)) shown derive from integer or half-integer coordination number fits to filtered EXAFS data [k = 1.5–12.6 Å^{-1}; R = 0.7–2.2 Å (fits 1–3) or 0.2–4.2 Å (fits 4–5)].

[b] Multiple scattering paths represent combined paths, as described previously (see Materials and Methods).

[c] Goodness of fit (R_f for fits to filtered data; R_u for fits to unfiltered data) defined as

$$1000 * \frac{\sum_{i=1}^{N}\left[\mathrm{Re}(\chi_{i_{exp}}) - \mathrm{Re}(\chi_{i_{sim}})\right]^2 + \left[\mathrm{Im}(\chi_{i_{exp}}) - \mathrm{Im}(\chi_{i_{sim}})\right]^2}{\sum_{i=1}^{N}\left[\mathrm{Re}(\chi_{i_{exp}})\right]^2 + \left[\mathrm{Im}(\chi_{i_{exp}})\right]^2}$$

, where N is the number of data points.

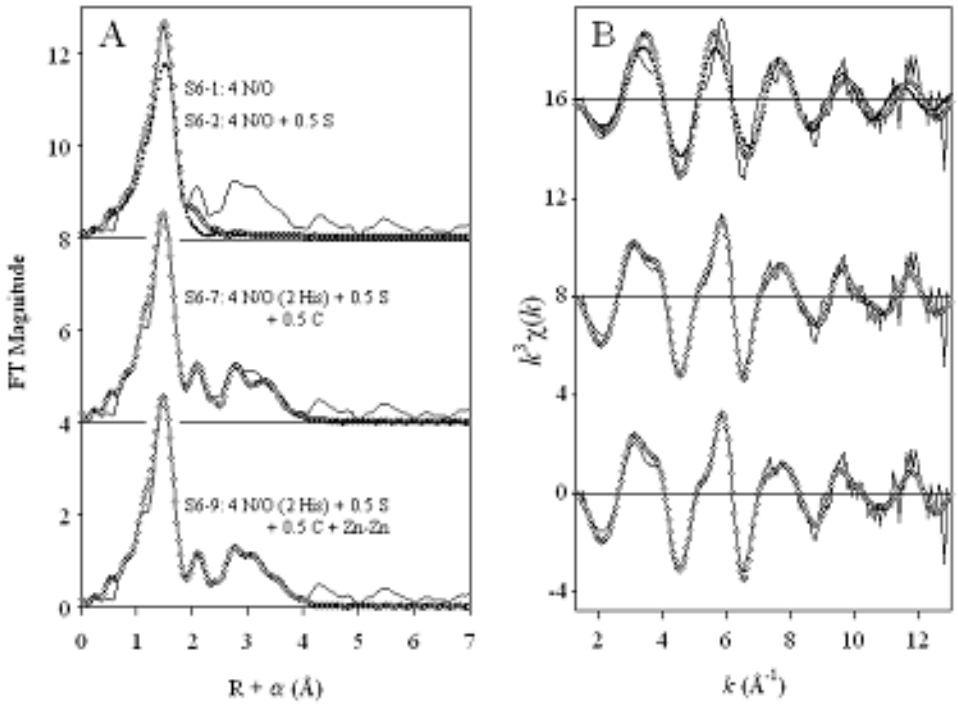

Figure S9. Fourier transforms (A) of k^3-weighted EXAFS (B) for ZnZn-CcrA (solid lines), and corresponding curve fits (open symbols, except S6-1 shown with filled symbols) from Table S6.

Table S6. Detailed EXAFS curve fitting results for ZnZn-CcrA.[a]

Fit	Model	Zn•N/O	Zn•S	$Zn \cdot C_{CO_2}$	Zn•His [b]	Zn•Zn	R_f [c]	R_u [c]
S6•1	4 N/O	2.04 (7.0)					125	243
S6•2	4 N/O + 0.5 S	2.02 (6.4)	2.33 (6.0)				65	218
S6•3	4 N/O + 1 S	2.03 (7.6)	2.32 (14)				103	237
S6•4	4 N/O + 0.5 S + 0.5 C	2.03 (6.2)	2.33 (6.6)	2.50 (0.8)			43	207
S6•5	4 N/O + 0.5 C	2.04 (6.8)		2.53 (0.1)			85	221
S6•6	4 N/O (2 His) + 0.5 S	2.03 (6.9)	2.33 (5.2)		2.92 (6.3), 3.17 (3.4) 4.11 (16), 4.42 (20)		54	90
S6•7	4 N/O (2 His) + 0.5 S + 0.5 C	2.03 (6.7)	2.33 (7.8)	2.48 (1.4)	2.91 (7.1), 3.14 (3.3) 4.11 (16), 4.42 (20)		45	79
S6•8	4 N/O (2 His) + 0.5 S + Zn•Zn	2.03 (6.8)	2.33 (5.7)		2.91 (7.6), 3.14 (8.7) 4.17 (23), 4.42 (18)	3.44 (11)	27	65
S6•9	4 N/O (2 His) + 0.5 S + Zn•Zn + 0.5 C	2.03 (5.9)	2.33 (4.5)	2.49 (1.4)	2.91 (6.8), 3.15 (3.5) 4.17 (22), 4.42 (18)	3.44 (11)	21	62

[a] Distances (Å) and disorder parameters (in parentheses, σ^2 (10^3 Å^2)) shown derive from integer or half•integer coordination number fits to filtered EXAFS data [k = 1.5•12.5 Å^{-1}; R = 0.7•2.3 Å (fits 1•5) or 0.2•4.2 Å (fits 6•9)].

[b] Multiple scattering paths represent combined paths, as described previously (see Materials and Methods)

[c] Goodness of fit (R_f for fits to filtered data, R_u for fits to unfiltered data) defined as

$$1000 * \frac{\sum_{i=1}^{N} \left[\mathrm{Re}(\chi_{i_{exp}}) - \mathrm{Re}(\chi_{i_{sim}}) \right]^2 + \left[\mathrm{Im}(\chi_{i_{exp}}) - \mathrm{Im}(\chi_{i_{sim}}) \right]^2}{\sum_{i=1}^{N} \left[\mathrm{Re}(\chi_{i_{exp}}) \right]^2 + \left[\mathrm{Im}(\chi_{i_{exp}}) \right]^2}$$, where N is the number of data points.

. Chapter IV

Metal Titration of BcII from *Bacillus cereus*

Introduction

There has been much controversy over the metal binding behavior of B1 metallo-β-lactamases. As previously noted, CcrA binds metals sequentially, populating the Zn_1 site completely before populating the Zn_2 site. Bla2 metal binding behavior varies depending on the metal. Zinc binds in the same manner as CcrA, while cobalt shows no preference for either site populating both sites regardless of stoichiometry. Recent spectroscopic evidence suggests the binding behavior of BcII from *Bacillus cereus* displays minimal preference for either site and may display cooperativity. [1]

Early studies of metal binding using competition titration shows a greater disparity of the metal binding affinities with a first dissociation constant of 0.62 nM and a second dissociation affinity of 1.50 μM. [2] A difference of three orders of magnitude between the two sites would fully populate the first site before occupying the other. The first crystal structure collected on BcII contained a single equivalent of zinc located in the Zn_1 (3H) site. [3] This evidence suggested that the binding is indeed sequential. Later studies have shown different results. Cobalt metal substitution data has shown that the metal incorporation is not sequential. [1] Substoichiometric additions of cobalt display UV-visible spectra corresponding to the Zn_1 (3H) site at the same time that it displays a LMCT band corresponding to a cobalt-sulfur bond formation. An EPR titration of apo-BcII with cobalt displays the presence of four species. The primary species maximized at 0.8 equivalents and was described as axial. The secondary species maximized at 2.0

equivalents and was described as rhombic. The other two sites correspond to nonspecifically bound and solvent bound cobalt. There is also an observed discrepancy between the EPR detected cobalt equivalents and the quantity of cobalt added, which is attributed to an increase in the quantity of spin coupled cobalt (II) present in the bridged dicobalt species. [4]

The metal binding to BcII has been studied with mass spectrometry, which shows that the mass corresponding to dizinc BcII grows consistently from zero to two equivalents as the population of apo BcII steadily decreases and the population of monozinc BcII grows to a small population (20%) before disappearing. [5] A kinetic analysis of the zinc and cobalt substituted enzymes have suggested similar results. [6, 7] These studies show cooperativity in the binding and a loss of metal ion during the hydrolysis of substrate. The enzyme would then require the addition of a metal from the surroundings to regenerate the active site.

Studying the metal binding behavior of BcII will help to elucidate the active form of BcII. Reports of the active form of this enzyme vary as much as the metal binding behavior. The active form of the enzyme is necessary to pinpoint in order to understand the reaction mechanism and to facilitate rational inhibitor design. There have been reports that each of the possible forms of the enzyme is the active form. The mononuclear Zn form present in the initial crystal structures suggested that the Zn_1 site is the active form. [3] A recent study of mutations within the Zn_2 site demonstrates a reduction of rate if metal binding is disrupted. [1] Another study suggest that the enzyme's physiological state is apo, but the binding of substrate induces a conformational change that results in

the binding of necessary metal from the surroundings. [8] The dinuclear form of the enzyme is suggested in more recent studies as the active form of the enzyme. [5]

In summary, the picture of metal binding to BcII has evolved over time and a clear picture has yet to emerge. This study will use x-ray absorption spectroscopy to look at the BcII active site as both zinc and cobalt are added to the site.

Experimental Procedures

BcII containing one half, one, and two equivalents of Zn (II) and Co (II) was perpared and characterized according to published procedures by our collaborators. Samples for EXAFS (0.5-2 mM) were prepared as previously described. Data collection and analysis were performed as described in preceding chapters.

Results

Previous spectroscopic experiments of BcII suggests that both the Zn_1 and Zn_2 sites become populated simultaneously with as little as 0.3 equivalents of metal. With 0.5 equivalents of Co (II), the fewest equivalents available for this study, the best fits to the EXAFS data are in agreement with this observation. The fits show a mixture of both the Zn_1 and Zn_2 sites including four nitrogen atoms, half of a sulfur atom, and two histidines, which is the average coordination sphere of the two sites. The fit residual improves by 30% with the addition of a Co-Co interaction at 3.56 Å. (Figure 4-2) This distance is similar to the reported values of other di-cobalt enzymes and ~0.1 Å longer than the 3.4 Å expected from the di-zinc enzyme (based on crystal structures). The one equivalent form of cobalt-substituted BcII is best fit by the same structural model as the one half

equivalent form. (Figure 4-3) The bond distances, peak height, and disorder terms are virtually identical between the two fits. However, the fit residual improves by 50% upon addition of a Co-Co distance of 3.56 Å. The two equivalent form of cobalt-substituted BcII has a distinct appearance from the other two samples. (Figure 4-4) The intensity corresponding to the shell of atoms directly bound to the cobalt increases by approximately 50%, which corresponds to a decrease in the disorder terms in the nitrogen and sulfur shells. There is also a lengthening of two of the histidine secondary scattering pathways. Addition of a Co-Co distance of 3.56 Å improves the fit by 30%.

The zinc-substituted BcII shows similar trends to the cobalt-substituted form. With one half of an equivalent of zinc (II), both the Zn_1 and Zn_2 sites appear to be populated. The best fits include 4 nitrogen atoms and 0.5 sulfur atoms with two histidine residues. There is a 25% improvement of the fit residual on addition of a Zn-Zn distance of 3.4 Å. (Figure 4-5) Moving to one equivalent of zinc (II), the best fit remains a mixture of Zn_1 and Zn_2, with the addition of a Zn-Zn interaction improving the fit by nearly 30%. (Figure 4-6) With the ZnZn form of BcII, the best fit uses the same structural model, but the addition of a Zn-Zn interaction improves the fit by 45%. (Figure 4-7) With increasing equivalents of metal ions, the disorder terms decrease, which suggests that the sites become more ordered.

Discussion

The BcII metal titration performed allows us to monitor metal binding behavior at substoichiometric metal concentrations. BcII appears to show cooperativity in binding of metal. With even a modest addition of metal, metal fills both sites in the active site.

Additionally, the improvement of fit upon the addition of a metal-metal interaction suggests that the site is well ordered and contains a bridge between the metals. The lowering of the disorder terms with higher equivalents of metal suggests that there may be small portions of the sample that exists in the monozinc form, but the fraction is reduced as the sample becomes saturated and moves to a single stable species.

The metal titration of BcII analyzed by EXAFS shows metal binding behavior unlike the previously studied members of subclass B1. Combined with the analysis of metal binding in Bla2 [9] and CcrA, [9, 10] subclass B1 displays three unique modes of binding metal. With the members of the subclass having the same coordinating residues, these differences in binding modes must be attributed to more subtle interactions such as hydrogen bonding networks, orientation and arrangement of coordinating residues, backbone flexibility, and the local environment of the active site.

The metal binding behavior of the B1 metallo-β-lactamase, CcrA has been well characterized by optical, magnetic resonance, and X-ray absorption studies. These studies show sequential binding with both zinc and cobalt. Similar to the monozinc crystal structure of BcII, the initial equivalents of metal bind to the Zn_1 (3H) site, which suggests that the binding affinity of the Zn_1 (3H) site in CcrA is higher than the Zn_1 (DCH) site. This suggests that either the sites have similar binding affinity or upon addition of the first equivalent of metal the binding site affinity of the second site becomes greater, encouraging the formation of the dimetal form. The X-ray absorption evidence of a metal-metal bridge formed with modest additions of metal argues for the latter option. The sequence homology between the two enzymes is only modest (32%) but both retain the HXHXD motif that is present in all metallo-β-lactamase as well as stretches of

conserved animo acids and thirteen conserved glycines. The variations in primary sequence allows for the metal binding behavior to be tuned differently, while still maintaining the stable metallo-β-lactamase fold.

Comparing BcII metal-binding behavior to Bla2 provides a much more compelling comparison. The two sequences are nearly identical (92% homology) with only three changes in the active site pocket, but the metal binding behavior is vastly different. [1, 10, 11] Bla2 shows different binding behavior depending on the metal ion presented to it, whereas BcII binds both Zn (II) and Co (II) the same way. There are three different amino acids present in the secondary shell of the active site, which could contribute to the change in metal binding behavior. The first difference occurs at position 39, where an isoleucine is replaced with to a valine. Such a modification is relatively minor, as both groups have the same charge and polarity. The only difference is the shortening of an aliphatic chain by a single carbon. This change should do little to affect the overall protein structure, but the aliphatic sidechain is only 4.1 Å away from histidine 210. The variation of the distance of the carbon chain from the binding residue may indirectly influence the binding affinity. The second alteration between the two sites is the replacement of glycine 151 with a glutamate. This introduces a large, bulky, charged group in the place of a hydrogen atom. On the surface of the protein, this disruption will be far less important than if a residue was imbedded in the internal structure, with the charge interacting with solvent molecules instead of the hydrophobic core. However, the this residue is two amino acids away from a histidine residue in the Zn_1 (3H) site. The increased flexibility of the glycine residue and the side chain could modify the backbone alignment enough to attenuate the metal binding behavior. The final difference is at

position 182 with modification of a threonine to an alanine. This residue is on the edge of the active site pocket and introduces a hydrogen bonding residue, which can modify the existing water network in the active site. With two waters involved in coordinating the metal centers, the modification of the hydrogen bonding network could provide the observed metal binding attenuation. With three mutations responsible for different metal-binding behavior, it may be possible with site-directed mutagenesis further probe the source of these differences.

Comparison to two other members of the B1 subclass shows three distinct binding modes. BcII displays cooperativity and adopts the ZnZn or CoCo form at substoiciometric metal content. CcrA shows sequential binding with both zinc (II) and cobalt (II). It fills the Zn_1 site completely before adding metal to the Zn_2 site. Bla2 behaves as CcrA when the metal added is zinc (II), but behaves as BcII when the metal added is cobalt (II). With this wide variety of binding behaviors, it is important to note that the binding coordination sphere is identical in all of these cases, and secondary interactions in the active site are a likely cause of the binding differences.

Summary

The metal binding behavior of metallo-β-lactamase, BcII was studied with x-ray absorption spectroscopy. These studies show that metal binding to the enzyme occur concurrently at the Zn_1 and Zn_2 sites in the active site in substoichiometric quantities of metal. The EXAFS fits improve upon addition of a metal-metal distance in all samples studied, which suggests that the metal binding to BcII displays positive cooperativity for both zinc and cobalt. These studies further support other studies showing the positive

cooperativity in the metal binding of BcII. The metal binding behavior of BcII differs from the other members of the B1 subclass studied by x-ray absorption spectroscopy.

References

1. Llarrull, L.I., et al., *Evidence for a Dinuclear Active Site in the Metallo-β-lactamase BcII with SubStoichiometric Co(II).* Journal of Biological Chemistry, 2007. **282**(42): p. 30586-30595.

2. de Seny, D., et al., *Metal Ion Binding and Coordination Geometry for Wild Type and Mutants of Metallo-β-Lactamase from Bacillus cereus 569/H/9 (BcII).* Biological Chemistry, Journal of, 2001. **276**(48): p. 45065-45078.

3. Carfi, A., et al., *The 3-D Structure of a Zinc Metallo-β-Lactamase from Bacillus cereus Reveals A New-Type of Protein Fold* EMBO Journal, 1995. **14**(20): p. 4914-4921.

4. Tioni, M.F., et al., *Trapping and Characterization of a Reaction Intermediate in Carbapenem Hydrolysis by B. cereus Metallo-β-lactamase.* American Chemical Society, Journal of, 2008. **130**: p. 15852-15863.

5. Jacquin, O., et al., *Positively Cooperative Binding of Zinc Ions to Bacillus cereus 569/H/9 β-lactamaase II Suggests that the Ninuclear enzyme is the Only Relevant Form for Catalysis.* Molecular Biology, Journal of, 2009. **392**: p. 1278-1291.

6. Badarau, A., C. Damblon, and M.I. Page, *The Activity of the Dinuclear Cobalt-β-lactamase from Bacillus cereus in Catalysing the Hydrolysis of β-lactams.* Biochemical Journal, 2007. **401**: p. 197-203.

7. Badarau, A. and M.I. Page, *Loss of Enzyme Activity During Turnover of the Bacillus cereus β-lactamase Catalyzed Hydrolysis of β-lactams due to loss of zinc ion.* Journal of Biological Inorganic Chemistry, 2008. **13**: p. 919-928.

8. Wommer, S., et al., *Substrate-activated Zinc Binding of Metallo-β-Lactamases.* Biological Chemistry, Journal of, 2002. **277**(27): p. 24142-24147.

9. Hawk, M.J., et al., *Differential Binding of Co(II) and Zn(II) to Metallo-β-lactamase Bla2 from Bacillus anthracis.* Journal of the American Chemical Society, 2009. **131**(30): p. 10753-10762.

10. Periyannan, G., et al., *Sequential Binding of Co(II) to Metallo-β-Lactamase CcrA.* Biochemistry, 2006. **45**(4): p. 1313-1320.

11. Materon, I.C., et al., *Biochemical Characterization of β-Lactamase Bal1 and Bla2 from Bacillus anthracis.* Antimicrobial Agents and Chemotherapy, 2003. **47**(6): p. 2040-2042.

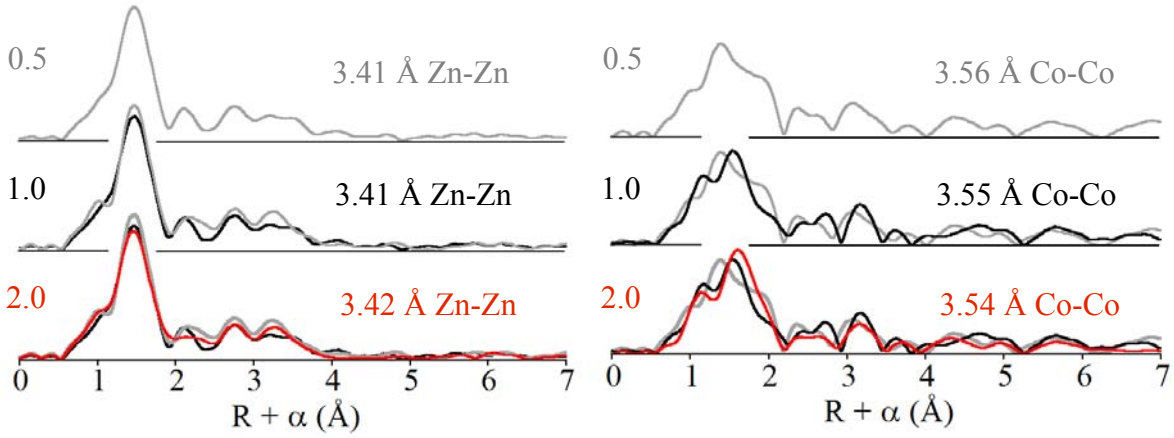

Figure 4-1: Comparison Plot of BcII Titration. Zinc titration (left) and Cobalt titration (right) with 0.5 equivalents (grey), 1.0 equivalent (black), and 2.0 equivalents (red) of metal

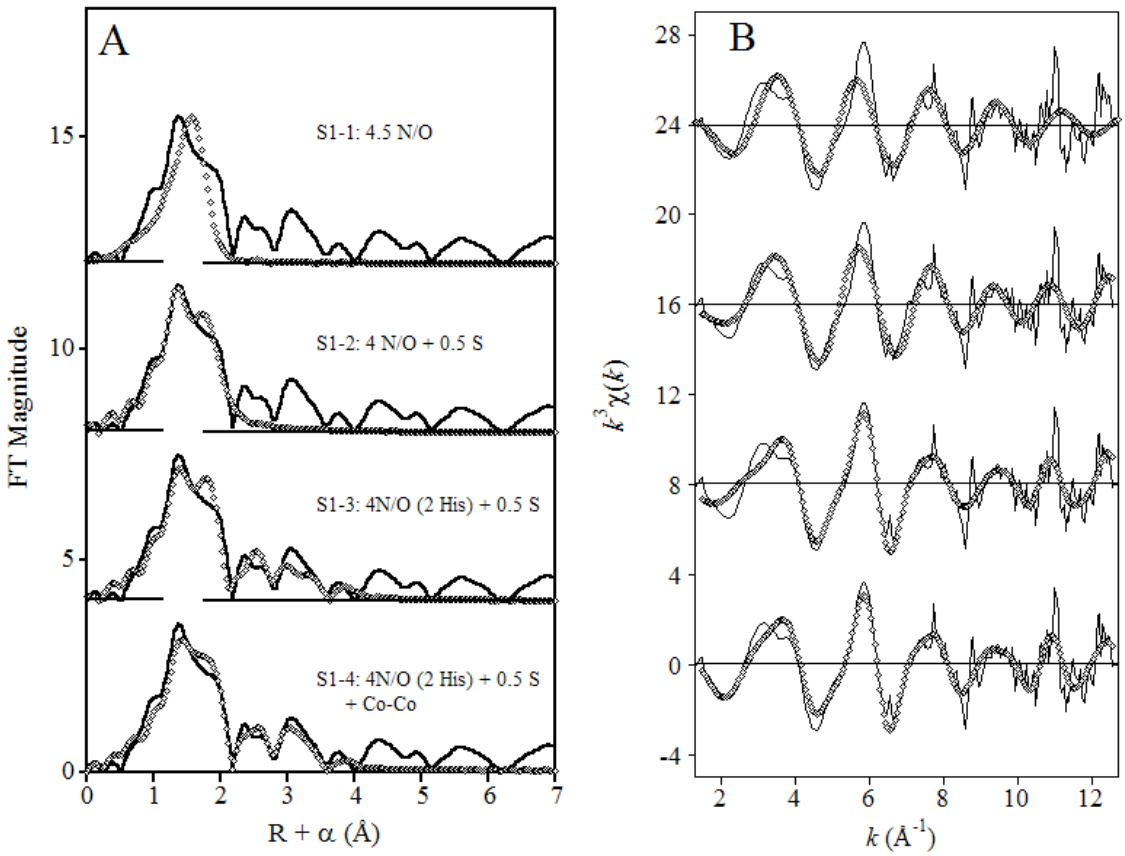

Figure 4-2. Fourier transforms (A) of k^3-weighted EXAFS (B) for 0.5Co-BcII (solid lines), and corresponding curve fits (open symbols) from Table 4-1.

Table 4-1. Detailed EXAFS curve fitting results for 0.5Co-BcII.[a]

Fit	Model	*Co-N/O*	*Co-S*	*Co-His* [b]	*Co-Co*	R_f [c]	R_u [c]
S1-1	4.5 N/O	2.10 (7.4)				152	384
S1-2	4 N/O + 0.5 S	2.02 (8.5)	2.28 (0.8)			32	255
S1-3	4 N/O (2His) + 0.5 S [d]	2.02 (8.4)	2.27 (0.9)	2.89 (4.2), 3.31 (20) 4.08 (6.4), 4.25 (9.5)		125	180
S1-4	4 N/O (2His) + 0.5 S + Co-Co [d]	2.03 (6.9)	2.28 (1.7)	2.94 (2.2), 3.25 (14) 4.00 (10), 4.28 (16)	3.56 (8.8)	76	134

[a] Distances (Å) and disorder parameters (in parentheses, σ^2 (10^{-3} Å^2)) shown derive from integer or half-integer coordination number fits to filtered EXAFS data [k = 1.5-12.5 Å^{-1}; R = 0.7-2.3 Å (fits 1-2) or 0.2-4.2 Å (fits 3-4)].

[b] Multiple scattering paths represent combined paths, as described previously (see Materials and Methods).

[c] Goodness of fit (R_f for fits to filtered data; R_u for fits to unfiltered data) defined as

$$1000 * \frac{\sum_{i=1}^{N} \left\{ \left[\mathrm{Re}(\chi i_{calc}) \right]^2 + \left[\mathrm{Im}(\chi i_{calc}) \right]^2 \right\}}{\sum_{i=1}^{N} \left\{ \left[\mathrm{Re}(\chi i_{obs}) \right]^2 + \left[\mathrm{Im}(\chi i_{obs}) \right]^2 \right\}}$$

, where N is the number of data points.

[d] Inclusion of a Co-C scattering path (0.5 C/Co), along with the parameters of this fit, led to a refined Co-C distance of 2.50 Å (σ^2 = 0.3 x 10^{-3} Å^2), with a modest decrease in fit residual to R_f = 113.

[e] Inclusion of a Co-C scattering path (0.5 C/Co), along with the parameters of this fit, led to a refined Co-C distance of 2.52 Å (σ^2 = 0.6 x 10^{-3} Å^2), with a modest decrease in fit residual to R_f = 55.

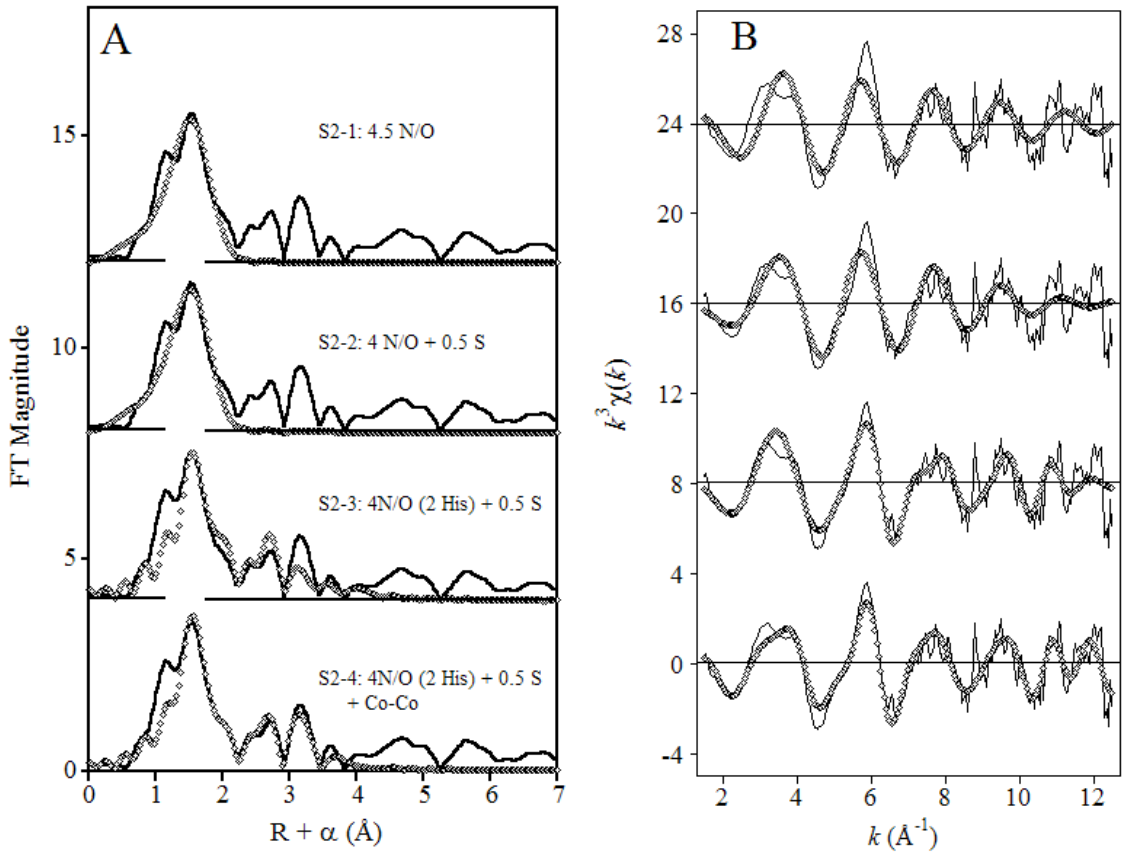

Figure 4-3. Fourier transforms (A) of k^3-weighted EXAFS (B) for 1Co-BcII (solid lines), and corresponding curve fits (open symbols) from Table 4-2.

Table 4-2. Detailed EXAFS curve fitting results for 1Co-BcII.[a]

Fit	Model	*Co-N/O*	*Co-S*	*Co-His* [b]	*Co-Co*	R_f [c]	R_u [c]
S2-1	4.5 N/O	2.11 (7.4)				124	384
S2-2	4 N/O + 0.5 S	2.05 (8.7)	2.28 (4.8)			47	355
S2-3	4 N/O (2His) + 0.5 S [d]	2.04 (9.7)	2.27 (5.0)	2.95 (2.0), 3.27 (20) 4.02 (23), 4.28 (13)		111	235
S2-4	4 N/O (2His) + 0.5 S + Co-Co [d]	2.03 (6.9)	2.27 (3.7)	2.94 (2.2), 3.25 (14) 4.00 (10), 4.28 (16)	3.55 (6.0)	63	177

[a] Distances (Å) and disorder parameters (in parentheses, σ^2 (10^{-3} Å^2)) shown derive from integer or half-integer coordination number fits to filtered EXAFS data [k = 1.5-12.5 Å^{-1}; R = 0.7-2.3 Å (fits 1-2) or 0.2-4.2 Å (fits 3-4)].

[b] Multiple scattering paths represent combined paths, as described previously (see Materials and Methods).

[c] Goodness of fit (R_f for fits to filtered data; R_u for fits to unfiltered data) defined as

$$1000 * \frac{\sum_{i=1}^{N} \left\{ \left[\mathrm{Re}(\chi_{i_{calc}}) \right]^2 + \left[\mathrm{Im}(\chi_{i_{calc}}) \right]^2 \right\}}{\sum_{i=1}^{N} \left\{ \left[\mathrm{Re}(\chi_{i_{obs}}) \right]^2 + \left[\mathrm{Im}(\chi_{i_{obs}}) \right]^2 \right\}}$$

, where N is the number of data points.

[d] Inclusion of a Co-C scattering path (0.5 C/Co), along with the parameters of this fit, led to a refined Co-C distance of 2.53 Å (σ^2 = 0.1 x 10^{-3} Å^2), with a modest decrease in fit residual to R_f = 100.

[e] Inclusion of a Co-C scattering path (0.5 C/Co), along with the parameters of this fit, led to a refined Co-C distance of 2.52 Å (σ^2 = 0.6 x 10^{-3} Å^2), with a modest decrease in fit residual to R_f = 55.

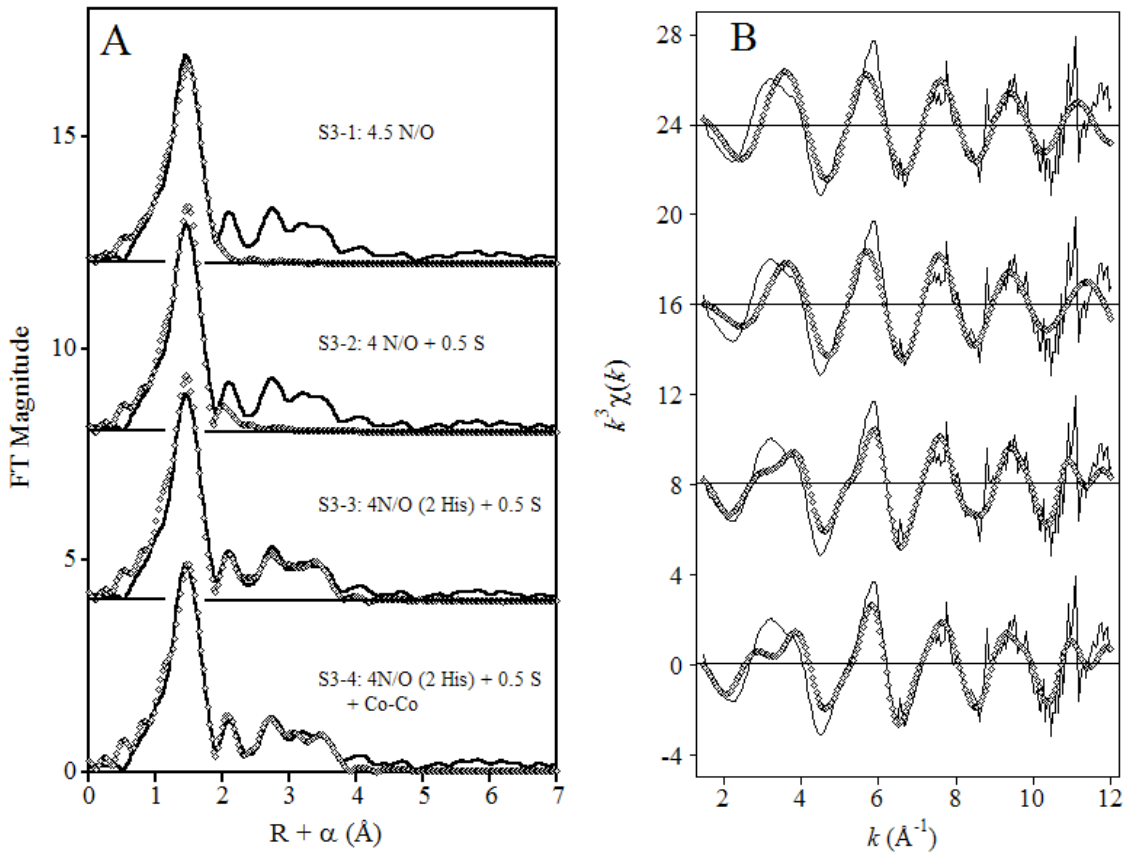

Figure 4-4. Fourier transforms (A) of k^3-weighted EXAFS (B) for CoCo-BcII (solid lines), and corresponding curve fits (open symbols) from Table 4-3.

Table 4-3. Detailed EXAFS curve fitting results for CoCo-BcII.[a]

Fit	Model	*Co-N/O*	*Co-S*	*Co-His* [b]	*Co-Co*	R_f [c]	R_u [c]
S3-1	4.5 N/O	2.12 (5.1)				119	309
S3-2	4 N/O + 0.5 S	2.08 (1.8)	2.32 (1.7)			92	288
S3-5	4 N/O (2His) + 0.5 S [d]	2.08 (2.6)	2.33 (1.5)	2.95 (5.8), 3.19 (16) 4.13 (6.9), 4.32 (6.6)		172	221
S3-6	4 N/O (2His) + 0.5 S + Co-Co [e]	2.09 (1.3)	2.32 (1.4)	2.93 (1.8), 3.19 (14) 4.18 (14), 4.32 (12)	3.52 (8.4)	125	202

[a] Distances (Å) and disorder parameters (in parentheses, σ^2 (10^{-3} Å^2)) shown derive from integer or half-integer coordination number fits to filtered EXAFS data [k = 1.5-12.4 Å^{-1}; R = 0.7-2.3 Å (fits 1-2) or 0.2-4.2 Å (fits 3-4)].

[b] Multiple scattering paths represent combined paths, as described previously (see Materials and Methods).

[c] Goodness of fit (R_f for fits to filtered data; R_u for fits to unfiltered data) defined as

$$1000 * \frac{\sum_{i=1}^{N} \left\{ \left[\mathrm{Re}(\chi_{i_{calc}}) \right]^2 + \left[\mathrm{Im}(\chi_{i_{calc}}) \right]^2 \right\}}{\sum_{i=1}^{N} \left\{ \left[\mathrm{Re}(\chi_{i_{obs}}) \right]^2 + \left[\mathrm{Im}(\chi_{i_{obs}}) \right]^2 \right\}}$$

, where N is the number of data points.

[d] Addition of a Co-C scattering path (0.5 C/Co) to the parameters of this fit led to a refined Co-C distance of 2.47 Å (σ^2 = 1.9 x 10^{-3} Å^2), with a minimal decrease in fit residual to R_f = 168.

[e] Addition of a Co-C scattering path (0.5 C/Co) to the parameters of this fit led to a refined Co-C distance of 2.48 Å (σ^2 = 1.0 x 10^{-3} Å^2), with a minimal decrease in fit residual to R_f = 115.

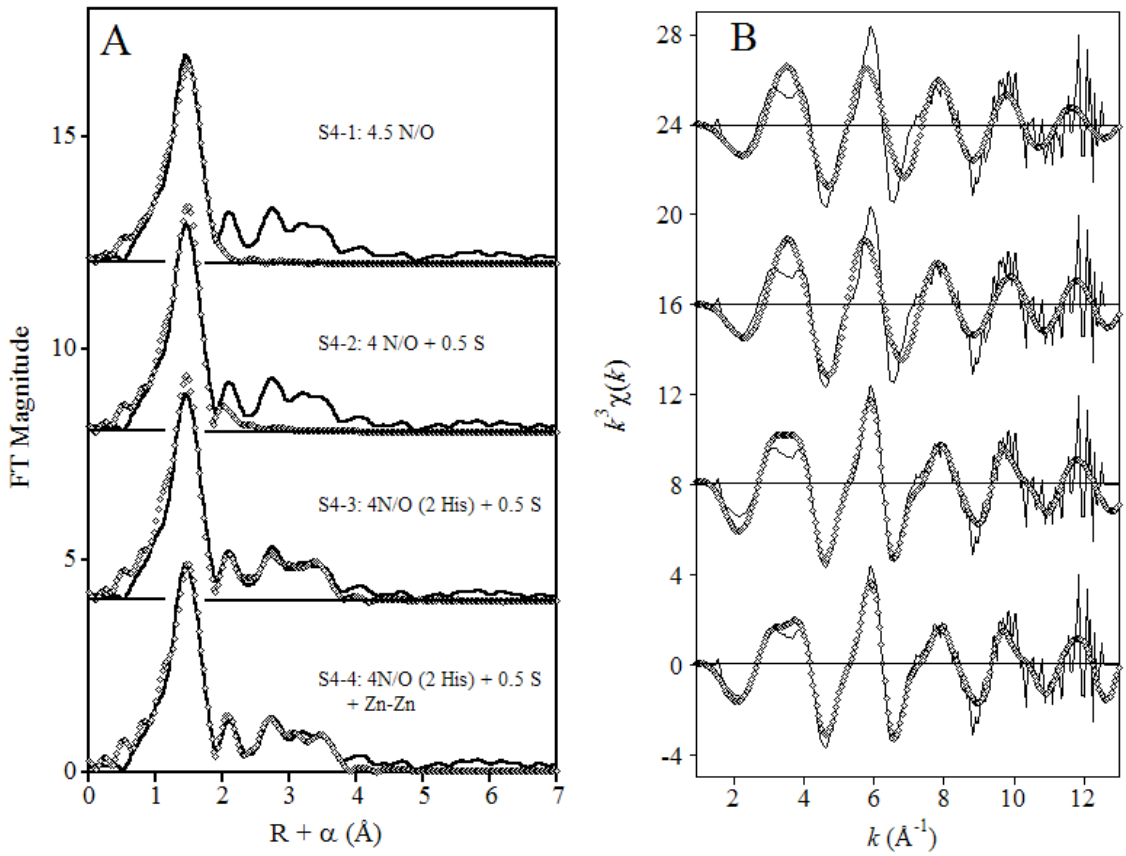

Figure 4-5. Fourier transforms (A) of k^3-weighted EXAFS (B) for 0.5Zn-BcII (solid lines), and corresponding curve fits (open symbols) from Table 4-4.

Table 4-4. Detailed EXAFS curve fitting results for 0.5Zn-BcII.[a]

Fit	Model	*Zn-N/O*	*Zn-S*	*Zn-His* [b]	*Zn-Zn*	R_f [c]	R_u [c]
S4-1	4.5 N/O	2.01 (6.6)				113	207
S4-2	4 N/O + 0.5 S	2.00 (4.9)	2.30 (5.8)			71	181
S4-3	4 N/O (2 His) + 0.5 S [d]	2.00 (4.5)	2.29 (6.3)	2.93 (0.6), 3.18 (2.0) 4.11 (10), 4.43 (14)		34	63
S4-4	4 N/O (2 His) + 0.5 S [e] + Zn-Zn	2.00 (5.0)	2.30 (8.0)	2.95 (1.6), 3.21 (5.0) 4.12 (9.0), 4.41 (21)	3.41 (13)	26	53

[a] Distances (Å) and disorder parameters (in parentheses, σ^2 (10^{-3} Å^2)) shown derive from integer or half-integer coordination number fits to filtered EXAFS data [k = 1.5-12.5 Å^{-1}; R = 0.7-2.2 Å (fits 1-2) or 0.2-4.2 Å (fits 3-4)].

[b] Multiple scattering paths represent combined paths, as described previously (see Materials and Methods).

[c] Goodness of fit (R_f for fits to filtered data; R_u for fits to unfiltered data) defined as

$$1000 * \frac{\sum_{i=1}^{N} \left\{ \left[\mathrm{Re}(\chi_{i_{calc}}) \right]^2 + \left[\mathrm{Im}(\chi_{i_{calc}}) \right]^2 \right\}}{\sum_{i=1}^{N} \left\{ \left[\mathrm{Re}(\chi_{i_{obs}}) \right]^2 + \left[\mathrm{Im}(\chi_{i_{obs}}) \right]^2 \right\}}$$

, where N is the number of data points.

[d] Inclusion of a Zn-C scattering path (0.5 C/Zn), along with the parameters of this fit, led to a refined Zn-C distance of 2.49 Å (σ^2 = 5.4 x 10^{-3} Å^2), with a modest decrease in fit residual to R_f = 25.

[e] Inclusion of a Zn-C scattering path (0.5 C/Zn), along with the parameters of this fit, led to a refined Zn-C distance of 2.50 Å (σ^2 = 5.1 x 10^{-3} Å^2), with a modest decrease in fit residual to R_f = 18.

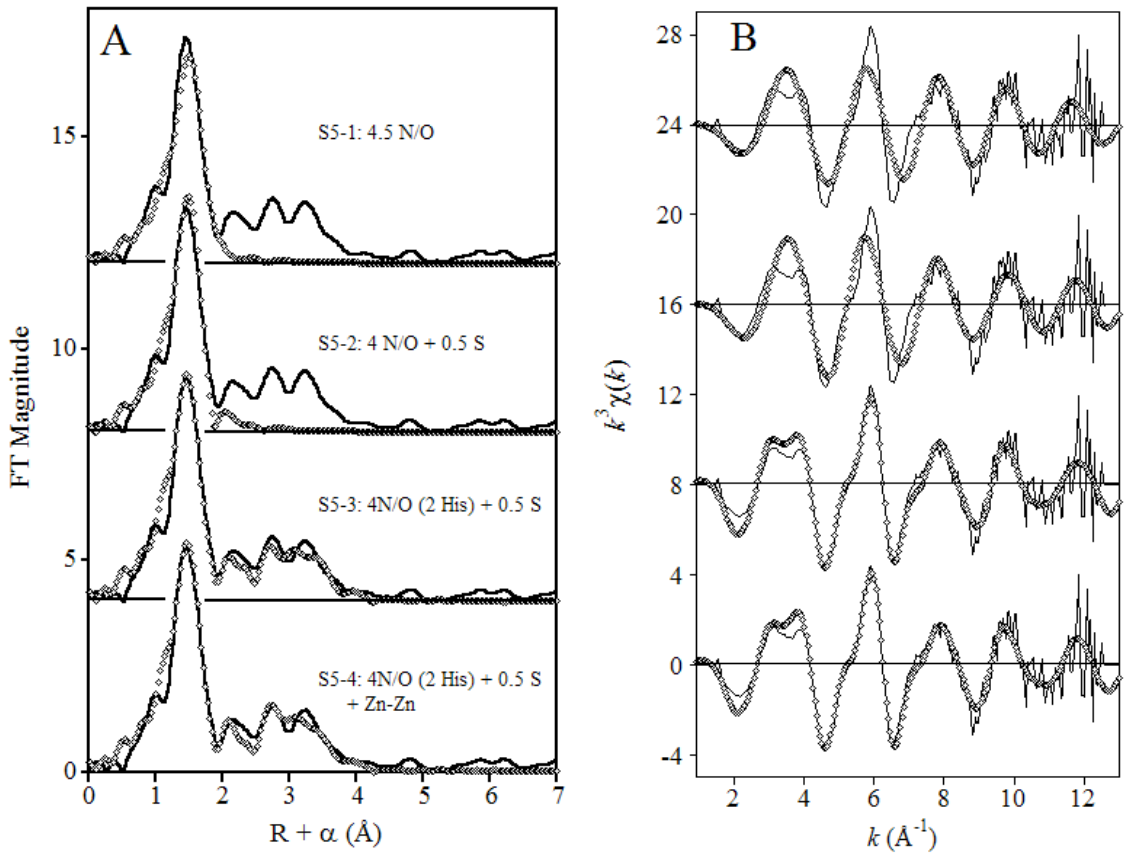

Figure 4-6. Fourier transforms (A) of k^3-weighted EXAFS (B) for 1Zn-BcII (solid lines), and corresponding curve fits (open symbols) from Table 4-5.

Table 4-5. Detailed EXAFS curve fitting results for 1Zn-BcII.[a]

Fit	Model	*Zn-N/O*	*Zn-S*	*Zn-His* [b]	*Zn-Zn*	R_f [c]	R_u [c]
S5-1	4.5 N/O	2.00 (4.6)				109	294
S5-2	4 N/O + 0.5 S	2.00 (5.0)	2.29 (6.3)			70	261
S5-3	4 N/O (2 His) + 0.5 S [d]	2.00 (4.5)	2.29 (6.3)	2.93 (0.6), 3.18 (2.0) 4.08 (12), 4.44 (14)		44	139
S5-4	4 N/O (2 His) + 0.5 S + Zn-Zn	2.03 (6.6)	2.30 (7.0)	2.93 (0.6), 3.18 (2.0) 4.08 (13), 4.44 (14)	3.41 (20)	32	46

[a] Distances (Å) and disorder parameters (in parentheses, σ^2 (10^{-3} Å^2)) shown derive from integer or half-integer coordination number fits to filtered EXAFS data [k = 1.5-12.5 Å^{-1}; R = 0.7-2.2 Å (fits 1-4) or 0.2-4.2 Å (fits 5-6)].

[b] Multiple scattering paths represent combined paths, as described previously (see Materials and Methods).

[c] Goodness of fit (R_f for fits to filtered data; R_u for fits to unfiltered data) defined as

$$1000 * \frac{\sum_{i=1}^{N} \left\{ \left[\mathrm{Re}(\chi_{i_{calc}}) \right]^2 + \left[\mathrm{Im}(\chi_{i_{calc}}) \right]^2 \right\}}{\sum_{i=1}^{N} \left\{ \left[\mathrm{Re}(\chi_{i_{obs}}) \right]^2 + \left[\mathrm{Im}(\chi_{i_{obs}}) \right]^2 \right\}}$$

, where N is the number of data points.

[d] Inclusion of a Zn-C scattering path (0.5 C/Zn), along with the parameters of this fit, led to a refined Zn-C distance of 2.50 Å (σ^2 = 16 x 10^{-3} Å^2), with a modest decrease in fit residual to R_f = 39.

[e] Inclusion of a Zn-C scattering path (0.5 C/Zn), along with the parameters of this fit, led to a refined Zn-C distance of 2.51 Å (σ^2 = 11 x 10^{-3} Å^2), with a modest decrease in fit residual to R_f = 39.

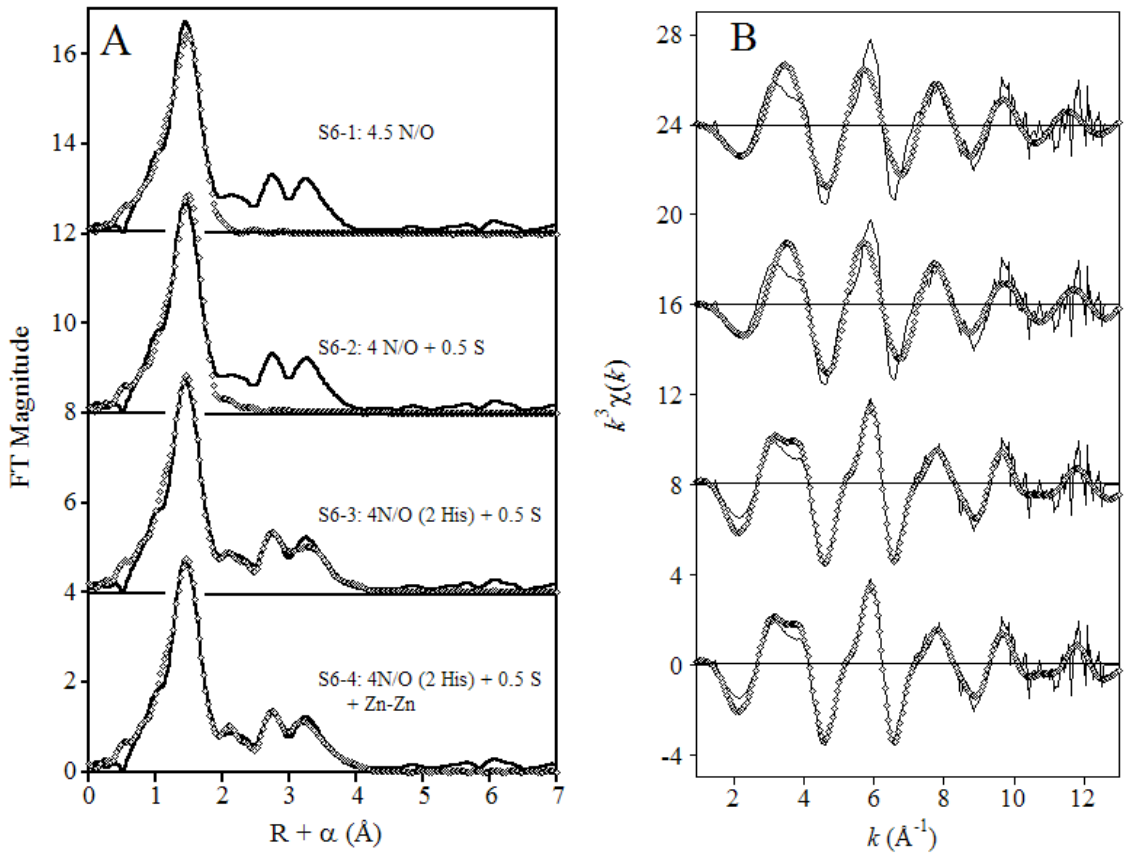

Figure 4-7. Fourier transforms (A) of k^3-weighted EXAFS (B) for ZnZn-BcII (solid lines), and corresponding curve fits (open symbols) from Table 4-6.

Table 4-6. Detailed EXAFS curve fitting results for ZnZn-BcII.[a]

Fit	Model	*Zn-N/O*	*Zn-S*	*Zn-His* [b]	*Zn-Zn*	R_f [c]	R_u [c]
S6-1	4.5 N/O	2.02 (6.4)				96	214
S6-2	4 N/O + 0.5 S	2.01 (5.9)	2.29 (6.4)			57	206
S6-3	4 N/O (2His) + 0.5 S [d]	2.01 (5.8)	2.29 (6.0)	2.93 (0.6), 3.17 (1.4) 4.09 (14), 4.43 (16)		19	89
S6-4	4 N/O (2His) + 0.5 S [e] + Zn-Zn [e]	2.04 (6.3)	2.27 (2.6)	2.90 (7.1), 3.18 (5.8) 4.08 (18), 4.43 (25)	3.42 (13)	10	71

[a] Distances (Å) and disorder parameters (in parentheses, σ^2 (10^{-3} Å^2)) shown derive from integer or half-integer coordination number fits to filtered EXAFS data [k = 1.5-12.5 Å^{-1}; R = 0.7-2.3 Å (Fits 1-2) or 0.2-4.0 Å (Fits 3-4)].

[b] Multiple scattering paths represent combined paths, as described previously (see Materials and Methods).

[c] Goodness of fit (R_f for fits to filtered data; R_u for fits to unfiltered data) defined as

$$1000 * \frac{\sum_{i=1}^{N} \left\{ \left[\mathrm{Re}(\chi_{i_{calc}}) \right]^2 + \left[\mathrm{Im}(\chi_{i_{calc}}) \right]^2 \right\}}{\sum_{i=1}^{N} \left\{ \left[\mathrm{Re}(\chi_{i_{obs}}) \right]^2 + \left[\mathrm{Im}(\chi_{i_{obs}}) \right]^2 \right\}}$$

, where N is the number of data points.

[d] Addition of a Zn-C scattering path (0.5 C/Zn) to the parameters of this fit led to a refined Zn-C distance of 2.49 Å (σ^2 = 10 x 10^{-3} Å^2) and minimal improvement in fit residual to R_f = 16.

[e] Addition of a Zn-C scattering path (0.5 C/Zn) to the parameters of this fit led to a refined Zn-C distance of 2.50 Å (σ^2 = 1.3 x 10^{-3} Å^2) and minor improvement in fit residual to R_f = 9.

Chapter V

Rapid Freeze Quench Studies of L1

This chapter includes work published in Breece, R.M.; Hu,; X. Bennett, B.; Crowder, M.W.; Tierney D.L. *Journal of the American Chemical Society*, 2009, 131, 11642-11643.

Introduction

The mechanism of metallo-β-lactamses remains a target of great interest. Understanding the mechanism could provide links between the three subclasses and could lead to the eventual design of a universal inhibitor. Previous studies have looked at the reaction kinetics of native and metal substituted L1. These studies have found that the enzyme is active against a wide array of β-lactam antibiotics. Against one cephalosporin, nitrocefin, a reaction intermediate was discovered by stopped-flow UV-visible spectroscopy. [1] The intermediate species displays a distinctive absorption at 665 nm compared to 390 nm for the substrate and 485 nm for the product. The intermediate structure is thought to be ring-opened with negative charge present on the formerly amide nitrogen. Extended conjugation along the unique sidechain (Figure 5-1) is thought to stabilize the intermediate. [1-4] Another report suggests that the negative charge is stabilized by an interaction with the divalent active site metal [5], however the energy of the absorption is independent of the metal present in the active site suggesting it is primarily an intermediate based transition. [1, 6] A crystal structure of the ring-opened product of the nitrocefin covalently linked to a class A penicillin binding protein [7]

(Figure 5-2) suggests the nitrogen is involved in conjugation with the adjacent double bond. The carbon-nitrogen-carbon bond angle in this structure is 129 degrees and is in plane of the double bond. The dinitrostyrene sidechain appears to extend the conjugation. Though in this structure, a rotation of the phenyl ring disrupts the planarity of the system. This intermediate has been seen in the dizinc and dicobalt forms of L1, but its presence in the monozinc form is diminished and it is not observed with monocobalt form. [8]

The metal binding behavior of the native and cobalt-substituted forms of the enzyme has been well defined using EXAFS, [9] EPR, paramagnetic ^{1}H NMR and UV-visible spectroscopy. [6] EXAFS showed the two equivalents of metal are bound at the active site and the metals are bridged, with a zinc-zinc distance of 3.42 Å. [10] The crystal structure of this enzyme shows the same site with an only slightly longer zinc-zinc distance, 3.46 Å. Cobalt-substituted L1 differs from the native form. From EXAFS it appears, the average coordination number of the active site increases by one half and the average bond length increases by 0.07 Å. There is no evidence of a bridge between the two metals and as such no cobalt-cobalt distance was observed. EXAFS of the product complex of ZnZn L1 bound to the ring-opened nitrocefin indicates a rotation of the six-membered ring, with the sulfur of the thioether binding to the zinc. This provides a sulfur bound to the metal site which was detectable by EXAFS. [9]

Exploiting the sequential binding of L1, a ZnCo L1 [8] was produced to monitor each metal site individually. The EXAFS of this species will be discussed later in this chapter, but other kinetic and spectroscopic techniques have been previously reported. ZnCo L1 was found to be as active as native L1. The UV-visible spectrum displays no Co-S LMCT bands and the d-d bands reveal a series of broad peaks between 500-650 nm

with a maximum extinction coefficient of 130 M^{-1} cm^{-1} consistent with a five coordinate species. The paramagnetic ^{1}H NMR displays one broad solvent exchangeable peak at 50ppm corresponding to two unresolved histidine residues based on integration. Stopped flow studies with nitrocefin show the appearance of the reaction intermediate in a manner similar to other dimetal L1's. The EPR spectrum of CoZn L1 is similar to monocobalt L1 and is markedly different from CoCo L1. These pieces of information suggest that the cobalt binds to the enzyme in the Zn_2 (DHH) site, and that the zinc is bound at the Zn_1 (3H) site.

In order to further elucidate the mechanism of B3 metallo-β-lactamase, L1, hydrolysis of nitrocefin, a β-lactam antibiotic, rapid freeze quench techniques were utilized to structurally characterize the observed reaction intermediate. This technique will be applied to the native dizinc L1, in addition to the mixed metal CoZn L1, in order to look at the metal coordination at one time point within the reaction.

Experimental Procedures

L1 was prepared according to established procedures for initial studies, but a new procedure was developed for producing CoZn L1. A single equivalent of cobalt was incorporated biologically with a media very low in zinc and high in cobalt during periods of overexpression. After spectroscopic verification of metal content, a direct addition of zinc (II) brought the enzyme to the desired metal content. [11]

Rapid freeze quench samples were generated using a modified Update Instruments (Madison, WI) rapid-freeze-quench system. Equal volumes of 1mM L1 and

5 mM nitrocefin, each containing 20% glycerol in 50 mM HEPES, pH 7.0, were rapidly mixed (<1 ms), incubated at 2° C, and freeze-quenched in 2-methylbutane at -130° C. [12] The total effective reaction time was 10ms; this was calibrated by comparing the development of a low-spin Fe(III) EPR signal and the disappearance of a high-spin Fe(III) EPR signal with the associated optical changes at 636 nm using stopped-flow spectrophotometry, upon mixing myoglobin with an excess of sodium azide. The syringes, mixer, and tubing were all maintained at 2° C using ice water. Immediately prior to sample collection (< 1s), the nozzle and attached mixer were removed from the bath and held 5 mm above the surface of 2-methylbutane contained in a collecting funnel and maintained at -130° C by a surrounding bath of liquid nitrogen cooled 2-methylbutane. Samples were packed into custom EXAFS cuvettes designed to interface with this setup at -130° C and stored in liquid nitrogen. EXAFS data collection and analysis were conducted according to methods previously reported. [13]

Results

The freeze-quenched di-zinc L1 reacted with nitrocefin shows moderate differences from either the resting state or the product bound state. The best fit to the freeze-quenched sample is an average primary coordination sphere of 4.5, which is similar to the first shell coordination sphere of the resting enzyme. The average bond length was fitted to 2.03 Å. There is no detectable presence of sulfur in the spectrum. The addition of a half of a carbon at 2.45 Å (corresponding to a carboxylate ligand on one of the two sites) improves the fit residual by 50%. The presence of a zinc shell at 3.72 Å improves the fit residual by 70% (Table 5-1).

The cobalt-zinc mixed-metal sample provides a baseline for comparison to the freeze-quenched sample that will be described later. This sample contains one equivalent of cobalt as over-expressed. The dinuclear site is formed by supplementing the mono-cobalt L1 by direct addition of zinc. The metal content was confirmed by ICP. The EXAFS analysis shows a sequential binding of the metal with the cobalt being best fit by a model corresponding to the Zn_2 (DHH) site and the zinc being best fit by a model corresponding to the Zn_1 (3H) site. (Table 5-2) *In vivo*, the cobalt (II) is added to the Zn_2 (DHH) site which is best fit to the data with 3 N/O (2.10 Å) and 2 N/O (1.94 Å) along with 2 histidine ligands and a cobalt-zinc distance of 3.40 Å. (Table 5-2) Moving from a single shell to multiple shells to characterize the intensity at a distance of 1.5 Å resulted in a fit improvement of 75%. The difference in the distances between the two shells, 0.16 Å, is on the low edge of the resolutions of the data (0.14 Å). The addition of the cobalt-zinc shell improves the fit residual by 40%. The direct addition of the zinc (II) completes the active site binding to the Zn_1 (3H) site. This site is well defined by a single shell of four N/O at 2.00 Å with three histidine ligands and a zinc-cobalt distance of 3.42 Å. The addition of the zinc-cobalt shell improves the fit by 32%. The correlation between the metal-metal distance between the EXAFS of the two edges further supports the presence of a water/hydroxide bridge between the two metals. A bridge between the two metals is required in order to see the interaction.

A 10 ms freeze-quenched sample of the mixed-metal CoZn L1 with nitrocefin display similar results to the resting mixed metal sample. The cobalt is bound to the Zn_2 site and the zinc is bound to the Zn_1 site. The coordination number at the cobalt remains at five with no effective change in average bond length. (Table 5-3) The coordination

number of the zinc moves from four to five, though the bond length does not show the accompanying expansion that is expected. Without the increase in bond length, it is unlikely that the higher coordination number is present. Upon addition of a metal-metal shell to either of the fits, the distance refines to 3.75 Å. The fit residual improvement however is only 4%. This improvement is too small to be considered. The lack of a metal-metal interaction suggests the lack of a bridging species providing an order of the two sites with respect to each other.

Discussion

The differences between the freeze-quenched samples suggest that we are looking at a different state from either the resting or the product bound state. The state that was captured displays similar coordination number to the two other stages of the reaction mechanism we have studied. The maintenance of coordination number suggests that the binding of substrate replaces ligands around the metal. The most likely ligand leaving the metal would be the bridging or the terminal water. The coordination of the carboxylate to the Zn_1 (DHH) site would lead to the loss of either one of the bound residues, the terminal water to the bulk solvent, or the bridging water/hydroxide to the Zn_2. The loss of the bridging water/hydroxide would lead to a more active nucleophile in the position to attack the lactam carbonyl producing the ring-opened product. From the zinc-zinc distance that was measured, this ring opening occurs within 10 ms, the minimum lag time for our freeze quench apparatus. There is no sulfur present in the freezed-quench sample, which would place this rotation at a timeframe after the 10 ms of the reaction. This

provides the two extreme time points for the spectra acquired, but leaves a fair number of stages of the reaction that our intermediate could represent.

One primary question is the state of the formerly amide based nitrogen. Immediately after the ring opening reaction, the nitrogen would possess a formal negative charge. Stabilization is possible due to the extended conjugation that extends out along the dinitrostyrene side chain, found exclusively in nitrocefin. The negatively charged nitrogen will ultimately become protonated as the product is released. The freeze-quenched sample may contain a protonated nitrogen, but the presence of the extended conjugation and the intermediate observed under stopped-flow optical studies, suggest that the negatively charged species may exist for a observable length of time. Another possibility other than the protonation state of the nitrogen is that the negative charge is in close proximity to the positively charged zinc ion. The opposing charges could temporarily stabilize one another. Formation of a bond between the anionic nitrogen and the zinc would decrease the reaction speed. In the freeze-quenched sample, the coordination number of the Zn_2 is five, which would suggest that the bond between the nitrogen and the zinc has not formed. Otherwise, one of the exchangeable ligands would have to be released.

A comparable structure is the crystal structure of L1 complexed with hydrolyzed moxalactam. [14] This structure shows a larger average coordination sphere from 4.5 to 5.5 and a solvent derived bridge molecule. It also displays a bond between the former amide nitrogen to Zn_2. The formation of the Zn-N bond will be strong due to the excess electron density on the nitrogen after the cleavage of the bond. The strength of this bond will have likely impede release of the product and contribute to the stability of the

complex. The change in coordination number between the L1-moxalactam crystal structure and this freeze-quenched species may be explained by the lack of a solvent molecule bridging the two metals, though the zinc-zinc distance is only modestly elongated (3.68 Å vs 3.72 Å). The higher coordination number of the moxalactam complex will tend towards higher average ligand bond lengths, which will allow for a more relaxed Zn-O-Zn bond angle. The freeze-quenched nitrocefin sample has a lower average bond distance and a longer zinc-zinc distance, which would push the bond angle more towards linear.

The CoZn L1 sample provides a unique opportunity for us it allows us to probe the individual metal sites in the di-metal enzyme. Previously, the study of subclass B2 would provide insight into the Zn_2 site and monosubstituted enzymes of subclasses B1 and B3 could provide insight into the Zn_1 site. Due to the limitations of the spectroscopic techniques employed, the dizinc or dicobalt forms are observable as an average of the two sites (EXAFS) or as a sum of two individual spectra that can be difficult to resolve. The mixed metal sample allows for the probing of each site independent of the other. Combined with the versatility of x-ray spectroscopy, one sample may be analyzed for both elements, removing the variation that can be present among samples biologically prepared. This situation is ideal for the freeze-quenched experiments, in that the coordination number of both metals in the reaction mechanism can be probed separately giving us a closer look at the mechanism that is present. Kinetics studies show that the CoZn L1 retains 67% of the native activity, which could indicate that the enzyme retains the same mechanism. [8]

The mixed-metal sample has been studied previously using UV-visible, paramagnetic nuclear magnetic resonance, and electron paramagnetic resonance spectroscopies. These studies suggest the cobalt binds to the Zn_2 (DHH) site of L1. The UV-visible spectrum displays multiple unresolved peaks between 500-650 nm with a net extinction coefficient of 130 $M^{-1}cm^{-1}$. These features are commonly ascribed to 5-coordinate cobalt (II). The spectra the 1 Co L1 and the CoZn L1 display are identical, but are different from CoCo L1. This suggests that the cobalt occupies one unique location instead of occupying an average of the two sites. The NMR spectra display one broad peak that was solvent exchangeable at 50 ppm. The integration of this peak showed that it was equivalent to two protons. These protons would correspond to the solvent exchangeable protons of the two histidine ligands bound to the metal. This spectrum was similar to the precursor 1 Co L1 sample before the addition of zinc, which suggests that the addition of zinc minimally disrupts the cobalt binding. The EPR spectroscopy was found to contain two species attributed to the equilibrium between Co(II)-H_2O and Co(II)-OH. These findings are in agreement with what we have observed. The cobalt locates in the Zn_2 (DHH) site and is bound to two water/hydroxide ligands and the zinc binds in the Zn_1 (3H) site with a single water/hydroxide.

The freeze-quenched CoZn L1 sample provides multiple points of comparison. First, the freeze-quenched sample may be compared with the CoZn L1 sample. This will provide two stages along the reaction pathway. Direct comparison between the zinc and the cobalt spectra between the two samples will allow us to look at both of the sites at ten milliseconds into the reaction. At this time frame it appears that the ring opening reaction has occurred. The lack of a definitive metal-metal distance adds some ambiguity to the

placement within the reaction scheme. The metal-metal distance refines to 3.75 Å at both the zinc and cobalt edges, though the improvement in the fit residual (4%) is too low to be considered. Apart from the lack of a visible metal-metal distance, the cobalt-edge remains similar to the resting enzyme in both bond length and coordination number. This can be explained by replacing the bridging hydroxide with the substrate carboxylate.

The zinc-edge spectrum shows some differences from the resting state spectrum. Although the average bond length is unchanged, the refined coordination number is larger, which suggests that the site has acquired an additional ligand or that the site has become more ordered. Within the reaction scheme, there are two stages where the Zn_1 (3H) site should be five-coordinate. As the substrate binds, the lactam carbonyl will bind to the Zn_1 (3H) site, while the metal remains bound to a hydroxide/water and after the nucleophilic attack on the lactam, the newly formed carboxylic acid may temporarily assume a bidentate binding mode. These cases should move to a four-coordinate zinc as the reaction progresses.

Second CoZn L1 may be compared to the ZnZn L1 sample to compare both reactions at the same time frame. With the overall reaction taking 50% longer (25.6 ms vs. 38.4 ms as calculated from k_{cat}), the 10 ms time frame may show different stages of the reaction. The stopped flow of comparison of the dizinc L1 and ZnCo L1 shows that there is a significant population of the intermediate present in both samples. Alternatively if both are at the rate-limiting step of the reaction, the freeze quenched CoZn L1 sample may provide insight into the activity occurring at each of the two metals within the reaction. What has been observed is that the average of the two sites in the freeze-

quenched CoZn L1 sample, averaging a coordination number of 4.5 with 2.5 histidines is similar to the freeze-quenched ZnZn L1 sample.

This study provides a look at a single state of the reaction mechanism that is primarily characterized by similar coordination numbers and an increase of metal-metal distance. The implications of this metal-metal distance is that the ring opening reaction is rapid in the reaction scheme and that the slower steps of this reaction are the protonation events that facilitate product release. Based on the proposed reaction mechanism, two protons are required for product release. The first is the cycloamine. After the cleavage of the lactam bond, this nitrogen would possess a formal negative charge, which is stabilized by resonance in nitrocefin. In other species that do not display the intermediate in stopped-flow UV-visible spectroscopy, this species remains for an even a shorter time. The other ligand that would facilitate product release by protonation is the ring-bound carboxylate. The release of this group is necessary for the rotation that allows for the thioether to be bound to the zinc. The proton source remains in question. The possible sources are active site residues, the terminal water, and local water molecules. With the proximity to the metal, the loss of a proton from either of the water ligands could aid in the later formation of a hydroxide bridge between the metal sites.

It may be possible to understand the enzymatic mechanism as a function of metal-metal distance. The resting state of the enzyme maintains the hydroxide/water bridge and a metal-metal distance of 3.4 Å. At 10 ms of reaction time, this distance has been extended to 3.72 Å. With the product bound, the distance is intermediate to the two at 3.62 Å. One means of enzymatic activity is the substrate binds to both metals, through the carbonyl to one and through the carboxylic acid to the other, then the bridge between the

metals breaks and enzymatic motions moves the metals apart. This provides a tension on the four-membered lactam ring, which is then hydrolyzed by the metal-bound hydroxide. In the following steps, the system relaxes and the metals move closer together.

The 10 ms examined here is the shortest time that the commercial freeze-quench apparatus can attain, therefore to capture earlier stages in the reaction a custom apparatus must be constructed. Additionally later time frames may be helpful in elucidating the stages after the ring opening. The combination of the longer and shorter time frames will provide a more complete scheme by which the reaction proceeds. Subtle protonation events may beyond the ability of EXAFS to probe, but the rotation of the six-membered ring could be monitored by looking for the appearance of the metal-sulfur bond. The loss and reformation of the hydroxide bridge between the metals should also be a possible target for EXAFS studies.

Summary

These studies have delved into the mechanism of the metallo-β-lactamase L1. Rapid freeze quenching of L1 samples reacted with nitrocefin was collected at 10 ms into the reaction. The EXAFS data show that there is an increase in the zinc-zinc distance upon ring opening that is greater than in the L1 nitrocefin product complex. Additionally, the production of mixed metal samples has greatly increased the capabilities of EXAFS analysis of these systems. Monitoring each metal site individually in the system removes a limitation with x-ray absorption techniques, which studies an average of the metal population. Mixed metal L1 combined the rapid freeze quenching allowed for the metal environment of both sites of the enzyme to be separately studied.

References

1. McManus-Munoz, S. and M.W. Crowder, *Kinetic Mechanism of Metallo-β-Lactamse L1 from Stenotrophomonas maltophilia.* Biochemistry, 1999. **38**(5): p. 1547-1553.

2. Wang, Z., W. Fast, and S.J. Benkovic, *Direct Observation of an Enzyme-Bound Intermediate in the Catalytic Cycle of the Metallo-β-Lactmase from Bacteroides fragilis.* American Chemical Society, Journal of, 1998. **120**(41): p. 10788-10789.

3. Wang, Z., W. Fast, and S.J. Benkovic, *On the Mechanism of the Metallo-β-Lactamase from Bacteroides fragilis.* Biochemistry, 1999. **38**(31): p. 10013-10023.

4. Wang, Z. and S.J. Benkovic, *Purification, Characterization, and Kinetic Studies of a Soluble Bacteroides fragilis Metallo-β-Lactamase That Provides Multiple Antibiotic Resistance.* Biological Chemistry, Journal of, 1998. **273**(35): p. 22402-22408.

5. Lisa, M., L. Hemmingsen, and A.J. Vila, *Catalytic Role of the Metal Ion in the Metallo-β-Lactamase GOB.* Journal of Biological Chemistry, 2009. **285**: p. 4570-4577.

6. Hu, Z., G. Periyannan, and M.W. Crowder, *Folding Strategy to Prepare Co(II)-substituted Metallo-β-lactamase L1.* Analytical Biochemistry, 2008. **378**: p. 177-183.

7. Macheboeuf, P., et al., *Active Site Restructuring Regulates Ligand Recognition in Class A Penicillin-Binding Proteins.* Proceedings of the National Academy of Science of the United States of America, 2005. **102**(3): p. 577-582.

8. Hu, Z., et al., *Role of Zn1 and Zn2 Sites in Metallo-b-lactamase L1.* American Chemical Society, Journal of, 2008. **130**: p. 14207-14216.

9. Costello, A.L., et al., *Site Selective Binding of Zn(II) to Metallo-b-Lactamase L1 from Stenotrophomonas maltophilia.* Biological Inorganic Chemistry, Journal of, 2006. **11**(3): p. 351-358.

10. Ullah, J.H., et al., *The Crystal Structure of the L1 Metallo-β-Lactamase from Stenotrophomonas maltophilia at 1.7 Å Resolution.* Molecular Biology, Journal of, 1998. **284**(1): p. 125-136.

11. Breece, R.M., et al., *Motion of the Zinc Ions in Catalysis by a Dizinc Metallo-β-Lactamase.* American Chemical Society, Journal of, 2009. **131**: p. 11642-11643.

12. Garrity, J.D., B. Bennett, and M.W. Crowder, *Direct Evidence that the Reaction Intermediate of Metallo-β-lactamase L1 is Metal Bound.* Biochemistry, 2005. **44**: p. 1078-1087.

13. Thomas, P.W., et al., *The Quorum-quenching Lactonase from Bacillus thuringiensis is a Metalloprotein.* Biochemistry, 2005. **44**(20): p. 7559-7569.

14. Spencer, J., et al., *Antibiotic Recognition by Binuclear Metallo-β-Lactamases Revealed by X-ray Crystallography.* American Chemical Society, Journal of, 2005. **127**(41): p. 14439-14444.

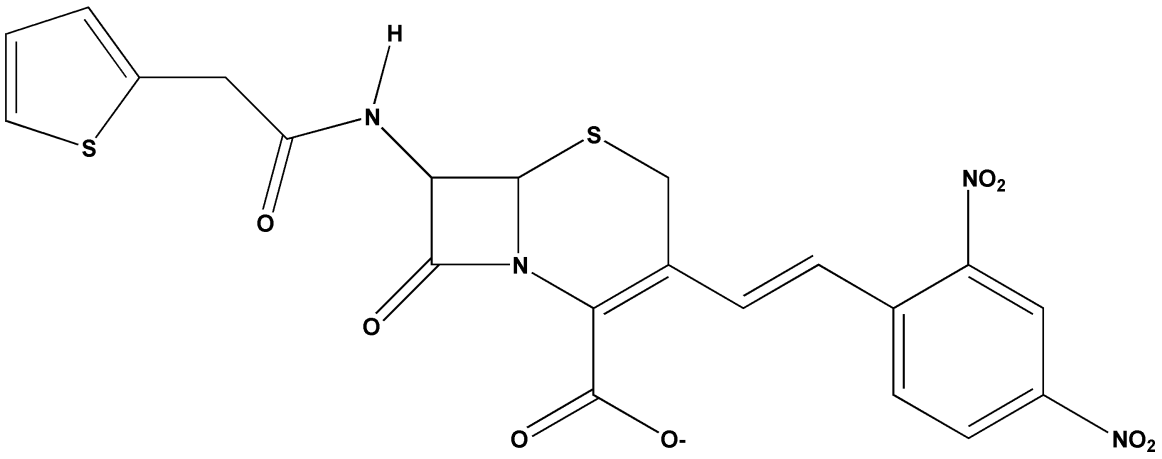

Figure 5-1: Structure of Nitrocefin

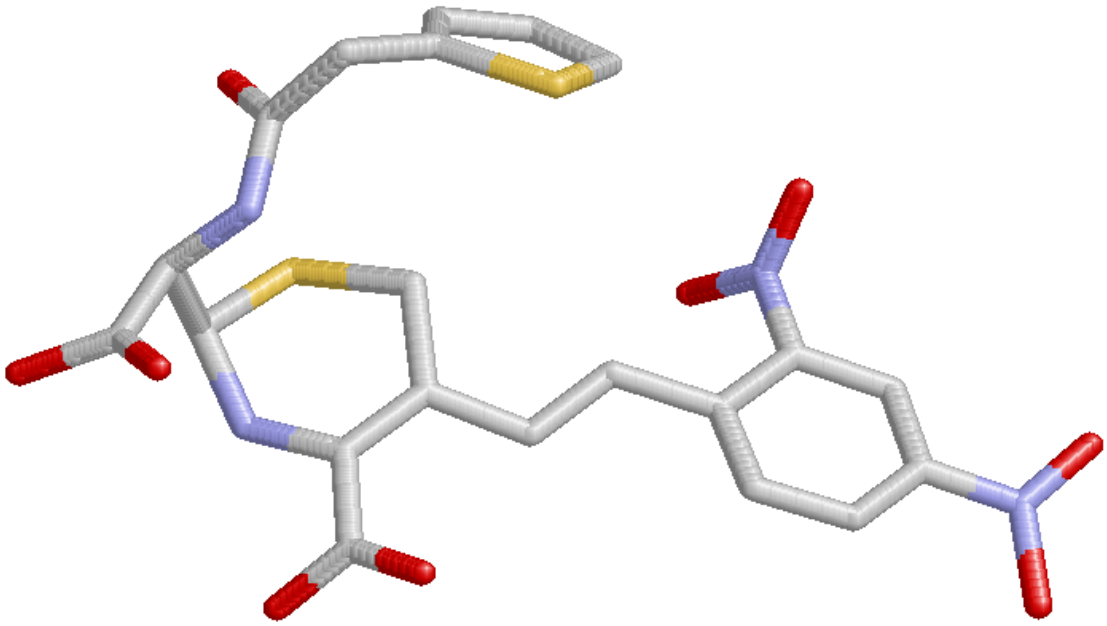

Figure 5-2: Crystal Structure of Ring-Opened Nitrocefin.
(Rendered with RasMol from 2UWX)

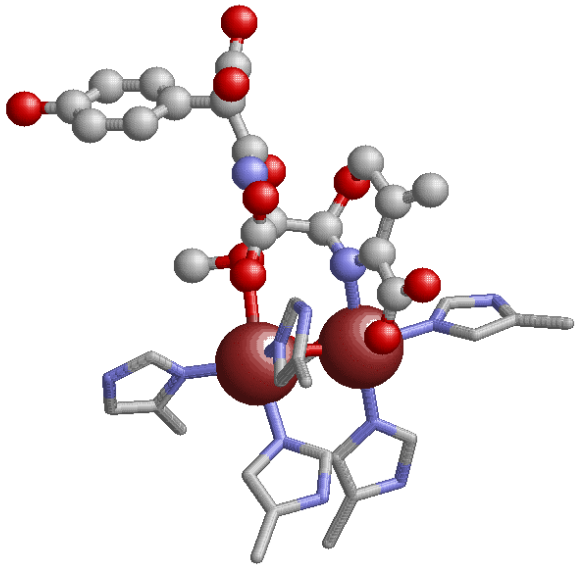

Figure 5-3: L1 bound to ring-opened Moxalactam
(Rendered with RasMol from 2aio)

Table 5-1. Detailed EXAFS curve fitting results for freeze-quenched ZnZn-L1. [a]

Fit	Model	*Zn-N/O*	*Zn-S*	*Zn-His* [b]	*Zn-Zn*	R_f [c]	R_u
	ZnZn-L1						
1	4.5 N/O	2.03 (5.6)				112	330
2	2.5 N + 2 O	2.08 (3.8) 1.94 (1.3)				31	70
3	2 N + 2 O + 0.5 S	2.18 (24) 1.97 (1.3)	2.24 (3.1)			21	65
Fit	Model	*Zn-N/O*	*Zn-C*	*Zn-His* [b]	*Zn-Zn*	R_f [c]	R_u
4	4.5 N/O (2.5 His)	2.03 (10)		2.90 (4.3), 3.15 (10) 4.13 (20), 4.36 (15)		124	216
5	4.5 N/O + 0.5 C (2.5 His)	2.03 (10)	2.45 (0.3)	2.89 (4.2), 3.12 (13) 4.11 (16), 4.36 (17)		82	192
6	4.5 N/O + 0.5 C (2.5 His) + Zn-Zn	2.03 (10)	2.45 (0.2)	2.86 (6.1), 3.15 (10) 4.12 (8.7), 4.35 (14)	3.72 (6.6)	26	156

[a] Distances (Å) and disorder parameters (in parentheses, σ^2 (10^{-3} Å^2)) shown derive from integer or half-integer coordination number fits to filtered EXAFS data [Zn-edge: k = 1.5-13.7 Å^{-1}; R = 0.7-2.2 Å (Fits 1-3), R = 0.2-4.0 Å (Fits 4-6)]

[b] Multiple scattering paths represent combined paths, as described previously (see Materials and Methods)

[c] Goodness of fit (R_f for fits to filtered data) defined as $1000 * \frac{\sum_{i=1}^{N}\left\{[\mathrm{Re}(\chi i_{calc})]^2 + [\mathrm{Im}(\chi_{i_{calc}})]^2\right\}}{\sum_{i=1}^{N}\left\{[\mathrm{Re}(\chi i_{obs})]^2 + [\mathrm{Im}(\chi_{i_{obs}})]^2\right\}}$, where N is the number of data points

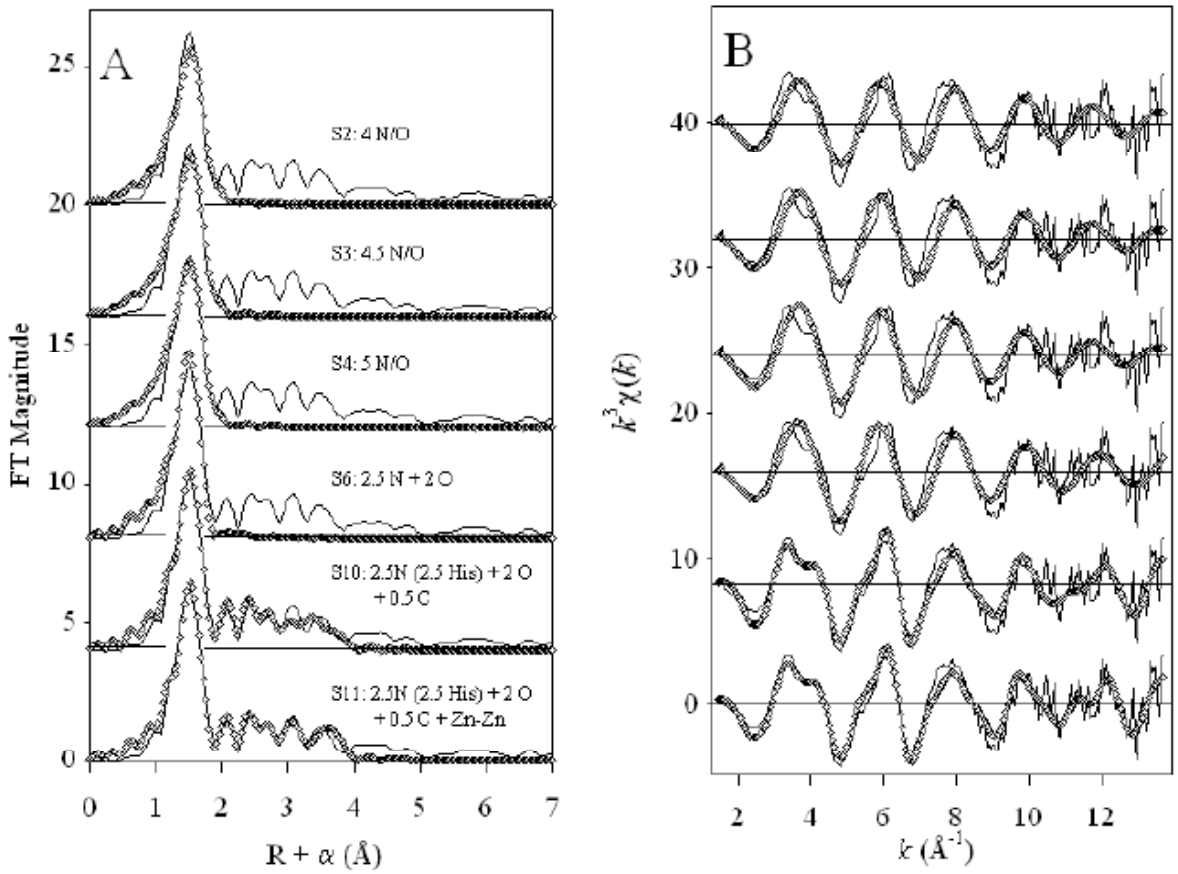

Figure 5-4. Fourier transforms (A) of k^3-weighted EXAFS (B) for ZnZn-L1, freeze-quenched after 10 ms reaction with nitrocefin (solid lines), and corresponding curve fits (open symbols) from Table 5-1.

Table 5-2. Detailed EXAFS curve fitting results for CoZn-L1. [a]

Fit	Model	*M-N/O*	*M-His* [b]	*M-M*	R_f [c]	R_u
	CoZn-L1 (Zn edge)					
	4 N/O	2.00 (4.5)			13	206
	4 N/O (3 His)	2.00 (4.3)	2.90 (4.7), 3.14 (2.8) 4.10 (18), 4.41 (20)		31	70
	4 N/O (3 His) + Co-Zn	2.01 (6.1)	2.90 (5.6), 3.13 (3.7) 4.22 (26), 4.41 (16)	3.42 (13)	21	65
	CoZn-L1 (Co edge)					
	4 N/O	2.16 (9.9)			275	514
	3N 2O	2.10 (2.2) 1.94 (1.2)			74	322
	3N 2O (2 His)	2.10 (3.0) 1.94 (2.6)	2.81 (3.8), 3.13 (2.1) 3.95 (5.1), 4.52 (7.8)		90	183
	3N 2O (2 His) +Co-Zn	2.10 (2.3) 1.94 (1.5)	2.84 (8.2), 3.14 (6.6) 3.79 (7.0), 4.53 (10)	3.40 (6.9)	54	169

[a] Distances (Å) and disorder parameters (in parentheses, σ^2 (10^{-3} Å^2)) shown derive from integer or half-integer coordination number fits to filtered EXAFS data [Zn-edge: k = 1.5-14 Å^{-1}; R = 0.1-4.0 Å; Co-edge: k = 1.5-12.5 Å^{-1}; R = 0.1-4.1 Å]

[b] Multiple scattering paths represent combined paths, as described previously (see Materials and Methods)

[c] Goodness of fit (R_f for fits to filtered data) defined as $1000 * \frac{\sum_{i=1}^{N}\left\{\left[\mathrm{Re}(\chi i_{calc})\right]^2 + \left[\mathrm{Im}(\chi i_{calc})\right]^2\right\}}{\sum_{i=1}^{N}\left\{\left[\mathrm{Re}(\chi i_{obs})\right]^2 + \left[\mathrm{Im}(\chi i_{obs})\right]^2\right\}}$, where N is the number of data points

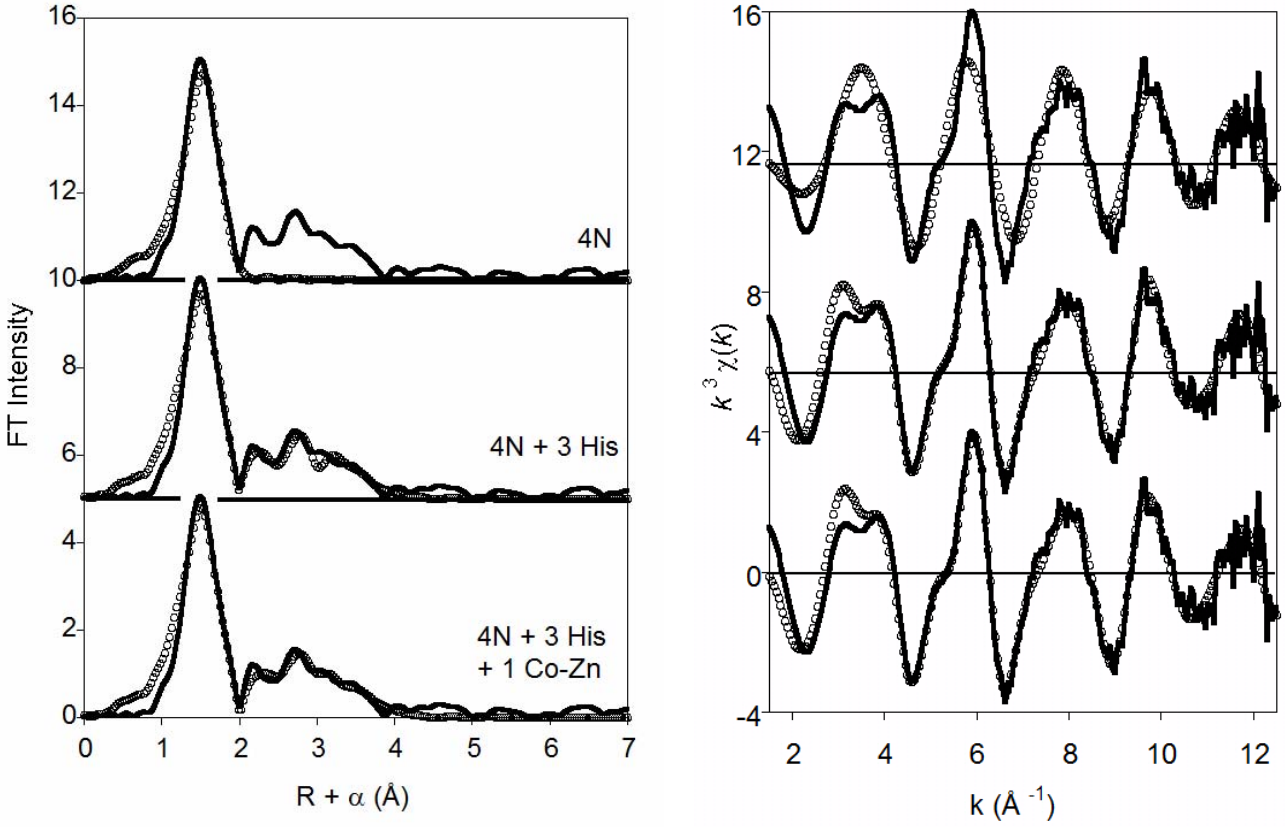

Figure 5-5. Fourier transforms (A) of k^3-weighted EXAFS (B) for the zinc edge of CoZn-L1 (solid lines), and corresponding curve fits (open symbols) from Table 5-2.

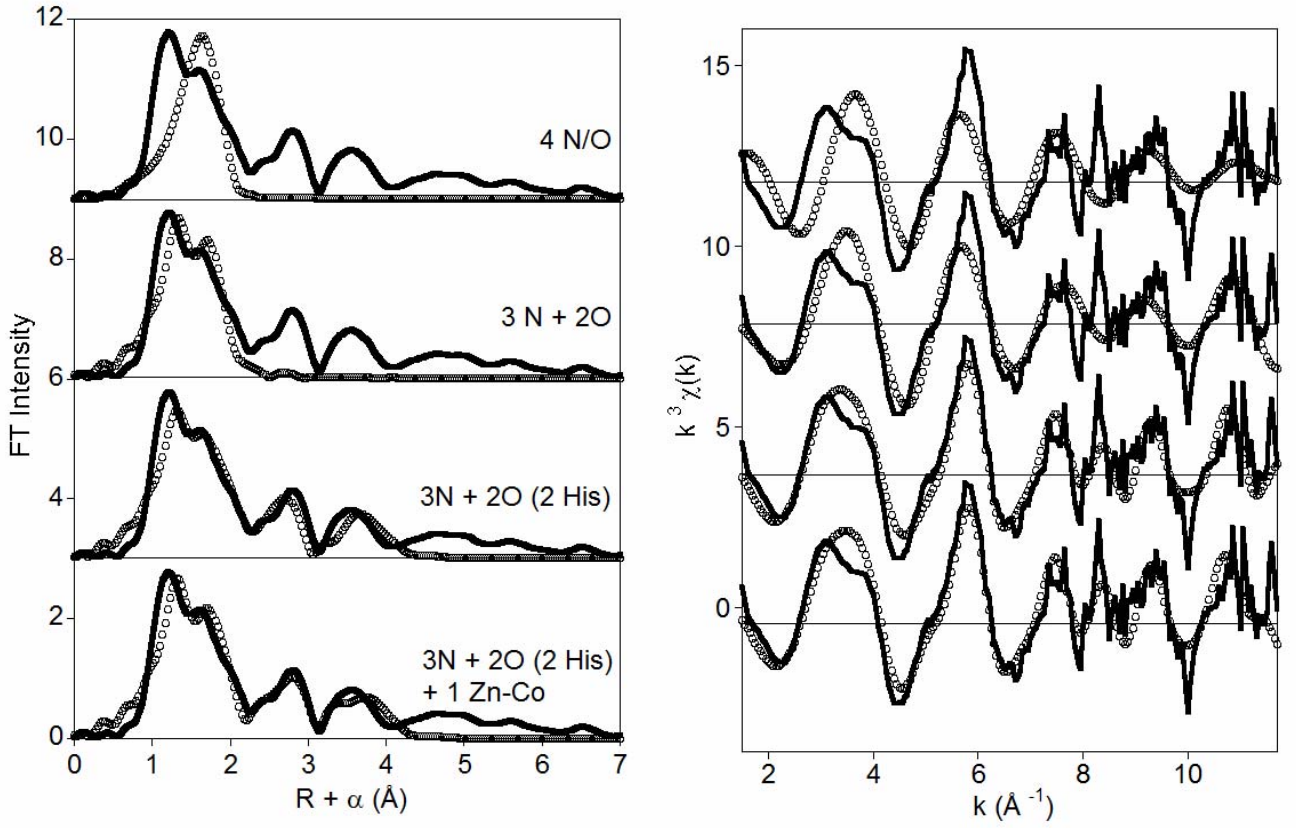

Figure 5-6. Fourier transforms (A) of k^3-weighted EXAFS (B) for the cobalt edge of CoZn-L1 (solid lines), and corresponding curve fits (open symbols) from Table 5-2.

Table 5-3. Detailed EXAFS curve fitting results for freeze-quenched CoZn-L1. [a]

Fit	Model	*M-N/O*	*M-His* [b]	*M-M*	R_f [c]	R_u
	CoZn-L1 (Zn edge)					
	5 N/O	2.02 (3.3)			11	293
	5 N/O (3 His)	2.02 (4.3)	2.91 (5.8), 3.17 (4.2) 4.17 (27), 4.43 (19)		77	195
	5 N/O (3 His) + Co-Zn	2.02 (5.5)	2.91 (5.7), 3.16 (3.7) 4.07 (33), 4.41 (19)	3.75 (18)	74	194
	CoZn-L1 (Co edge)					
	4 N/O	2.07 (8.6)			86	500
	3N + 2O	2.11 (0.2) 1.95 (1.8)			36	408
	3N + 2O (2 His)	2.08 (0.8) 1.94 (1.0)	2.83 (5.0), 3.11 (0.4) 3.95 (2.1), 4.51 (4.4)		58	231
	3N + 2O (2 His) + Co-Zn	2.08 (0.8) 1.94 (1.1)	2.82 (5.8), 3.11 (0.5) 4.13 (0.9), 4.52 (3.4)	3.77 (3.7)	56	220

[a] Distances (Å) and disorder parameters (in parentheses, σ^2 (10^{-3} Å^2)) shown derive from integer or half-integer coordination number fits to filtered EXAFS data [Zn-edge: k = 1.5-14 Å^{-1}; R = 0.1-4.0 Å; Co edge: k = 1.5-12.5 Å^{-1}; R = 0.1-4.1 Å]

[b] Multiple scattering paths represent combined paths, as described previously (see Materials and Methods)

[c] Goodness of fit (R_f for fits to filtered data) defined as $1000 * \frac{\sum_{i=1}^{N}\left\{\left[\mathrm{Re}(\chi_{i_{calc}})\right]^2+\left[\mathrm{Im}(\chi_{i_{calc}})\right]^2\right\}}{\sum_{i=1}^{N}\left\{\left[\mathrm{Re}(\chi_{i_{obs}})\right]^2+\left[\mathrm{Im}(\chi_{i_{obs}})\right]^2\right\}}$, where N is the number of data points

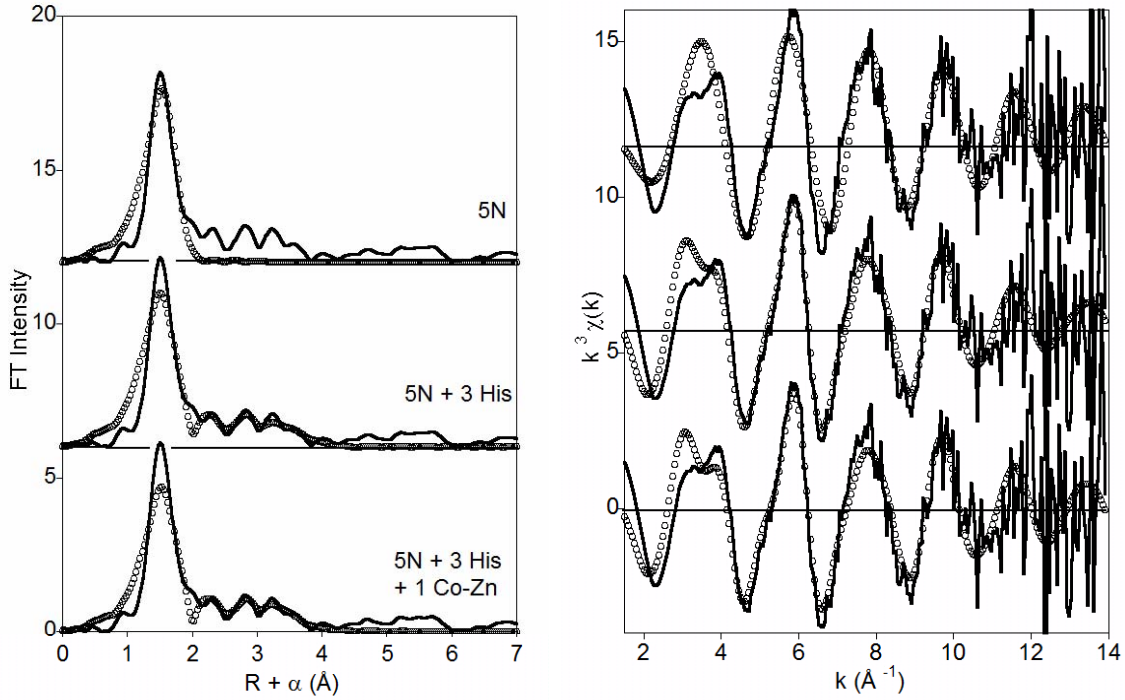

Figure 5-7. Fourier transforms (A) of k^3-weighted EXAFS (B) for the zinc edge of CoZn-L1, freeze-quenched after 10 ms reaction with nitrocefin (solid lines), and corresponding curve fits (open symbols) from Table 5-3.

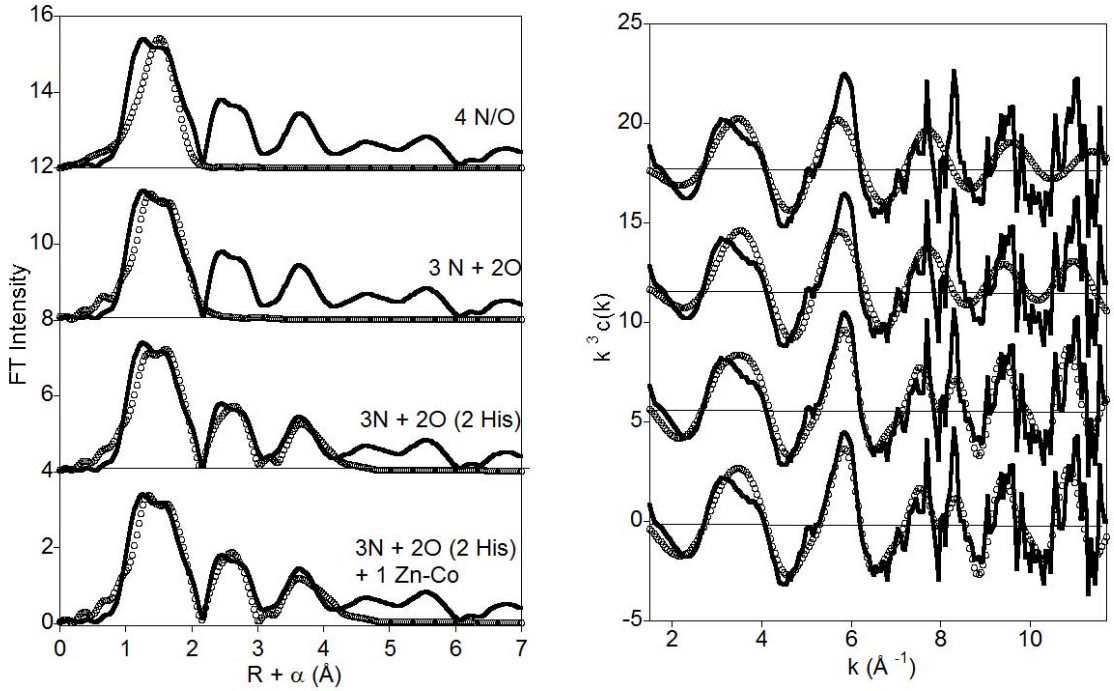

Figure 5-8. Fourier transforms (A) of k^3-weighted EXAFS (B) for the cobalt edge of CoZn-L1, freeze-quenched after 10 ms reaction with nitrocefin (solid lines), and corresponding curve fits (open symbols) from Table 5-3.

Chapter VI

Summary and Future Work

This work builds upon the foundation of previous work using x-ray absorption spectroscopy in the analysis of metallo-β-lactamases. This research has used x-ray absorption spectroscopy to explore the metal binding behavior within the B1 subclass and probes the mechanism of the B3 subclass. Most importantly, this work presents a series of tools and techniques that will aid in further explorations of the structure and function of this superfamily of enzymes.

Metal Binding Behavior of Metallo-β-Lactamases

To date, three members of subclass B1 have been characterized by x-ray absorption spectroscopy. In each case, they provide different metal binding behavior. The first, CcrA, has been seen to follow sequential binding. BcII binds metals to both sites when exposed to divalent metal ions. Bla2 binds zinc differently than cobalt, with zinc binding like CcrA and cobalt binding like BcII. This variation within one subclass, suggests that the previous strategy of taking one member of each subclass as an example will provide an incomplete picture of that subclass. To address this issue, studies are being expanded to other members of the subclasses. Future studies should include Imp1 and MDN, B1 metallo-β-lactamases that are more commonly found in clinical settings.

The differential binding in Bla2 provides another difference in the behavior of cobalt and zinc in enzymes. Cobalt is often used as a spectroscopic probe of zinc metallo-

proteins, but previous research has suggested that the resting state of cobalt-substituted enzyme contains additional solvent molecules compared to the zinc-containing enzyme. This is a case that the differences between the two metals alone are enough to affect the binding behavior. This suggests that in the zinc case the binding affinity between the Zn_1 and Zn_2 sites are different enough that there is preferential binding to the Zn_1 site, however for cobalt, the binding affinity to the two sites are more similar, allowing for the two sites to become occupied simultaneously. This is the first case of the metal binding being different between zinc and cobalt. With minimal differences in the two sites, mutagensis should be used to convert the active sites and mimic the other site's metal binding behavior.

The sequential nature of the metal to these enzymes allowed for the production of the mixed metal forms, which allows for the study of each site individually in the bimetallic enzyme. These studies have shown that the formation of ZnCo L1 is possible and that it forms a bridged species similar to that of the native dizinc L1. Future studies should use this mixed metal approach to explore any of the other metallo-β-lactamases that display sequential binding, including CcrA and potentially Bla2 starting from a 1 Zn Bla2 foundation. Any of these potential forms may then be used to explore the differences between that and the L1.

Mechanism of Metallo-b-Lactamases

Using rapid freeze quenched samples, a reaction intermediate was characterized in the reaction of L1 with nitrocefin. This intermediate expands the information provided previously by the crystal structure of L1 and moxalactam. The freeze-quenched sample

shows a ring-opened intermediate at 10 ms. This ring opening displays a metal-metal distance longer than either the resting enzyme or the product-bound enzyme. Further study should expand the type of enzyme and the type of β-lactam antibiotics. Other antibiotics do not display the optically observable intermediate, but could provide insight into the mechanism with respect to more commonly employed antibiotics in the clinical setting. Looking at other subclasses of enzymes could be used to look for commonalities and differences between the different reaction mechanisms. Additionally, looking at L1 with a single equivalent of metal could provide a nice comparison with the B2 subclass of enzyme, looking at how this versatile active site reacts at both the metal sites. Finally, probing additional time points would alloy for the study of the full duration of the reaction and look at the enzyme returning to the resting state.

The combination of the mixed metal form and the rapid freeze-quenching techniques allows us to look at the reaction in even more detail. Study of the coordination number and bond length of the individual sites will allow for the probing of different stages within the reaction mechanism. Currently, two time points have been collected, the resting form and the 10 ms time frame. The mixed metal form with product bound is one of the next data sets to be collected. Additional time points, after 10 ms will allow for the study of those alterations that lead to the product bound form as well as the relaxation towards the resting state of the enzyme. The construction of an apparatus for looking at shorter time frames is of greater interest, in order to look at species before the ring opening, particularly the substrate binding step.